FERMILAB-THESIS-1991-23

A Study of Charmed Meson Decays Involving K_S^0's

A Dissertation submitted to the
Division of Graduate Studies and Research
of the University of Cincinnati

in partial fulfillment of the
requirements for the degree of

DOCTOR OF PHILOSOPHY

in the Department of Physics
of the College of Arts and Sciences
1991
by

Anthony Lee Shoup
B.S., Wright State University, 1984
M.S., University of Cincinnati, 1987

Abstract

A Study of Charmed Meson Decays Involving K^0_S's

by

Anthony Lee Shoup

Using data from the Fermilab experiment E691, I have measured the branching ratios for the decays: $D^0 \to \overline{K^0}\pi^0$, $D^0 \to \overline{K^0}K^0$, $D^0 \to \overline{K^0}\,\overline{K^0}K^0$, $D^+ \to \overline{K^0}\pi^+$, $D^+ \to \overline{K^0}K^{*+}$, $D_s^+ \to \overline{K^0}K^{*+}$. The large branching ratio (relative to $K^-\pi^+$) of $BR(D^0 \to \overline{K^0}\pi^0) = (5.0 \pm 0.8 \pm 0.9)\%$ indicates either a lack of color suppression or significant elastic final state interactions. I saw no evidence for the decay $D^0 \to \overline{K^0}K^0$ and set a 90% CL upper limit of 0.12%. This limit indicates that inelastic final state interactions do not mix final states such as K^+K^- or $\pi^+\pi^-$ into the $\overline{K^0}K^0$ state above the 20% level. The result $BR(D^+ \to \overline{K^0}K^{*+}) = (3.2 \pm 1.2 \pm 0.8)\%$ is consistent with similar D→PV decays (P-pseudoscalar, V-vector, where V forms from the W^+ decay products), supporting the idea that these decay rates are enhanced relative to D→PP decays.

DEDICATION

To

P.T. Bapu - whose guidance, encouragement, and confidence in me set me on the right path.

and

Shirley - whose support, understanding and love have **kept** me on the right path.

Acknowledgements

I thank the members of the E691 collaboration for conducting an excellent experiment:

from - University of California, Santa Barbara, California, USA
A.Bean, T.Browder, J.Duboscq, S.McHugh, R.Morrison, J.Raab, M. Witherell

from - Carleton University, Ottawa, Ontario, Canada
P. Estabrooks, J.Pinfold, J.Sidhu

from - Centro Brasileiro de Pesquisas Fisicas, Rio de Janeiro, Brazil
J.Anjos, A.Santoro, M.Souza

from - University of Colorado, Boulder, Colorado, USA
L.Cremaldi, J.Elliott, M.Gibney, U.Nauenberg

from - Fermi National Accelerator Laboratory, Batavia, Illinios, USA
J. Appel, L.Chen, P.Mantsch, T.Nash, M.Purohit, K.Sliwa, M.Sokoloff, W.Spalding, M.Streetman

from - National Research Council, Ottawa, Ontario, Canada
M.Losty

from - Universidade de São Paulo, São Paulo, Brazil
C.Escobar

from - University of Toronto, Toronto, Ontario, Canada
S.Bracker, G.Hartner, B.Kumar, G.Luste, J.Martin, S.Menary, P.Ong, A.Stundzia

from - Yale University, New Haven, Connecticut
P. Karchin

I also thank my advisors, for whom it has been pleasure to work with:

Randy Johnson - for keeping physics **FUN** and for letting me make the mistakes.

Mike Sokoloff - for instilling motivation, careful attention to detail and for his many physics lessons.

I also thank them for their **thorough** editing of this thesis!

I thank the other members of my committee, Rohana Wijewardhana and Howard Jackson

I thank the National Science Foundation for supporting this research.

I thank Ferando Barrios for his constant friendship, eagerness to help, and his ability to "work" the system. I wish him luck and success at his new position in D.C.

I thank Helen Rucker and John and Lori Gevedon for their guidance and help when I needed it.

I thank the U.C. HEP group, especially Augusto for his friendship and patient ear.

Many thanks to my family for their love and support, especially Mary and Dale Werts and Rosemary and Dick Shoup who **invested** in my future.

I thank and cherish Mindy and Becky for their love.

Finally, most of all I thank my wife Shirley for so many countless things.

Contents

List of Figures

List of Tables

1 Introduction

Almost half of all charged D meson decays involve at least one neutral kaon ($\overline{K^0}$), as do about one-third of all neutral D meson decays. These decays allow one to explore fundamental processes which affect the weak interactions of almost all particles. These processes include the bare weak decay mechanisms, strong final state interactions, and weak interference effects. The standard model of Glashow [Gl61], Salam [Sa68], and Weinberg [We67], which is a quantum field theory based on local gauge symmetries, has explained most experimental measurements involving weak interactions.

In this thesis I will discuss measurements of some D^0, D^+ and D_s^+ decays which aid in the understanding of the strong interaction mechanisms. The results are based on the full (10^8-events) data sample of the Fermilab photoproduction experiment E691. In this chapter, I describe the theoretical framework; in Chapter 2 I discuss the experimental setup used by E691; in Chapter 3 I review our methods of data collection and reconstruction; in Chapters 4 and 5 I detail the methods and results of the analyses; and in Chapter 6 I conclude the thesis with a summary of the knowledge gained from these measurements.

1.1 Historical Perspective

To explain the large suppression of flavor-changing neutral weak currents observed in decays like $K_L^0 \to \mu^+\mu^-$, Glashow, Iliopoulos, and

Maiani [Gl70] re-introduced[†] a fourth quark, the charm quark (c). In this explanation, called the GIM mechanism, the c quark couples to the weak isospin eigenstate $s' = s \cdot \cos\theta_C - d \cdot \sin\theta_C$ which is orthogonal to the eigenstate which couples to the u quark, $d' = s \cdot \sin\theta_C + d \cdot \cos\theta_C$. With this mechanism, flavor-changing neutral currents are eliminated from first order processes. To suppress these neutral currents to the level observed, second order processes must also be suppressed by requiring that the c quark mass be a few GeV [Gl70].

Charm quark physics began with the discovery of the J/ψ as a narrow enhancement in both p-Be and e^+e^- collisions [Au74, Au74a]. Its mass (3.1 GeV) is sufficient for the interpretation of a $c\bar{c}$ bound state. It has a narrow width because its mass is less than threshold for decaying directly to openly charmed particles. The only allowed decays are via $c\bar{c}$ annihilation. The discoveries of the explicitly charmed particles, D° and D^+, followed in 1976 [Go76].

1.2 Decays of D Mesons

Charmed particles are hadrons which contain at least one c quark. In the six quark standard model there are five stable, charmed, pseudoscalar mesons[††] and 21 stable, charmed spin-1/2 baryons. Of the five mesons, three have been seen experimentally and their properties are listed in Table 1.2.

[†] It was first proposed in 1964 [Bj64] for purely esthetic reasons - to preserve equality between the number of quarks and leptons.

[††] They are the D°, D^+, D_S^+, B_C^+, T_C° and their antiparticles. The $c\bar{c}$ meson, η_C, is not a stable meson.

Meson	Quark Content	Mass (MeV)	Lifetime (sec x10^{-13})
D°	$c\bar{u}$	1864.5 ± 0.5	4.21 ± 0.10
D^+	$c\bar{d}$	1869.3 ± 0.4	10.62 ± 0.28
D_s^+	$c\bar{s}$	1968.8 ± 0.7	$4.45^{+0.35}_{-0.29}$

Table 1.1 Properties of experimentally observed charmed mesons

The decays of D mesons are governed by the weak charged current (mediated by the W^+ and W^- bosons). For D decay physics, the weak current can be approximated by the two generation form†

$$J_\mu = (\bar{u}\,\bar{c})\,\gamma_\mu\,(1 - \gamma_5)\,U\begin{pmatrix} d \\ s \end{pmatrix} \qquad (1.1)$$

where U is the unitary Cabibbo mixing matrix given by

$$U = \begin{pmatrix} V_{ud} & V_{us} \\ V_{cd} & V_{cs} \end{pmatrix} = \begin{pmatrix} \cos\theta_c & \sin\theta_c \\ -\sin\theta_c & \cos\theta_c \end{pmatrix}, \qquad (1.2)$$

and θ_c is the Cabibbo angle. The value of $\sin\theta_c$ was originally measured in strange particle decays. Its current value is 0.2205 ± 0.0018 [Be90]. Decay rates are proportional to the transition matrix squared and therefore are proportional to factors of $\sin^2\theta_c$ for "Cabibbo suppressed" decays and $\cos^2\theta_c$ for "Cabibbo allowed" decays. Cabibbo allowed decays are favored over Cabibbo suppressed decays by a factor of $\sim |\cos\theta_c / \sin\theta_c|^2 \approx 20$ and therefore dominate charm decays.

† See reference [Ko73] for extension to 3 generations of quarks

1.2.1 D decay mechanisms and lifetimes

The dominant [Ba87] D decay mechanisms are represented by the spectator diagrams of Figures 1.1a (outer-W) and 1.1b (inner-W). In these decays, the light "spectator" $\bar{q}$ plays no direct role in the weak interaction. Neglecting quark recombination effects (discussed below) the "decay" of the c quark in spectator diagrams is similar to muon decay and thus occur at a rate proportional to m_c^5 [Re90 p. 416]. If the spectator diagrams were the only decay mechanisms, all the D mesons should have very similar lifetimes, contrary to the measurement $\tau_{D^+}/\tau_{D^\circ}=2.52\pm0.09$ [An87]. Two possible explanations for the D° and D^+ lifetime difference are destructive interference (discussed in section 1.2.2) and decay mechanisms which are available to the D° and not the D^+.

The W-exchange diagram, shown if Figure 1.1c, is allowed for D° mesons and not for D^+'s. This might explain the shorter D° lifetime. This amplitude involves a factor $\psi(0)$, corresponding to the probability of finding the c and $\bar{u}$ quarks at the same point. If the hadronic radius is not very sensitive to m_c then $|\Psi(0)|^2 << m_c^3$ which is smaller than m_c^5 for spectator decays [Re90 p. 416]. The W-exchange diagram is also expected to be helicity-suppressed (as in the decay $\pi^+\rightarrow e^+\nu_e$) [Re90], although this suppression may be reduced by emission of soft gluons at the $W^+\rightarrow u\bar{q}$ vertex.

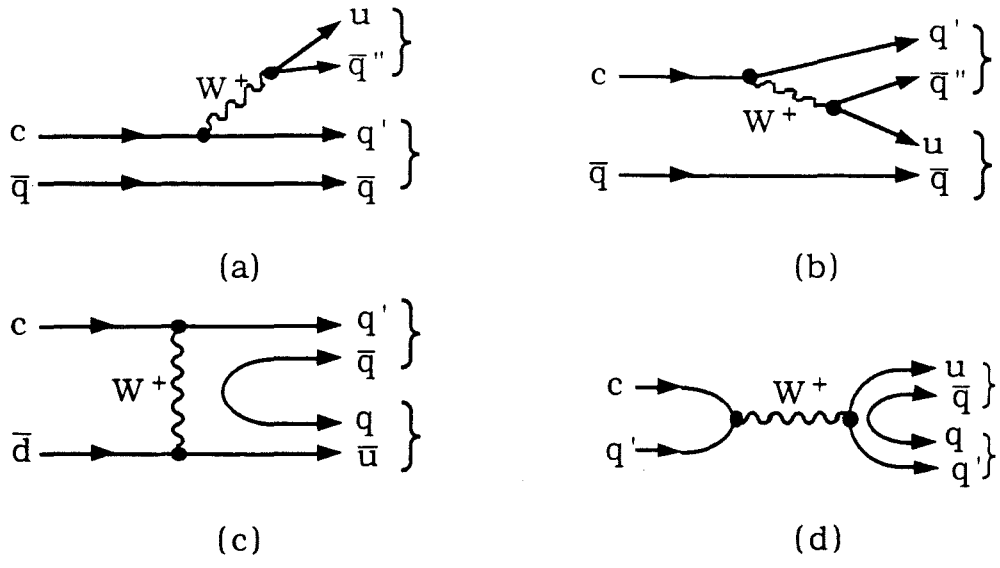

Figure 1.1 D decay mechanisms (a) Outer-W spectator, (b) Inner-W spectator, (c) W$^-$ exchange, (d) Annihilation. [q - (u,d,s); q' - (d,s); q'' - (d,s)]

The annihilation diagrams of Figure 1.1d are possible only for D^+ and D_s^+ decays. As for the W-exchange diagrams for D°'s, they may be small relative to spectator decays from the factor $|\Psi(0)|^2 << m_c^3$ and from their own helicity suppression.

The relative contributions each of the above decay mechanisms make to D meson widths cannot be ascertained from just the lifetimes and a several branching ratio measurements. Detailed studies of many decay channels need to be made to gain a complete understanding. QCD processes, like those described below, also must be considered.

1.2.2 Quark recombination

Bound states of quarks are always colorless. In mesons, the antiquark must carry the anticolor of the quark. In the case of Figure

1.1b, the $u\bar{q}''$ quarks from the W must carry the same color and anticolor as the $c\bar{q}$ quarks in the initial meson. This leads to a color suppression of diagrams like in Figure 1.1b since the quark colors only "accidentally" matchup one-third of the time [Do86, Ba87]. However, this suppression can be reduced by processes like those illustrated in Figure 1.2. In these processes a soft gluon swaps the colors of the c or q' quark with the u quark from the W. Thus the u quark will combine with the spectator quark $\bar{q}$ and the q' quark will combine with the $\bar{q}''$.

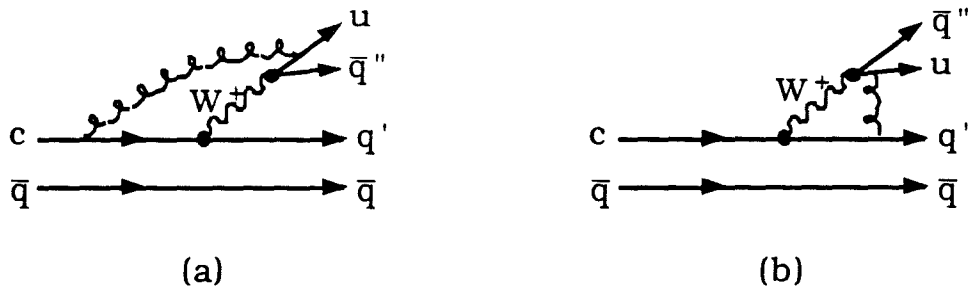

(a) (b)

Figure 1.2 Examples of first-order gluon exchange in spectator diagrams.

Destructive interference is another possible explanation for the D^0-D^+ lifetime difference. Consider the spectator diagrams of Figure 1.1a and 1.1b, redrawn for the decay $D^+ \rightarrow \overline{K}^0\pi^+$ in Figure 1.3. The final states of the two diagrams are identical. This is not true for D^0 decays. If there is destructive interference between these two amplitudes, then the D^+ lifetime will be lengthened. Calculations of the effects of hard gluons [Ba87, Bu86] show that the two amplitudes are relatively negative, supporting destructive interference.

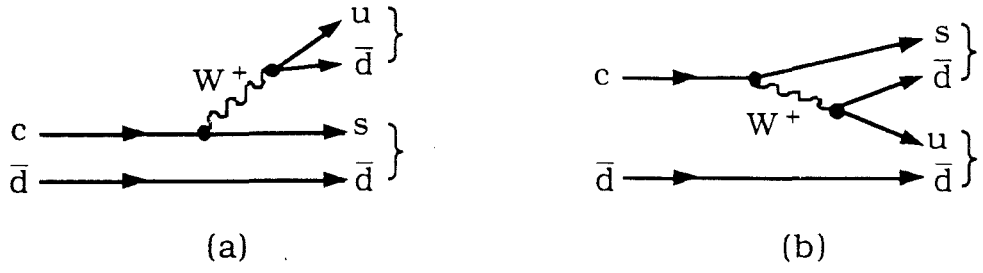

Figure 1.3 Two diagrams of the decay $D^+ \rightarrow \overline{K}^\circ \pi^+$

While the decay of the charm quark is a weak interaction and can be treated perturbatively, the formation of the hadrons from the resulting quarks is a strong, nonperturbative process. Final state interactions, the strong interactions of particle formation, may complicate the simple quark model interpretations of experimental results. The two classes of these interactions are: "elastic" - interactions which preserve quark flavors, and "inelastic" - ones which can change quark flavors. Both can change the relative rates of the various weak decay mechanisms.

As an example of final state interactions, consider the decay $D^\circ \rightarrow \overline{K}^\circ \phi$. Bigi [Bi80] has argued that this decay mode demonstrates the existence and perhaps dominance of W-exchange diagrams in D decays. While this final state may be produced via a W-exchange decay (Figure 1.1c with q' and q both s quarks), it can also be produced through a *normal* spectator diagram followed by inelastic final state interactions [Do86], as illustrated in Figure 1.4.

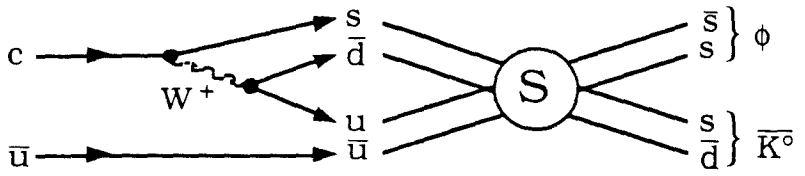

Figure 1.4 Production of $D^0 \to \overline{K^0}\phi$ from final state interactions.

Quark recombination effects must be understood to extract from experimental data the relative contributions of the weak mechanisms. The level of significance of recombination effects can be determined by measuring the decay rates of mesons into final states produced largely by these effects, and comparing them to better *understood* rates. The decays $D^0 \to K^-\pi^+$, $D^0 \to \overline{K^0}\pi^0$ and $D^+ \to \overline{K^0}\pi^+$ can be used to investigate color suppression and elastic final state interactions (see section 1.4.1) and the decay $D^0 \to \overline{K^0}K^0$, when compared with $D^0 \to K^+K^-$ and $D^0 \to \pi^+\pi^-$, can be used to explore inelastic final state interactions (see section 1.4.2).

1.3 Theoretical Framework

When strong interactions are neglected in the four quark Standard Model, the purely hadronic part of the charm-changing term (corresponding to Figure 1.1a) in the weak Lagrangian is given by

$$\mathcal{L}_{eff} = \frac{G_F}{\sqrt{2}} V_{cs} V_{ud} (c\bar{s})(d\bar{u})^{\dagger} \qquad (1.3)$$

---

† In (1.3) and for the rest of this section, I will use only the Cabibbo allowed terms to simplify the discussion.

where G_F is the Fermi constant and $(c\bar{s}) = c\gamma^{\mu}(1 - \gamma^5)\bar{s}$, etc. QCD corrections to this term like gluon radiation (similar to QED radiative corrections) and gluon exchange between quarks (like Figure 1.2) can be summed and their net effect is to add an additional term to the Lagrangian. The new Lagrangian is [Re90 p. 423]

$$L'_{eff} = \frac{G_F}{\sqrt{2}} V_{cu} V_{ud} \left[\frac{(c_+ + c_-)}{2}(c\bar{s})(d\bar{u}) + \frac{(c_+ - c_-)}{2}(c\bar{u})(d\bar{s}) \right] \qquad (1.4)$$

where

$$c_{\pm} = \left[\frac{\alpha_S(M_W^2)}{\alpha_S(M_c^2)} \right]^{\gamma_{\pm}} \qquad \gamma_+ = -\frac{1}{2}\gamma_- = \frac{2}{11 - \frac{2}{3}n_F}, \qquad (1.5)$$

and M_W is the W boson mass and n_F is the number of quark flavors [Bi88,Bu86]. In the first term the c and s quarks have the same color, which causes the s quark to combine with the spectator quark (like Figure 1.1a). The second term has the s and u quarks interchanged, reflecting that the c and u quarks have the same color. This causes the u quark to combine with the spectator quark (like Figure 1.1b). In the limit of $\alpha_s \rightarrow 0$, $c_+ = c_- = 1$ and the second term vanishes.† With $\Lambda_{QCD} = 150$ MeV, $m_c = 1.5$ GeV, and $c_+ = 0.8$ and $c_- = 1.6$.

† This does not mean the amplitude for the diagram of Figure 1.1b is zero, just that the QCD induced contribution vanishes. There still may be a contribution from the probability that the quark colors "incidentally" match up as in Figure 1.1b.

1.3.1 The Bauer, Stech, and Wirbel Model

Bauer, Stech, and Wirbel [Ba87] developed a theoretical approach (BSW approach) which allowed them to compute many D and B meson two-body decay rates. Their method starts with the effective Lagrangian of (1.4). They form all possible two-body decay diagrams with different topologies (as in Figures 1.1a and 1.1b). Using their approach, a D decay transition amplitude is given by

$$T(D \rightarrow f) \propto \alpha_1 \langle f | (c\bar{s})_H (d\bar{u})_H | D \rangle + \alpha_2 \langle f | (c\bar{u})_H (d\bar{s})_H | D \rangle, \quad (1.6)$$

where $| D \rangle$ and $\langle f |$ are the initial and final states, and

$$\alpha_1 = \frac{(c_+ + c_-)}{2} + \xi \frac{(c_+ - c_-)}{2}$$
$$\alpha_2 = \frac{(c_+ - c_-)}{2} + \xi \frac{(c_+ + c_-)}{2}. \quad (1.7)$$

They replace the quark currents in the Lagrangian by hadronic currents denoted by $(\ )_H$ in equation (1.6). The α_1 term corresponds to the diagram of Figure 1.1a and the α_2 term to Figure 1.1b. ξ is a free parameter in this treatment which is called the "color mismatch factor". ξ represents the probability that the quarks recombine as in Figure 1.1b without the benefit of the QCD induced term in (1.4).

A crucial assumption in the BSW approach is that the transition amplitudes factorize into pairs of matrix elements [Bi88]. For final states f = PP, PV, VP, and VV (P = pseudoscalar, V = vector) the factorization is

$$\langle f | (c\bar{s})_H (d\bar{u})_H | D \rangle \approx \langle P,V | (d\bar{u})_H | 0 \rangle \langle P,V | (c\bar{s})_H | D \rangle. \quad (1.8)$$

The first factor on the right-hand-side of (1.8) gives the strength of coupling the $(d\bar{u})$ current (from the W boson) to a P or V meson. The second factor is the strength of coupling the s and spectator quarks to a P or V meson. As an example, consider the decay $D^\circ \rightarrow K^-\pi^+$. Its factorization is

$$\langle K^-\pi^+ | (c\bar{s})_H (d\bar{u})_H | D^\circ \rangle \approx \langle \pi^+ | (d\bar{u})_H | 0 \rangle \langle K^- | (c\bar{s})_H | D^\circ \rangle. \quad (1.9)$$

The first factor is proportional to f_π , which is the strength of coupling of the π^+ to the $d\bar{u}$ current.

The BSW approach incorporates W-exchange and annihilation processes (Figures 1.1c and 1.1d) and final state interactions. Annihilation processes are expected to be small due to helicity suppression [Re90 p. 388], although soft gluons inside hadrons can lead to momentum and angular momentum exchanges between gluons and hadrons which reduce this suppression [Fa78, Ca78]. Elastic final state interactions are incorporated into the BSW predictions by comparing the isospin amplitudes of the decays $D^\circ \rightarrow K^-\pi^+$, $D^\circ \rightarrow \overline{K^\circ}\pi^\circ$ and $D^+ \rightarrow \overline{K^\circ}\pi^+$ with experimental data on these decays. Only low levels of inelastic final state interactions are included in this approach [Ba87].

Bauer, Stech, and Wirbel find that the best values for α_1 and α_2 are 1.3±0.1 and -0.55±0.1 with correlated errors [Ba87]. These

values agree well with typical c_+ and c_- values if $\xi = 0$. Thus, they conclude that direct color matching is necessary in forming mesons.

1.4 Final State Interactions and D Decay Modes

1.4.1 $D^\circ \to \overline{K}^\circ \pi^\circ$ and $D^+ \to \overline{K}^\circ \pi^+$ modes

The rates for $D^\circ \to \overline{K}^\circ \pi^\circ$, $D^+ \to \overline{K}^\circ \pi^+$, when used in conjunction with those for $D^\circ \to K^- \pi^+$, may indicate the strength of elastic final state interactions. All three modes are dominated by spectator decays: $D^\circ \to \overline{K}^\circ \pi^\circ$ by an inner-W (Figure 1.5a), $D^\circ \to K^- \pi^+$ by an outer-W (Figure 1.5b), $D^+ \to \overline{K}^\circ \pi^+$ by an outer- and inner-W (Figures 1.5c and 1.5d). Decomposing these decay matrices into isospin amplitudes yields:

$$A(D^+ \to \overline{K}^\circ \pi^+) = A_{\frac{3}{2}} e^{i\delta_{\frac{3}{2}}},$$

$$A(D^\circ \to K^- \pi^+) = \frac{1}{3}(A_{\frac{3}{2}} e^{i\delta_{\frac{3}{2}}} + \sqrt{2} A_{\frac{1}{2}} e^{i\delta_{\frac{1}{2}}}), \text{ and}$$

$$A(D^\circ \to \overline{K}^\circ \pi^\circ) = \frac{1}{3}(\sqrt{2} A_{\frac{3}{2}} e^{i\delta_{\frac{3}{2}}} - A_{\frac{1}{2}} e^{i\delta_{\frac{1}{2}}}) \qquad (1.10)$$

Theses relations satisfy the sum rule

$$\sqrt{2} A(D^\circ \to \overline{K}^\circ \pi^\circ) = A(D^+ \to \overline{K}^\circ \pi^+) - A(D^\circ \to K^- \pi^+). \qquad (1.11)$$

The branching ratios for these three decays will allow the determination of the two magnitudes of the isospin amplitudes and complex phase difference between them. The same isospin decomposition can also be applied to the $K^*\pi$ and $K\rho$ modes. The

same magnitudes $A_{\frac{1}{2}}$ and $A_{\frac{3}{2}}$ can be used for these modes, but, in principal, the complex phases will be different.

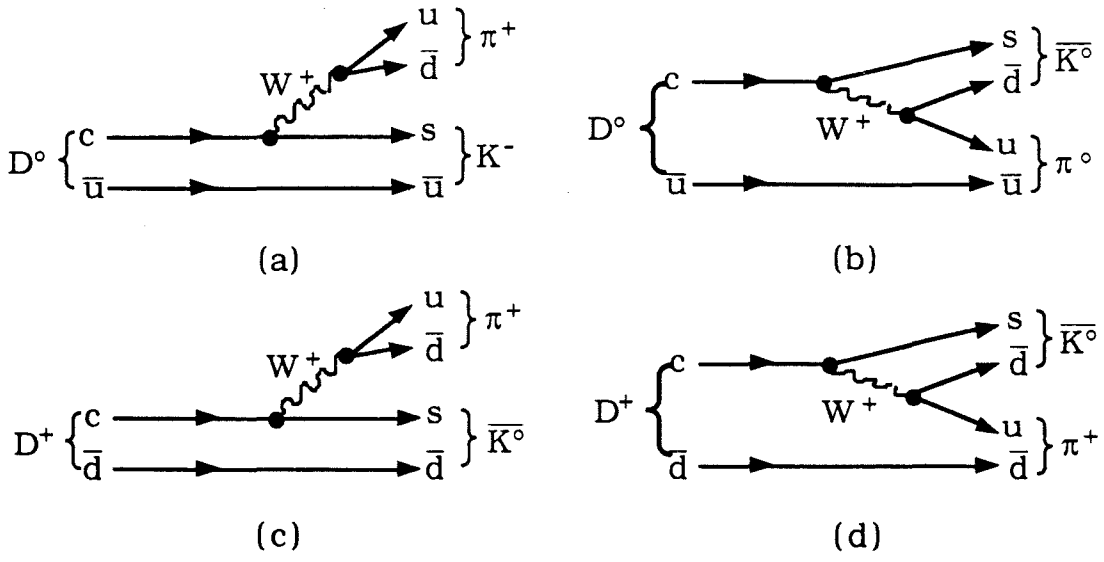

Figure 1.5 Decay diagrams for $D^\circ \to \overline{K}^\circ \pi^\circ$, $D^+ \to \overline{K}^\circ \pi^+$ and $D^\circ \to K^- \pi^+$.

1.4.2 $D^\circ \to \overline{K}^\circ K^\circ$ mode

A D° cannot decay directly into a $\overline{K}^\circ K^\circ$ pair via a spectator diagram because there is no $\bar{u}$ quark in the final state. The two different W-exchange diagrams of Figures 1.6 could contribute, but their amplitudes cancel each other through the GIM mechanism [Gl70] in the absence of SU(2) flavor symmetry breaking [Ph87]. While such symmetry breaking can occur either through differences in the probability of a $d\bar{d}$ or $s\bar{s}$ popping up from the vacuum or through a difference in the helicity suppression of coupling a W vector boson to an s quark relative to that of coupling to a d quark, it is expected to be

small. Therefore a large decay rate of $D^\circ \to \overline{K}^\circ K^\circ$ indicates inelastic final state interactions are present.

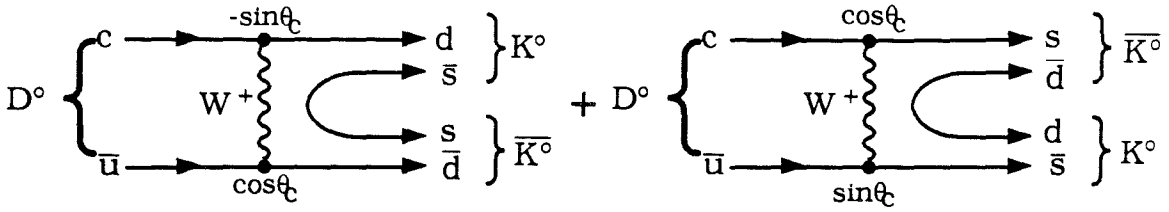

Figure 1.6 W-exchange diagrams which could contribute to the decay $D^\circ \to \overline{K}^\circ K^\circ$.

The $\overline{K}^\circ K^\circ$ final state can be produced with inelastic final state interactions as illustrated in Figure 1.7. The big S represents a hadronic interaction which changes the $u\bar{u}$ pair into a $d\bar{d}$ pair. If the $D^\circ \to \overline{K}^\circ K^\circ$ decay proceeds at a rate similar to other equivalent Cabibbo-suppressed decays, inelastic final state interactions must be significant. If the rate is well below Cabibbo-suppressed levels, this decay could be explained by SU(2) flavor symmetry breaking and there would be no need to invoke final state interactions.

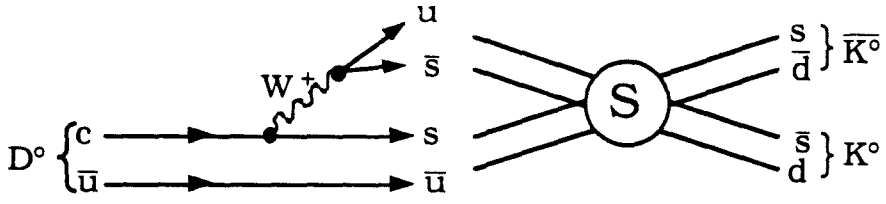

Figure 1.7 Spectator diagram and final state interactions which could contribute to the decay $D^\circ \to \overline{K}^\circ K^\circ$.

1.4.3 $D^\circ \to \overline{K^\circ}\overline{K^\circ}K^\circ$ mode

The decay $D^\circ \to \overline{K^\circ}\overline{K^\circ}K^\circ$ is Cabibbo allowed and cannot be produced by spectator diagram alone because there is no $\bar{u}$ quark in the final state. Three possible mechanisms that could produce this final state are shown in Figure 1.8. The first mechanism is a W^- exchange diagram where $d\bar{d}$ and $s\bar{s}$ pairs pop up from the vacuum†. The second mechanism is an inner-W spectator decay with an $s\bar{s}$ pair popping up from the vacuum, followed by final state interactions rescattering the $u\bar{s}$ and $\bar{u}s$ pairs into $d\bar{s}$ and $\bar{d}s$ pairs of the $\overline{K^\circ}$ and K°. The third mechanism also involves an inner-W spectator decay, in which the $u\bar{u}$ pair rescatter, possibly through a resonance state such as the a_0, into the final state $\overline{K^\circ}K^\circ$.

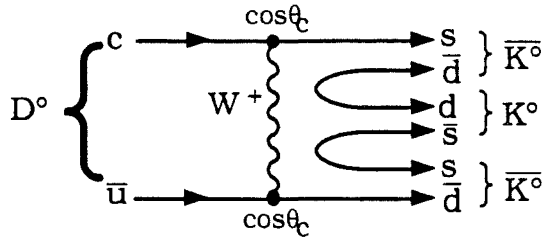

(a)

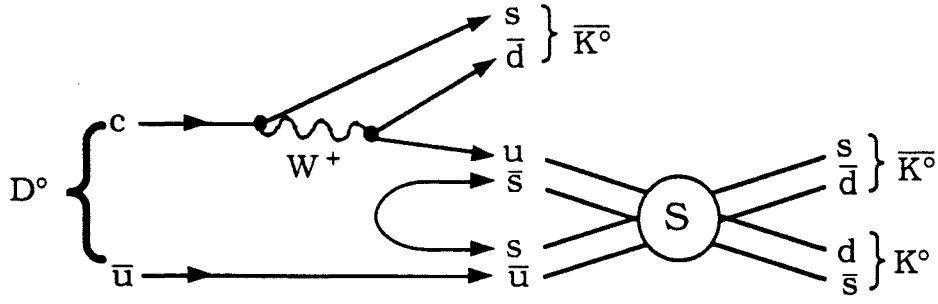

(b)

† This is similar to the process for $D^\circ \to \phi\overline{K^\circ}$ invoked earlier as an indicator of the existence of W-exchange diagrams.

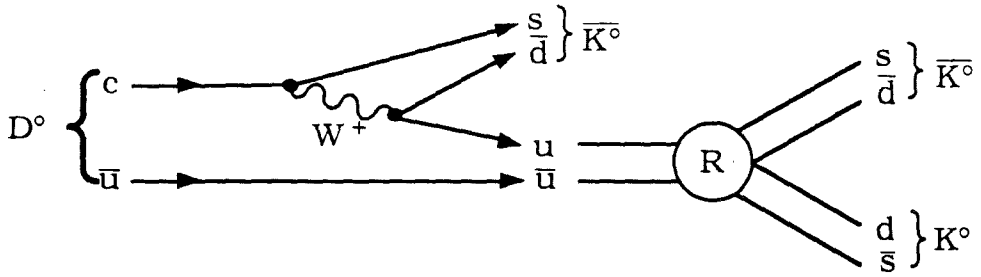

(c)

Figure 1.8 Possible mechanisms for the decay $D^\circ \rightarrow \overline{K^\circ}\,\overline{K^\circ}K^\circ$.

1.4.4 $D^+ \rightarrow \overline{K^\circ}K^{*+}$ mode

A possible decay mechanism for the decay $D^+ \rightarrow \overline{K^\circ}K^{*+}$ is a Cabibbo suppressed outer-W spectator decay, as shown in Figure 1.9. It is of the form P→PV where the V particle (K^{*+}) forms directly from the W vector boson. The rates for P→PV decays relative to the corresponding P→PP decays are enhanced for both Cabibbo allowed and suppressed decays [He90]:

$$\frac{Br(D^\circ \rightarrow K^-\rho^+)}{Br(D^\circ \rightarrow K^-\pi^+)} = 2.1 \pm 0.3$$

$$\frac{Br(D^+ \rightarrow \overline{K^\circ}\rho^+)}{Br(D^+ \rightarrow \overline{K^\circ}\pi^+)} = 2.4 \pm 0.7$$

$$\frac{Br(D^\circ \rightarrow K^-K^{*+})}{Br(D^\circ \rightarrow K^-K^+)} = 1.8 \pm 0.9. \qquad (1.12)$$

Since the branching ratio for $D^+ \rightarrow \overline{K^\circ}K^+$ is (0.84±0.27)%, the branching ratio for $D^+ \rightarrow \overline{K^\circ}K^{*+}$ may be 1.5 to 2.0%.

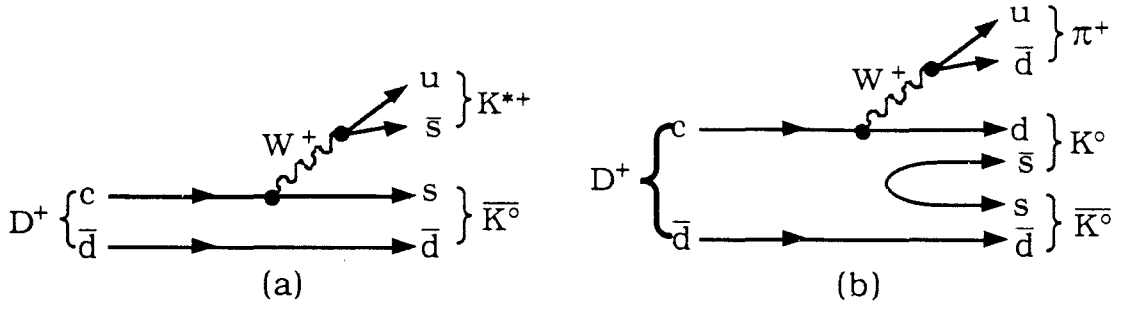

Figure 1.9 Decay mechanisms for (a) $D^+ \to \overline{K^0} K^{*+}$ and (b) $D^+ \to \overline{K^0} K^0 \pi^+$ non-resonant.

1.4.4 $D_s^+ \to \overline{K^0} K^{*+}$ mode

The decay $D_s^+ \to \overline{K^0} K^{*+}$ is also of the form P→PV. However, here the V particle (K^{*+}) does not form directly from the W vector boson and may not lead to the enhancement seen in other P→PV decays. This D_s^+ decay is Cabibbo allowed and may be produced through an inner-W spectator and/or an annihilation mechanism as illustrated in Figure 1.10. The annihilation amplitude may be small as seen in $BR(D_s^+ \to \rho \pi^+) < .21\%$ [He90] which can only proceed through annihilation.

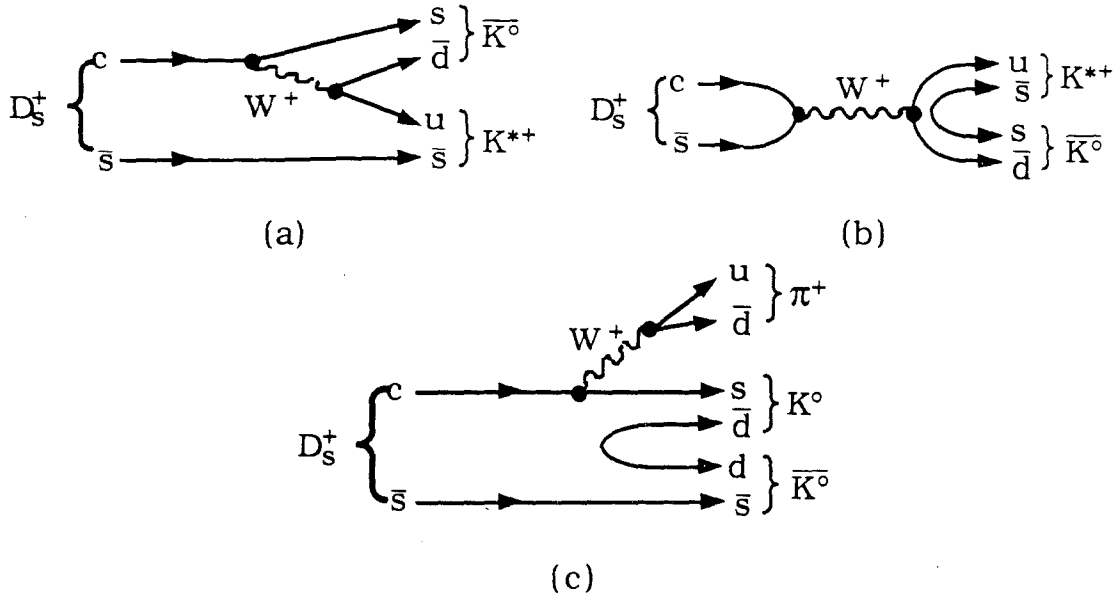

Figure 1.10 Decay mechanisms for (a,b) $D_s^+ \to \overline{K^\circ} K^{*+}$ and (c) $D_s^+ \to \overline{K^\circ} K^\circ \pi^+$ non-resonant.

1.5 Physics Summary

The above discussions described several aspects of weak decays of charmed particles which have yet to be thoroughly understood. Specifically, to understand quark recombination affects such as color suppression or hadronic final state interactions, detailed measurements of decay rates which are sensitive to these affects must be made. The results presented in Chapter 5 supply a few such measurements.

2 Experimental Setup

2.1 Fermilab Experiment E691

Experiment E691 is a second generation photoproduction experiment optimized to study charm particle production and decays. Its predecessor, experiment E516, is described in [Su84]. The experiment was conducted at the Tagged Photon Laboratory (TPL) of the Fermi National Accelerator Laboratory (Fermilab) in Batavia, Illinois. Several upgrades were incorporated into the Tagged Photon Spectrometer (TPS) between the E516 run and the E691 run. The most important upgrade was the addition of silicon microstrip detectors described in section 2.3.1. Concurrent to these TPS upgrades, the Tevatron proton beam energy was increased from 400 to 800 GeV. This increase resulted in raising the maximum energy of the photon beam from 170 to 260 GeV and resulting in a concomitant increase in the charm production rate [An89]. The duty cycle of the machine was also increased by a factor of 3.7 (22 seconds every minute from 1 second every 10). Both of these factors increased the rate at which E691 could take data. More complete descriptions of the detector, of our particle-identification and vertexing algorithms, and of related results are found in [Ra87, Br88] and references therein.

2.2 Photo-Production and Detection of Charm

The photoproduction of charm (charm produced by the interaction of high energy photons with nucleons) can be described by the Photon-Gluon Fusion model [Jo78, Fo81]. In the lowest order

process, shown in Figure 2.1a, the hadronic component of the photon scatters from a gluon in a target nucleon, converting both into a *real* charm-anticharm quark pair. The apparent violation of parity and color conservation of this process can be overcome by considering soft gluon radiation. Higher order processes like those in Figure 2.1b and 2.1c conserve parity and color. Combining quarks into hadrons can be modeled using the phenomenological framework of Feynman-Field, LUND, or the Cluster model [Go84, An83].

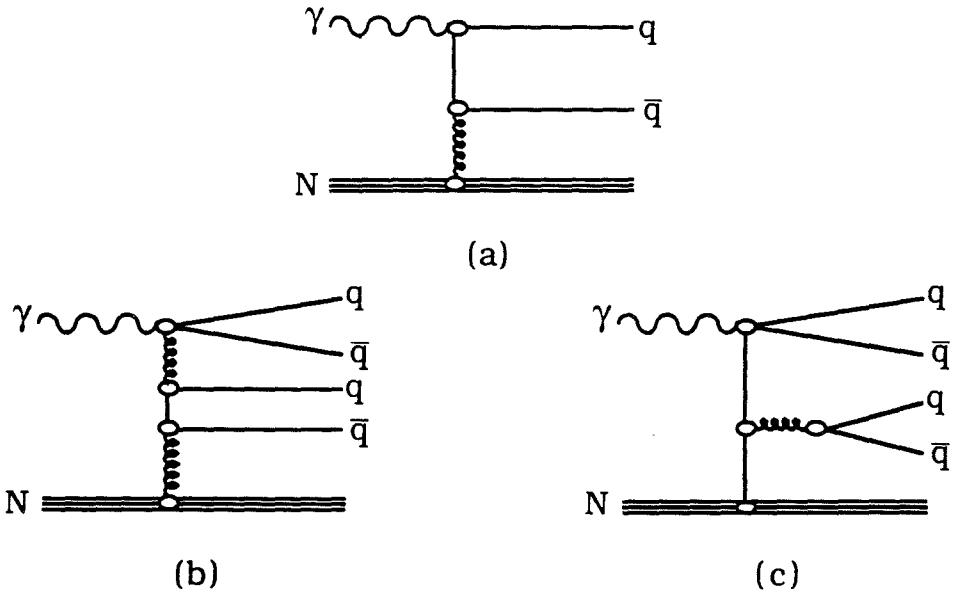

Figure 2.1 Photon-Gluon Fusion: (a) lowest order, (b) and (c) higher orders

The detection of charmed particles requires high luminosities (to compensate for small cross sections) and a large suppression of combinatorial backgrounds. The charm fraction of the hadronic cross section is only 0.5% This small† fraction is offset by an average luminosity of ~ 4.1×10^5 $cm^{-2}s^{-1}$. The large combinatorial background

† relative to comparable e^+e^- experiments.

is from an average charged track multiplicity of 10 tracks/event and from most events being non-charmed. This background can be reduced by exploiting the relatively long lifetime of charmed particles. A D° with momentum 60 GeV (typical of this experiment) will travel typically 0.36 cm before decaying, a measurable distance using silicon microstrip detectors (SMD's).† Another background reduction for D° measurements was gained by using only D° candidates consistent with the hypothesis $D^{*+} \rightarrow D^{\circ}\pi^{+}$. Requiring the D*-D° mass difference to be "close" to 0.147 GeV reduced backgrounds by 50 (see section 5.1.1).

2.3 Photon Beam & Tagging System

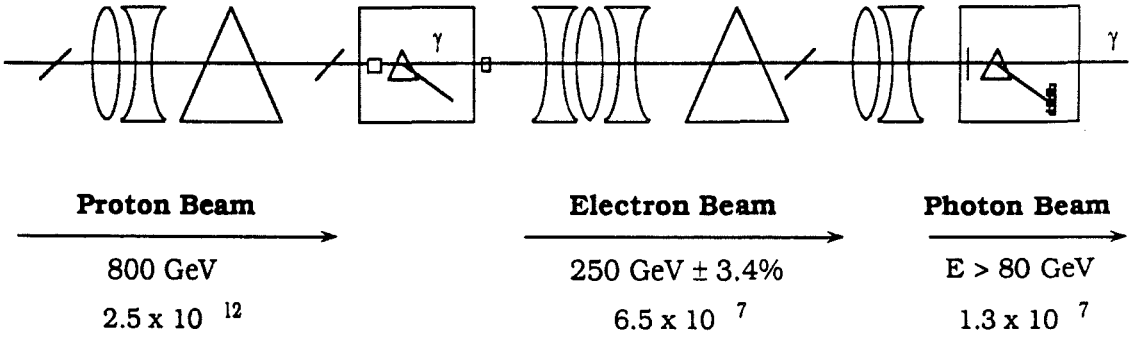

Figure 2.2 Beam transport system: $p \rightarrow \pi^{\circ}(X) \rightarrow \gamma\gamma \rightarrow e^{-}(e^{+}) \rightarrow \gamma$.

Our photons were generated in four steps, as illustrated in Figure 2.2. Protons of 800 GeV energy were extracted from the Tevatron at a rate of 10^{13} per spill. They interacted in a 30 cm long beryllium target and produced secondaries. The charged secondaries

† first developed at CERN [He81].

were swept aside by magnets into a beam dump, leaving only neutrals such as kaons, neutrons, and photons. Some of the photons converted into electron-positron pairs in a lead radiator. The electrons were momentum analyzed, collimated and transported to TPL. The electron beam energy could be tuned to values from 10 to 300 GeV. Their energy spread was ± 3.5%. At the entrance to TPL, one 260 GeV electron arrived for each 40K protons incident on target. Upon entering TPL, the electrons encountered a .2 radiation length tungsten foil. Because the characteristic emission angle of bremsstrahlung photons is given approximately by $\frac{1}{\gamma} = \frac{m_e}{E_e} \approx 10^{-3}$, the photons radiated by the electrons were well collimated with beam transverse sizes of $\sigma_x \sim 0.8$ cm and $\sigma_y \sim 1.8$ cm. After radiating, the electrons were deflected by three bending magnets into the electron tagging system while the photons went straight ahead into the E691 target.

The electron tagging system, diagrammed in Figure 2.2, had two purposes: 1) to determine each beam photon's energy and 2) to provide a photon signal to the trigger logic. The energy of each electron after it radiated was determined by a set of shower counters. The photon energy was then $E_{photon} = E_{beam} - E_{tag}$.

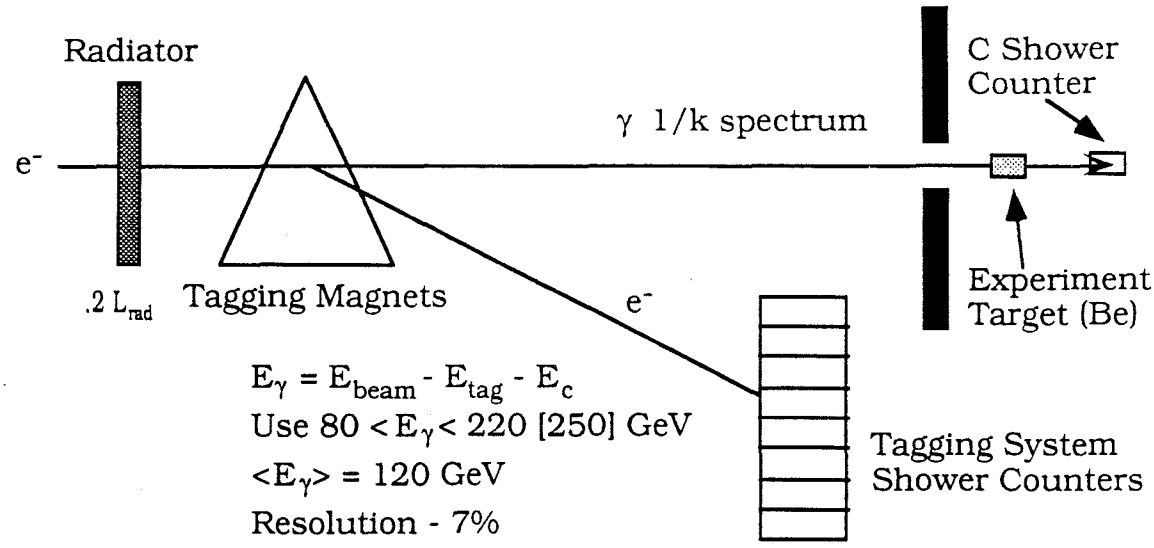

Figure 2.2 Photon Tagging System

2.4 Target

Our charmed particles were produced by interactions of beam photons with our beryllium target. Beryllium was chosen as the material that was the best compromise between the conflicting requirements of having low pair production rates, small multiple scattering, large hadronic cross sections, and good acceptance. Low pair production rates and small multiple scattering pointed to materials with low Z such as hydrogen. However, the requirements for large hadronic cross sections and good acceptance pointed to small dense targets. Our 5 cm long bar of beryllium, corresponding to 0.14 radiation lengths and 0.066 nuclear interation lengths, was located with its back face 3.8 cm from the first SMD plane (see section 2.5.1). The transverse size of 1.25 x 2.5 cm was determined by our beam dimensions.

2.5 Spectrometer

Even at our average charmed particle momentum, the short distance these particles traveled (typically 3 - 9 mm) made it impossible to detect directly. Instead, we reconstructed them from their observed decay products. We accomplished this reconstruction using the TPS which is a two magnet spectrometer that incorporates Silicon Microstrip Detectors, Drift Chambers, Cerenkov counters, calorimeters, and muon detectors. Figure 2.4 diagrams the E691 version of the TPS.

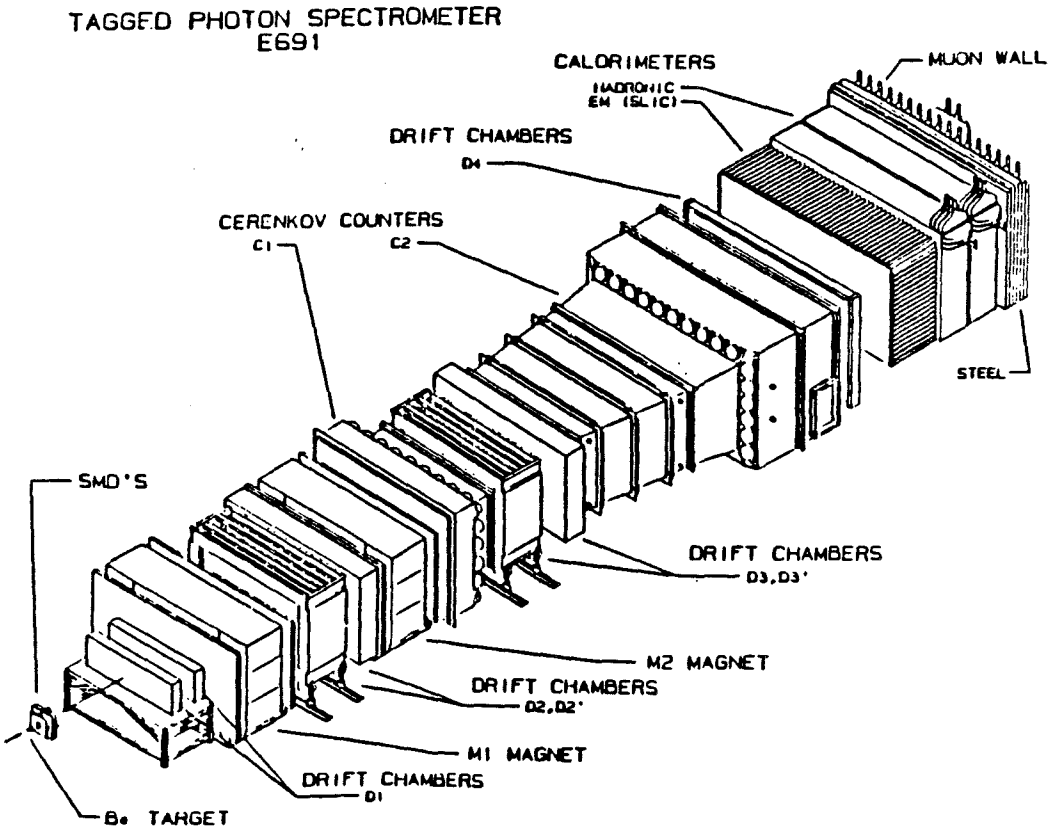

Figure 2.4 The E691 version of the TPS.

2.5.1 Silicon Microstrip Detectors

Using our SMD's, we determined the production and decay positions for charm decays with one or more charged particles. We typically reduced our background by a factor of 50 by making a cut on this separation since typical non-charm background particles came from the production point. The SMD's also provided great redundancy before the first magnet.

Each plane of the SMD's can be thought of as an array of long capacitors [Br88]. When a minimum ionizing charged particle traverses one of the capacitors, it discharges about 23000 electrons which were amplified, discriminated and read out through CAMAC serial scanners. There were a total of nine planes of SMD's arranged as show in Figure 2.5. They were mounted as three triplets, each triplet having an X, Y and V plane. The V plane was rotated by 20.5° with respect to X. This arrangement gave a stereo view. Table 2.1 gives characteristics of the SMD triplets.

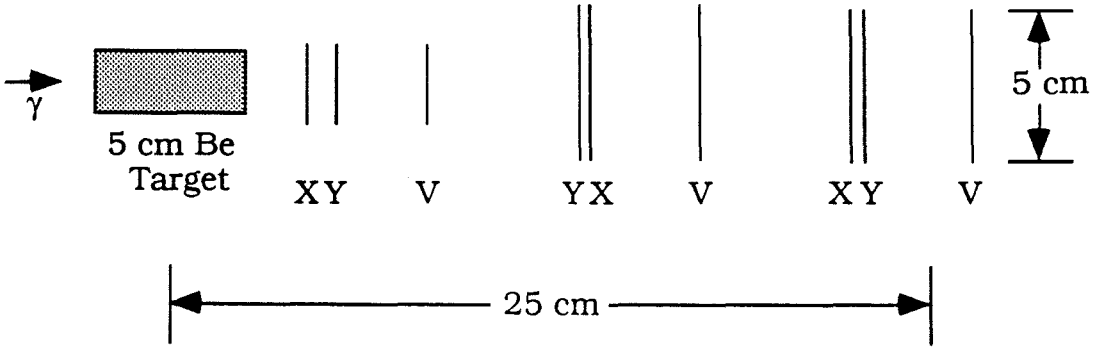

Figure 2.5 SMD plane layout

The transverse resolution of the SMD's was about 16 μm which gave us a longitudinal vertex separation resolution of about 300 μm for

a 60 GeV D meson. They were capable of operating in a high rate environment (~ 1 MHz). The average per plane efficiency was about 95%. The angular acceptance of ±100 mrad was adequate since typical tracks were contained in a cone of ±30 mrad. The SMD acceptance was also well matched to the acceptance of the rest of our spectrometer.

triplet	1	2	3
area (mm^2)	26x26	50x50	50x50
strip spacing (μm)	50	50	50
strip width (μm)	~30	~30	~30
# of instrumented strips	3x512	3x768	3x1000
plane ordering	X,Y,V	Y,X,V	X,Y,V
z-coordinates (cm)	1.931, 3.015, 6.684	11.046, 11.342, 14.956	19.915, 20.254, 23.876

Table 2.1 SMD Characteristics (adapted from [Ra87])

2.3.2 Drift Chambers

In addition to the SMD's, our charged particle tracking system included four drift chamber stations (see Figure 2.4) containing a total of 35 planes. Table 2.2 lists general characteristics of each drift chamber station. D1, the most upstream chamber, was located between the SMD's and the first magnet M1. It was divided up into two subassemblies, D1A and D1B, each of which contained four sense planes, X, U, V, X'. X and X' were in the same direction as the X

planes in the SMD's. U and V were at +20.5°, and -20.5° relative to X. X' was offset by half a cell size relative to X to eliminate left-right ambiguities. D2 contained 4 X,U,V triplets and was located between our two magnets M1 and M2. This station located the particles as they exited M1 allowing us to measure their bend and also to pin-point their entry into M2. Following M2, D3, was a scaled up version of D2 measured the particles exit point from M2. The final station, D4, was located in front of the calorimeter. It had the largest lever arm, but, unfortunately, also had the most noise coming from electromagnetic calorimeter backsplash. The noise degraded the chamber resolution which reduced its lever arm advantage.

	D1	D2	D3	D4
physical size (cm^2)	160x120	230x200	330x200	550x300
# of channels	1536	2400	1952	416
cell size U/V (cm)	0.476	0.892	1.487	2.97
cell size X (cm)	0.446	0.953	1.588	3.18
resolution (cm)	0.035	0.030	0.030	0.030

Table 2.2 Drift Chamber Characteristics (adapted from [Ra87])

2.3.3 Magnets

Two large aperture analysis magnets were used in conjunction with the drift chambers for charged particle momentum determination. The magnets also aided in charged track reconstruction by spreading the tracks laterally, decreasing the congestion in the central region. The magnetic fields pointed in the negative-y direction; so a positively (negatively) charged particle had

its positive-x (negative-x) momentum increased, called a "p_T-kick". Magnet M1 and M2 gave p_T-kicks of 0.21 and 0.32 GeV. Table 2.3 shows parameters of M1 and M2.

	M1	M2
entrance aperture (cm)	154x73	154x69
exit aperture (cm)	183x91	183x86
length (cm)	165	208
E691 current (amps)	2500	1800
$\int B_y(0,0,z)dz$ (T-m)	-0.71	-1.07
p_T kick (GeV/c)	0.21	0.32

Table 2.3 Magnet parameters (adapted from [Su84])

2.3.4 Cerenkov Counters

The two primary detector components for charged particle identification were our two threshold, Cerenkov counters, C1 and C2. The Cerenkov counters were operated at different momentum thresholds to cover a larger region of particle momenta. With ideal light collection, we could have uniquely identified pions, kaons, and protons in the 6-37, 20-37, 37-70, GeV/c momentum ranges respectively. Table 2.5 gives overall properties of our counters.

	C1	C2
length (m)	3.7	6.6
# of cells	28	32
gas	100% N2	80% He 20% N2
$\varepsilon = n-1$	290×10^{-6}	86×10^{-6}
$\gamma_{threshold}$	42	76

Table 2.4 Properties of the Cerenkov counters

2.3.5 Electromagnetic and Hadronic Calorimeters

To detect neutral particles which had not decayed into charged particles such as π°'s and η's, E691 used two calorimeters, a segmented liquid ionization calorimeter (SLIC) for electromagnetic showers and an iron scintillator sandwich calorimeter, the Hadrometer, for hadrons. The SLIC was used to identify electrons and photons and to measure their energy. Electrons were distinguished from charged hadrons by their relatively narrow showers. Photons were distinguished from electrons because no tracks lead to the photon's thin showers.

The SLIC consisted of sixty layers of 0.63 cm thick flat lead and corrugated aluminum sheets. This space between the corrugations was filled with liquid scintillator. Photomultiplier tubes (PMT's) connected to the ends of the scintillators detected the light produced in the scintillator by the particle showers. The corrugations were arranged in U, V and Y views. The U and V views were parallel to the DC U and V views to aid in linking tracks to showers.

The center of the SLIC was shielded from beam photon conversion pairs by a set of nineteen tungsten-lucite and lead-lucite shower counters, called the pair plane. This reduced the background triggers in our main transverse energy trigger (see section 3.1.1) and aided in the SLIC pattern recognition.

The Hadrometer, which was located directly behind the SLIC, measured hadronic showers. It was composed of 18 layers of 1" steel followed by 3/8" plastic scintillator. The scintillators were divided up into X and Y views, alternating in every other layer. The light output was waveshifted, detected by PMT's and then digitized. We achieved a fractional energy resolution of $75\%/\sqrt{E\,(GeV)}$ and intrinsic position resolution of less than 2".

2.3.7 Muon Walls

TPS had two large plastic scintillator walls for muon identification; the Front Muon Wall located at the entrance of the experimental hall detected externally produced muons entering the experimental area; the Back Muon Wall located behind the Hadrometer was used in our J/ψ dimuon trigger and analysis and in the muon calibration trigger.

In summary, all the major components of the TPS are listed in Table 2.5.

Detector	z-coord. (cm)	Active area x × y (cm)	Resolution
Front Muon Wall	-510.	250.×150.	
Target	-5.8*, -0.8†	1.25×2.5	
B-counter	0.0	2.5×2.5	
SMD1 SMD2 SMD3	3.0 11.3 20.3	2.6×2.6 5.0×5.0 5.0×5.0	16 μm
D1A D1B	156. 192.	86.×65. 114.×65.	350 μm
M1 (center)	286.6	174.x86.	$\Delta p/p \sim .001p$
D2-1 D2-2 D2-3 D2-4	384. 426. 468. 499.	182.×130. 182.×130. 210.×130. 228.×130.	300 μm
M2 (center)	620.6	171.×88.	$\Delta p/p \sim .0005p$
C1 mirror plane	866.	250.×130.	
D3-1 D3-2 D3-3 D3-4	930. 426. 468. 499.	254.×130. 254.×130. 254.×130. 302.×130.	300 μm
C2 mirror plane	1653.	465.×240.	
D4	1744.	508.×240.	800 μm
Pair-Scint. ctr.	1760.	100.×5.	
Pairplane	1829.*, 1839.†	174.×12.5	
SLIC	1849.*, 1951.†	490.×240.	$\frac{\Delta E}{E} \approx \frac{21\%}{\sqrt{E}}$
Hadrometer	1962.*, 2120.†	490.×270.	$\frac{\Delta E}{E} \approx \frac{75\%}{\sqrt{E}}$
Back Muon Wall Caboose DC-paddle	2235. 2385. 2300.*, 2367.†	547.×305. 33.×33. 33.×33.	

Table 2.5 Summary of the TPS components; * are upstream and † are downstream coordinates (adapted from [Ra87])

3 Data Collection, Reconstruction, and Monte Carlo Simulation

Studies of charmed particle production and decays are only possible after the collection, reconstruction, and simulation of a large data sample. Fast and efficient filtering of non-hadronic events was important to the data collection process since unwanted pair production events occur about 1000 times more frequently than hadronic events. Even with E691 filtering, a large number of events were recorded (10^8 events) which required an intensive amount of computer time to fully reconstruct the complete event set. A detailed Monte Carlo Simulation of our data and the TPS allowed us to estimate our reconstruction efficiencies. In this Chapter, I discuss the data collection, reconstruction, and simulation.

3.1 Data Collection

The data collection system consisted of three components: the trigger logic, the data acquisition subsystem, and the data monitor. The trigger logic detected each event and, if required, initiated a digitization sequence in the time-to-digital converters (TDC's) and analog-to-digital converters (ADC's). The data acquisition subsystem then read out the digitized information and recorded it on magnetic tape. The data monitor checked the correct operation of the trigger logic and data acquisition subsystem.

3.1.1 Triggers

The trigger logic component of the data collection system implemented three types of triggers: physics, calibration, and monitoring. The calibration and monitoring triggers were important in maintaining the proper functioning and calibration of the TPS and associated electronics. Detailed discussions of them can be found in [Ra87], [Me86] and references therein. The physics triggers (particularly the transverse energy trigger) had the largest impact on the results presented herein. These triggers rejected 99.9% of the unwanted pair production events while keeping 80% of the charmed events.

The TAGH trigger, selected hadronic events by requiring that an event have a hadronic energy above 40 GeV. To determine an event's hadronic energy, H, the total energies in the SLIC and Hadrometer were summed together. The actual TAGH trigger was formed from H being above 40 GeV and a coincident signal above one minimum ionizing particle from counter B (a scintillation counter located .8 cm downstream of the target).

The transverse energy trigger, E_T, more than doubled the charm content of our data relative to the TAGH events by requiring that an event have a large transverse energy. Charmed hadron decay products have larger momenta in the decaying hadron's rest frame than decay products from more prolifically producted particles such as ρ mesons and kaons. For example, pions from the decay $D^0 \rightarrow \pi^+\pi^-$ or from $\overline{K^0} \rightarrow \pi^+\pi^-$ have momenta of 922 MeVc or 206 MeVc respectively. A transformation to the lab frame does not change the mean transverse momenta since the decaying mesons are generally at small angles to

the beamline. The mean E_T for hadronic events and charm events was 1.5 GeV and 4.5 GeV respectively [Br88]. Figure 3.1 shows the E_T distributions for typical samples using the E691 TAGH trigger.

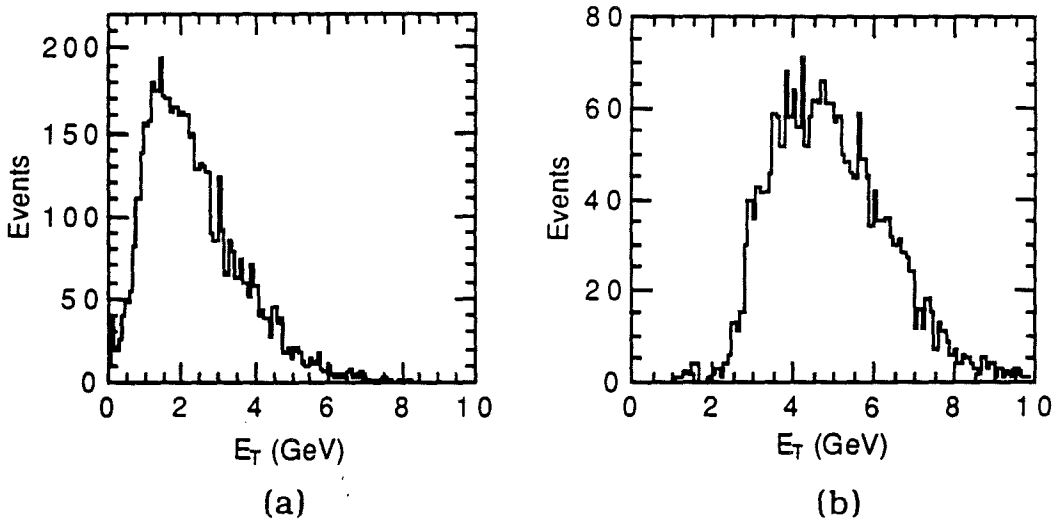

Figure 3.1 E_T distributions for (a) non-charm hadronic events, (b) charm events. (adapted from [Pu89])

We computed an estimate of an event's E_T by summing weighted values of all the channels of the SLIC and Hadrometer. The weights were given by $\sin\theta$ where θ is the average angle between the beam direction and a line from the target to the calorimeter element containing the signal. This E_T estimate was then discriminated and combined with other various trigger counter signals [Br88] to form the E_T trigger. We used a discrimination level of 2.2 GeV which reduced the hadronic background events by a factor of three while retaining 80% of the charm events [Ra87]. The majority of our data, 87%, was

taken with the E_T trigger. The remaining data was taken with the TAGH trigger†. The triggering rate using the E_T trigger was about 100 events/second for $1x10^7$ photons on target.

3.1.2 Data Acquisition and Monitoring

The data acquisition component of the data collection system digitized the spectrometer signals, read them out from CAMAC modules, and recorded them on tape. The acquisition process was initiated by one of the above mentioned triggers and controlled by a PDP-11/55. The trigger initiated the digitization sequence of the CAMAC ADC's and TDC's and the SMD scanners [Br88]. The digitized data were then transfered to a bulk memory buffer and the CAMAC modules were cleared and readied for the next event. The data were formatted and written to tape. The data acquisition subsystem recorded approximately 100 events/second with a 30% dead time.

The data monitor checked the operation of the spectrometer, trigger logic, and data acquisition subsystem. It consisted of a large software package running on a VAX 11/780. The software package incorporated an online monitoring system which allowed detached analysis processes, "DAPs", to analyze a small percentage of events fed from the PDP-11 to the VAX. Each DAP analyzed the performance of one subcomponent of the spectrometer. A DAP also monitored the beam quality and trigger rates. If any monitored quantity strayed out of predetermined tolerances, an online alarm system flashed a

† We also used a dimuon trigger for this and a separate experiment. It was not used in the thesis analyses and so is not discussed. Descriptions of it may be found in [Me86].

message to a control console. In addition to the online monitor, we walked through the experiment every eight hours to ensure that operating voltages, gas mixtures, temperatures, etc. were correct.

3.2 Data Reconstruction

To extract useful physics from the 5000 raw data tapes we acquired, the digitized spectrometer signals for each event had to be translated into a set of particle attributes. These attributes included the particle's four-momentum, trajectory, energy, and type probability. This translation was called the reconstruction.

The reconstruction was performed in two stages: Pass1 and Pass2. In Pass1 we reconstructed charged particle trajectories from the SMD and drift chamber data. Pass2 had four tasks: to estimate the incident photon energy, to reconstruct the calorimeter information for neutral particle detection, to assign probabilities for various mass hypotheses to each track using Cerenkov and calorimeter data, and to find vertex candidates. The two passes were initially run on the Fermilab Cyber 175 and 875 systems. Once the Advanced Computer Program (ACP) multiprocessor system [Na86] came on-line, Pass1 and later Pass2 were also run on the ACP.

3.2.1 Pass 1

In Pass1 we reconstructed two types of charged particle tracks: "SESTR"† tracks which traversed the SMD's and "ESTR" tracks which did not. SESTR tracks were reconstructed first using hits in the

† ESTR stands for Exhaustive Search and Tracking Routine and SESTR is silicon plus ESTR.

SMD's and DC's, followed by the reconstruction of ESTR tracks. ESTR tracks were from missed SESTR tracks and from downstream vertices due to $K^0_S \rightarrow \pi^+\pi^-$ and $\Lambda \rightarrow p\pi^-$ decays. Of all reconstructed tracks, 85% were SESTR and 15% ESTR. The average charm event contained about 10 tracks and took about 1.0 second of Cyber 175 CPU time for track reconstruction. An average E_T event required about 0.7 seconds of CPU time [Ra87].

We reconstructed SESTR tracks by first searching in the SMD's and D1 for track segments. 3-hit view tracks were formed in each of the X, Y and V SMD views. Using these all possible 9-hit (3+3+3)*, 8-hit (3+3+2) and 7-hit tracks of the form (3+3+1) were made. After each track was found, its hits were marked so that subsets of the track can be quickly rejected by subsequent analysis. Next we reconstructed the remaining 7-hit (3+2+2) and 6-hit tracks (2+2+2 and 3+2+1). These 7-hit and 6-hit track segments were required to have corroborating hits in the D1 U and V views. Of all the SESTR tracks, 46%, had 9 SMD hits, 35% had 8, 14% had 7 and 5% had 6 hits [Ha86].

The SESTR track reconstruction was continued by extending the SMD track segments beyond one or both magnets (see Figure 3.2). First the segments were linked to D3 "triplets" which consisted of a hit in each of three views in a drift chamber assembly. This linking was aided by the fact that the magnets only bent tracks in the X-Z plane. Thus only D3 triplets consistent with a straight-line extrapolation in Y of the SMD segment were considered. Any

* Each number refers to the number of hits in a view, i.e. a (3+3+1) had three hits in two views and 1 hit in the third.

additional D3 triplets are linked before moving onto D2 and D1. In the linking process we used a single bend point approximation for each magnet. After all SMD tracks were linked to DC hits, a detailed momentum fit, incorporating spatial variations of the magnetic fields, was performed for each track. Tracks with bad χ^2's or which shared too many hits with another track were discarded.

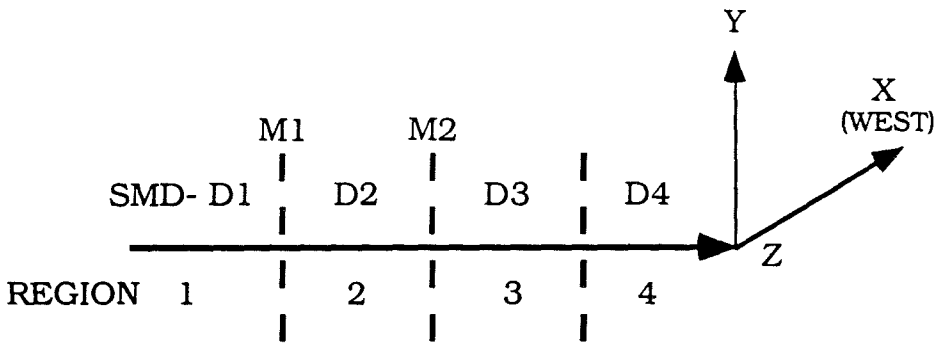

Figure 3.2 The tracking regions and coordinate systems.

ESTR track reconstruction proceeded by starting with DC hits not already used by SESTR tracks. This reconstruction found tracks from decays of K^0_S's or Λ's, or tracks missed by the SESTR reconstruction.

We categorized each track according to which reconstruction regions (see Figure 3.2) it was found. Bit 0 of the category number was assigned to region 1, bit 1 to region 2, bit 2 to region 3, and bit 3 to region 4. For example, a category 15 track passed through all four regions and a category 3 track had passed through regions 1 and 2 only.

3.2.2 Pass 2

In the Pass2 we processed information from the tagging system, the calorimeters and the Cerenkov counters. We also formed vertex candidates from the charged tracks found in Pass1. Pass2 required 0.75 CPU seconds of Cyber 175 time per event. The vertex reconstruction used half of this time; the calorimetry and Cerenkov reconstructions each took a quarter of the time.

First, we determined the energy of a beam photon. From the electron's shower position in the tagging counters we determined the electron's energy after radiating. This energy was subtracted from the initial electron beam energy, giving an estimate of the photon energy. For about 23% of recorded events the photon energy was not reconstructible from the tagging system. These events were excluded from production analyses but were used in charm decay studies.

Next, we formed a particle list by combining information from the SLIC, Hadrometer, muon wall, and Pass1. We reconstructed the SLIC information by finding showers in each of the three views: U, V, Y. A shower was an energy deposit in a contiguous group of SLIC counters, where each counter observed an energy above a minimum value. Showers with tracks pointing to them were specially marked. Using a detailed stepwise regression analysis [Su84], we distributed the observed SLIC energy amongst candidate particles. Several problems degraded the effectiveness the shower finding analysis: broad hadronic showers which can obscure narrower electromagnetic showers, satellite showers which resemble electromagnetic showers, and overlapping showers in one or more views.

For each particle found in the SLIC, we assigned a four-momentum and a probability of being an electron, muon, photon, or

neutral hadron. Electrons were identified by four criteria: 1) a consistency between the energy and momentum measurements from the SLIC and the tracking, 2) a consistency between the SLIC shower coordinates and the track coordinates at the SLIC, 3) a narrow transverse SLIC shower, and 4) a lack of signal in the Hadrometer. Muons were identified by hits in the muon wall and by narrow deposits of energy in the Hadrometer. We identified photons by either comparing their shower shapes to those generated by an EGS simulation of the SLIC or by forming them from small opening angle electron-positron pairs (the later were usually beam photons). We did not identify neutral hadrons as showers in the SLIC or Hadrometer; the position and energy resolution were not adequate.

Neutral pions were formed from pairs of photons. The π° mass was a check on the SLIC calibration constants[†]. Figure 3.3 displays mass histograms of 3 neutral particles reconstructed using SLIC information.

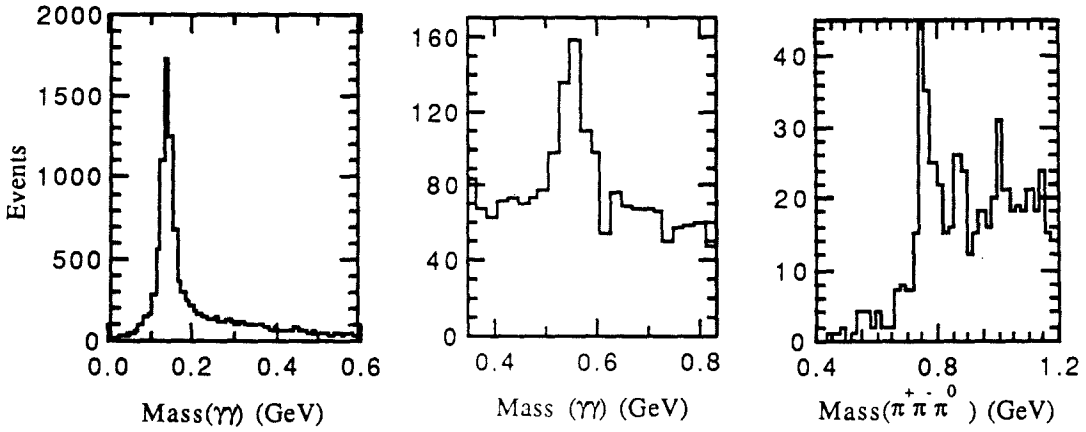

[†] a small correction to mass was necessary in high-multiplicity events.

Figure 3.3 Some particles reconstructed using the SLIC (a) $\pi^{\circ\dagger}$ (b) η° (c) ω°

For charged particles we made assignments of particle type probabilities to tracks using the Cerenkov information in conjunction with calorimetry and muon wall information. Only five types of charged particles were assumed to traverse the Cerenkov counters: electrons, muons, pions, kaons, and protons. Initially each track was assigned *a priori* probabilities for each particle type, based on the fraction of these particles found in hadronic interactions as determined from a previous photoproduction experiment, E516. These *a priori* probabilities were: 0.02 for electron, 0.01 for muon, 0.81 for pion, 0.12 for kaon, and 0.04 for proton. If a track had a high electron or muon probability, based on calorimetry and muon wall information, its electron or muon probability was set high and the remaining probabilities were set low. For the remaining tracks the amount of light collected in the Cerenkov mirrors was compared with that expected from pions, kaons, and protons. We combined these comparisons, the electron and muon probabilities, and the *a priori* probabilities, to assign probabilities CPRB2(i,j) for each event track set. CPRB2(i,j) was the probability that the ith track was of the jth particle type. We required Σ_j CPRB2(i,j) = 1 for each track.

The final Pass2 task was vertex reconstruction using SMD information. We began by finding a two track combination that formed a vertex with a good χ^2. Additional tracks were added to this vertex as long as the χ^2 remained good. Discarded tracks were used as seeds

---

† The π° plot was obtained from the tight set of cuts described in section 4.3 which includes a cut on the $\gamma\gamma$ invariant mass.

for the next vertex candidate. We stored x, y, and z positions, position errors, number of tracks, and track indices for each vertex candidate.

3.2.3 Data Summary Tapes

The creation of Data Summary Tapes, DST's, was a first step in making the complete data sample manageable. The fully reconstructed 10^8 events fit on about 5000 Pass2 6250 BPI magnetic tapes. Scanning this large tape set once for each possible analysis would have been an unnecessary expense of computer and human resources. By recording only information need for physics analysis on DST's, the data was reduced from 5000 Pass2 tapes to 500 DST's.

For specific physics analyses, subsets of data called strips were created. These strips include only events satisfying certain criteria. For example, a vertex strip was created which contained only events with secondary (decay) vertex candidates. The K^0_S strip which contained events with at least one *good* K^0_S was the strip I used for my analyses is described in section 4.1.

3.3. Monte Carlo Simulation

To estimate our reconstruction efficiencies and the integrated effects of our detector's geometrical acceptances, inefficiencies and other losses, we used a Monte Carlo simulation (MC). It was designed to generate charm events and simulate their detection in the TPS.

We produced Monte Carlo data tapes using three steps: event generation, event digitization, and event reconstruction. A set of about 30,000 events was generated for each tape. The requestor of the data usually specified that a specific charmed particle be generated in each

event and provided details about the particle, like its decay products and lifetime. The Monte Carlo generator would then produce charm in each event using the photon gluon fusion model. One or more of the charmed quarks were forced to hadronize into the requested particle while the other quarks and gluons were hadronized into other particles using the Lund model. All particles were allowed to decay using known decay rates, except for the requested particle which decayed as specified by the requestor. Truth tables containing information on each particle, such as its type, 4-momentum, charge, birth and death coordinates, etc., were written to magnetic tape. These tapes were run through a detector simulation program which produced raw data tapes with the same format as our real data tapes. The simulation contained detailed information on all components of the TPS, including measured resolutions, efficiencies, electronic noise and crosstalk levels, and geometric acceptances. The MC events were reconstructed using the standard Pass1 and Pass2 programs mentioned above. DST's were also generated for each Monte Carlo event set.

From a detailed comparison of Monte Carlo generated events and real data events (such as looking at SMD and drift chamber hit distributions, track resolutions, momentum and mass distributions), we ascertained that our MC simulated charm decaying directly to charged particles in our detector fairly well. However, we also found that the reconstruction efficiencies for K^0_S's and π^0's determined from the MC required corrections which are discussed in sections 4.2 and 4.4.

4 Efficiency Studies

Although charm decaying directly to charged particles was adequately simulated by our MC, downstream neutral particle decays such as K^0_S's and π^0's were not. Early E691 results of branching ratios of high statistics charm decays containing final state K^0_S's indicated that our MC might be underestimating our K^0_S reconstruction efficiency [Gi89]. An efficiency study which compared $N(K^{*+}\rightarrow K^0\pi^+)$ to $N(K^{*0}\rightarrow K^+\pi^-)$ for both MC and data events indicated that the MC-determined efficiency was too low by 30 ± 30%. It assumed that the production of charged and neutral K*'s was the same.

Another study [Br88a] using the decay $D^0\rightarrow K^-\pi^+\pi^0$ determined that our MC overestimated the real π^0 reconstruction efficiency. This study compared $N(D^0\rightarrow K^-\pi^+\pi^0)$ (number with π^0 reconstructed) to $N(D^0\rightarrow K^-\pi^+(\pi^0))$ (number without π^0 reconstructed) for both data and MC events. From this comparison it was determined that the MC overestimated the efficiency by (31 ± 14%).

The uncertainties from both studies are larger than most of the statistical errors of my analyses. In addition, the π^0 efficiency study did not clearly determine the momentum dependence of the overestimate. Any significant variation with momentum would effect the overestimate since the π^0 momentum spectra of the decays $D^0\rightarrow K^-\pi^+\pi^0$ and $D^0\rightarrow K^0_S\pi^0$ are different.

In this chapter, I describe the methods and results of the studies I have performed which determined the K^0_S and π^0 reconstruction efficiencies. The results of these studies are used in the analyses of Chapter 5.

4.1 Extraction of K^0_S Events

For each analysis I started with E691's K^0_S data sample. This K^0_S sample (6 million events) was stripped from our complete set of reconstructed events (100 million events). Each event was required to contain at least one *good* $K^0_S \rightarrow \pi^+\pi^-$ candidate, where a *good* $K^0_S \rightarrow \pi^+\pi^-$ candidate is defined below. The signal to background ratio for the complete sample was about 7:1.

For the strip and for subsequent analyses, only good ESTR and SESTR charged tracks of opposite charge were used to reconstruct good K^0_S candidates. For a track (ESTR or SESTR) to be considered *good* its fit χ^2/ν (ν is number of degrees of freedom) had to be less than 5.0 and its category had to be 3, 7, or 15. The χ^2/ν requirement greatly reduced the number of spurious tracks formed by random hits which happened to line up. K^0_S candidates formed from one ESTR and one SESTR track were not considered because of the low signal to background ratio inherent in this type of track pair. Thus, only K^0_S's formed from two ESTR tracks ($K^0_{S_{ESTR}}$'s) or two SESTR tracks ($K^0_{S_{SESTR}}$'s) were used.

Besides having the tracks be considered good tracks, additional kinematic and particle identification requirements of the K^0_S candidates were imposed. The Cerenkov product probability (CPROB(π,1)* CPROB(π,2)) that the candidate's tracks were pions was required to be above 0.05. This requirement eliminated most tracks which were identified as other types of charged particles such as a kaons or electrons. The z-coordinate (Z_v) of the position of the closest

approach of the candidate's two tracks was required to be greater than 1.0 cm for $K^{\circ}_{S_{SESTR}}$'s and 5.0 cm for $K^{\circ}_{S_{ESTR}}$'s. K°_{S}'s from the region upstream of 1.0 cm had a worse signal to background ratio than those from the region downstream of 1.0 cm. This was due to the larger track density near the production point. The distance of closest approach (DCA) of the two tracks was computed and required to be less than 0.01 and 0.5 cm for $K^{\circ}_{S_{SESTR}}$'s and $K^{\circ}_{S_{ESTR}}$ candidates. Finally, the invariant mass of the two pions was required to be between 0.480 and 0.514 GeV. Figure 4.1 shows a typical K°_{S} sample. For analyses involving two K°_{S}'s, a substrip was produced which included events containing at least two independent K°_{S}'s.

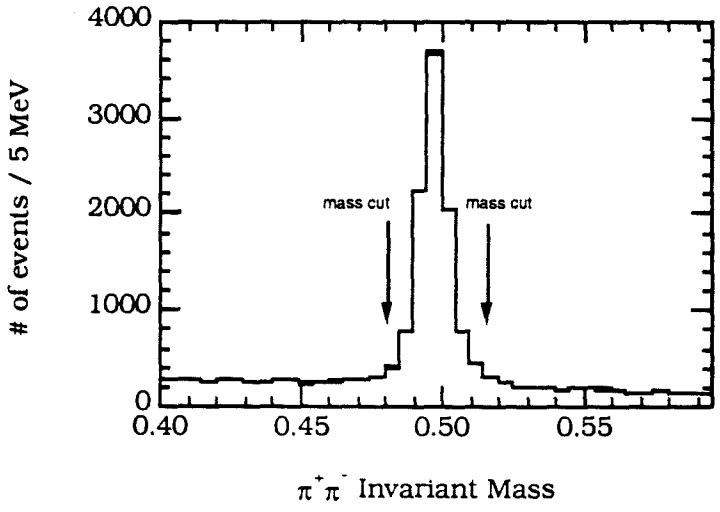

Figure 4.1 A typical K°_{S} signal

4.2 K°_{S} Reconstruction Efficiency

We determined our K^0_S reconstruction efficiency (ε_{Ks}) using our MC which was described in section 3.3. From the in-depth study which is discussed below I determined that the MC underestimates the efficiency for reconstructing K^0_S's which decay downstream of the SMD's. A correction factor for this underestimate has been applied to all the decay modes reported in chapter 5.

The approach I used was to measure the dependence of ε_{Ks} on the cut parameters used to isolate the K^0_S sample and compare this dependence in the MC and data. From this comparison I extracted ε_{Ks} for the MC relative to ε_{Ks} of the data at the nominal cut values. To check that there were no overall differences in the MC and data efficiencies, I compared tracking quantities which affect ε_{Ks}, such as per-plane efficiencies. I also made a comparison of the MC and data K^0_S mass widths as a function of momentum. Finally, I varied digitization parameters in the MC to estimate how sensitive ε_{Ks} is to these parameters. The result of this procedure is a ratio of the MC ε_{Ks} to the actual ε_{Ks} which is used as a correction to the MC determined reconstruction efficiencies.

To determine the cut dependencies of ε_{Ks}, I obtained the number of K^0_S's reconstructed for varying values of the cut parameters DCA and CPROB. I generated two sets of ten $\pi^+\pi^-$ invariant mass histograms; one set for DCA and one for CPROB. Each histogram was generated with a different cut value, varying from "no cut" to some "maximal cut". All the other cuts were held at their nominal values. I fit the mass histograms using a double Gaussian signal plus linear background. This was done for both MC and data. Figures 4.2 and 4.3 show plots of the relative efficiencies for the DCA cuts and CPROB

cuts. The DCA efficiencies were normalized to the signal found using no DCA cut and a CPROB cut of 0.05. The CPROB efficiencies were normalized to the signal found using a DCA cut of .5 cm and CPROB cut of 0.01. The behavior of the relative efficiency due to the CPROB cut is well described by the MC near the nominal CPROB cut value. This is not the case at CPROB cuts above 0.5. There is a significant deviation in the behavior of the relative efficiency of the DCA cut in the MC and data which increases with tighter cut values. At the nominal DCA cut of 0.5 cm, the MC underestimates ε_{K_S} by 1.17 ± 0.03. Also, the MC relative efficiency due to the DCA cut of .5 cm was 77.4% which accounts for all but 4% of the drop in the absolute K^0_S reconstruction efficiency noted below.

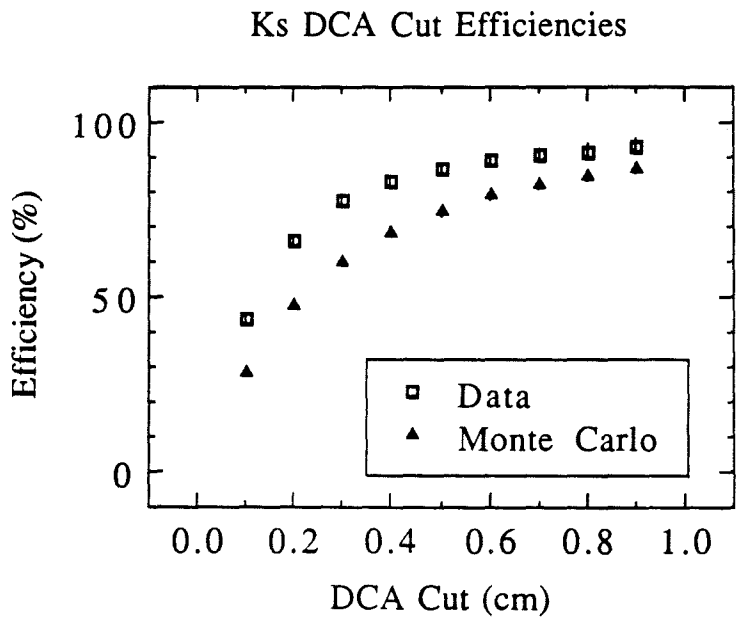

Figure 4.2 Relative efficiency of DCA Cut

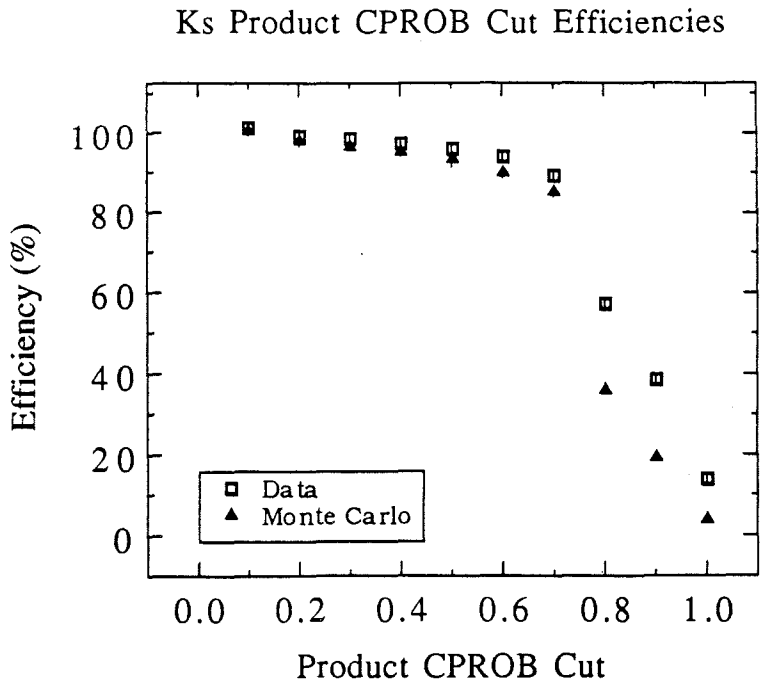

Figure 4.3 Relative efficiency of CPROB Cut

The above underestimate for ε_{Ks} does not take into consideration possible efficiency differences due to overall tracking or the $\pi^+\pi^-$ invariant mass cut. Below I describe detailed comparisons of several tracking quantities between the MC and data and comparisons of the $\pi^+\pi^-$ invariant mass widths as a function of K^0_S energy.

The first tracking quantities I examined were the per-plane efficiencies, ε_{pp}, of the SMD's and DC's. These were measured as a function of track momentum for both MC and data. I measured ε_{pp} for category 3, 7, and 15 ESTR and SESTR tracks separately. Only tracks with $\chi^2/\nu < 5.0$ and which had at least 8, 7, 10, 10 and 2 hits in the SMD's, D1, D2, D3, and D4 were considered. In addition, when computing the efficiency for a given plane, a track had to have at least

8, 7, 9, 9, 1 hits in the other planes of the SMD's, D1, D2, D3, and D4. This requirement insured a clean sample of real tracks and that the efficiency for the given plane was independent of the other planes. One drawback to this method is that a flat distribution of noise hits can bias this measurement [So91]. I estimate that this should affect ε_{pp} at the 1-2% level for average multiplicity events. The data had a slightly higher efficiency, relative to the MC, in the SMD's and D1 as can be seen in Table A.1 of Appendix A. Also, there is a decrease in efficiency for tracks with low momentum which is correctly reproduced by the MC.

In addition to a momentum measurement, the SMD ε_{pp}'s were also measured as a function of the angle, θ, each track made with each plane. The path length of a track through a given SMD strip varies as $1/\cos(\pi/2 - \theta)$ and the amount of charge extracted from the strip is proportional to the path length. Thus ε_{pp} should increase with track angle. However, the probability that the track transverses more than one strip also increases with θ. This angular dependence of ε_{pp} was studied using a test beam [Kar86] and a decrease in ε_{pp} with increasing θ was found. Using the method outlined above, I measured the angular dependence of ε_{pp}. This data is given in Table A.2 in Appendix A. Again the MC matches the data. In addition, the efficiencies were constant over the entire range of angles used. The difference between my results and those of [Ka85] was the result of decreasing noise levels in the discriminator units which allowed us to lower the thresholds.

Once the ε_{pp}'s were measured, I computed the absolute tracking efficiency of the MC for all category 15 ESTR and SESTR tracks

separately. To measure the efficiency, an attempt was made to *match* each MC generated track to reconstructed tracks event by event. A χ^2 was calculated for each generated and reconstructed track combination using the momentum and x- and y-slopes of both tracks. The combination with the minimum χ^2 was considered as the best match. I required a $\chi^2 < 6.0$ for a track to be matched. The absolute efficiency was then given by the number of matched tracks over the number of tracks generated. The tracking efficiency for the ESTR and SESTR category 15 tracks was 83.3 ± .1% and 92.3 ± .1%.

Next I measured the MC absolute tracking efficiency for tracks which came from K^0_S's and whose slower pion made an angle with the beam direction of < 30 mrad, using the method discussed above. The efficiency for reconstructing 1 track of a K^0_S was (86.1 ± .2)% and for reconstructing both tracks was (76.9 ± .8)%. In addition, the efficiency for fully reconstructing a K^0_S (DCA cut, CPROB cut, and mass cut) was (53.8 ± 1.0)%. These quantities and similar ones for $D^\circ \rightarrow K^- \pi^+$ are summarized in Table 4.1. As noted above, the drop in efficiency due to the DCA cut is 77.4% in the MC which accounts for all but 4% of the efficiency difference between reconstructing two tracks to full K^0_S reconstruction.

Type	Efficiency (%)
All tracks	83.3 ±.1
1 track, K^0_S, $\alpha < .030$	86.1 ±.2
2 tracks, K^0_S, $\alpha < .030$	76.9 ±.8
Reconstructed K^0_S, $\alpha < .030$	53.8 ±1.0

Table 4.1a Absolute MC tracking efficiency for various category 15 ESTR tracks. α is the angle between slow track and beam

Type	Efficiency (%)
All tracks	92.3 ± .1
1 track, $D^\circ \rightarrow K^-\pi^+$, $\alpha < .030$	95.7 ± .5
2 tracks, $D^\circ \rightarrow K^-\pi^+$, $\alpha < .030$	92.5± 1.2

Table 4.1b Absolute MC tracking efficiency for various category 15 SESTR tracks. α is the angle between slow track and beam

As an additional check of the MC tracking I computed the percentages of category 3-3, 3-15, and 15-15 K^0_S's as a function of K^0_S momentum (3-3 refers to K^0_S's reconstructed from two category 3 tracks, etc.). Any discrepancy between the MC and data in these percentages would indicate a problem in the detector simulation and could indicate which assembly was at fault. The percentages were calculated for $K^0_{S_{ESTR}}$ and $K^0_{S_{SESTR}}$ separately and are listed in Tables 4.2 and 4.3. I found good agreement between the MC and data percentages.

Energy	Cat 3-3	Energy	Cat 15-15	Energy	Cat 3-15	Total
4.3	74.0 ± 1.9	4.6	2.1 ± 0.3	4.5	26.4 ± 1.0	103.5 ± 2.1
4.3	73.4 ± 2.4	4.5	2.3 ± 0.5	4.4	24.3 ± 1.1	100.9 ± 2.7
7.0	21.6 ± 0.2	8.4	18.3 ± 0.5	6.9	59.2 ± 0.6	99.1 ± 0.8
6.9	21.1 ± 0.3	8.4	18.9 ± 0.3	7.8	60.6 ± 0.6	100.5 ± 0.7
11.9	4.1 ± 0.1	12.6	53.5 ± 0.3	12.2	43.4 ± 0.3	101.0 ± 0.5
11.9	4.3 ± 0.1	12.6	55.0 ± 0.5	12.1	41.0 ± 0.4	100.3 ± 0.7
17.1	1.4 ± 0.1	17.4	75.8 ± 0.5	17.2	23.1 ± 0.3	100.2 ± 0.6
17.0	1.4 ± 0.1	17.4	78.0 ± 0.7	17.1	20.8 ± 0.3	100.2 ± 0.8
22.3	0.6 ± 0.1	22.4	87.0 ± 0.7	22.2	12.4 ± 0.2	100.1 ± 0.7
22.2	0.4 ± 0.1	22.4	89.4 ± 1.0	22.2	10.1 ± 0.3	99.9 ± 1.1
0.0	0.0 ± 0.0	27.4	93.0 ± 1.0	27.2	7.0 ± 0.3	100.0 ± 1.0
0.0	0.0 ± 0.0	27.3	94.0 ± 1.4	27.1	5.5 ± 0.4	99.6 ± 1.5
0.0	0.0 ± 0.0	32.3	95.7 ± 1.3	32.3	4.3 ± 0.3	100.0 ± 1.5
0.0	0.0 ± 0.0	32.3	97.6 ± 2.0	32.2	2.4 ± 0.3	100.0 ± 2.0

Table 4.2 Percentage of category 3-3, 15-15 and 3-15 ESTR K_S^0 (MC first line, data next)

Energy	Cat 3-3	Energy	Cat 15-15	Energy	Cat 3-15	Total
4.3	82.0 ± 6.5	4.6	1.7 ± 0.4	4.5	18.9 ± 1.5	102.5 ± 6.7
4.3	80.1 ± 4.3	4.5	1.9 ± 0.4	4.4	17.6 ± 1.5	99.6 ± 4.6
7.0	27.8 ± 0.7	8.4	14.0 ± 0.4	7.9	58.4 ± 1.0	100.2 ± 1.3
6.9	31.0 ± 0.8	8.4	12.2 ± 0.5	7.8	57.5 ± 1.2	100.7 ± 1.5
11.9	0.8 ± 0.3	12.6	44.4 ± 1.4	12.2	50.4 ± 1.2	100.7 ± 1.9
11.9	1.0 ± 0.4	12.6	41.6 ± 1.1	12.1	52.4 ± 1.4	100.0 ± 1.8
17.1	0.8 ± 0.4	17.4	64.6 ± 1.6	17.2	29.9 ± 1.2	95.9 ± 2.0
17.0	0.5 ± 0.3	17.4	64.5 ± 2.0	17.1	32.2 ± 1.5	100.2 ± 2.5
22.3	0.0 ± 0.2	22.4	80.6 ± 2.4	22.2	25.3 ± 2.0	106.8 ± 3.2
22.2	0.0 ± 0.0	22.4	78.4 ± 3.2	22.2	17.5 ± 1.3	96.0 ± 3.4
0.0	.0 ± 0.0	27.4	85.6 ± 3.3	27.2	14.2 ± 1.1	99.7 ± 3.5
0.0	.0 ± 0.0	27.3	88.5 ± 4.7	27.1	10.8 ± 1.2	99.3 ± 4.9
0.0	.0 ± 0.0	32.3	90.3 ± 7.5	32.2	10.9 ± 1.5	101.2 ± 7.7
0.0	.0 ± 0.0	32.3	87.0 ± 6.1	32.2	10.7 ± 6.3	97.7 ± 8.8

Table 4.3 Percentage of category 3-3, 15-15 and 3-15 SESTR K_S^0 (MC first line, data next)

The next quantity I compared between the MC and data was the $\pi^+ \pi^-$ invariant mass width as a function of K^0_S energy. This comparison illustrates the effect of the mass cut on the difference between ε_{Ks} for the MC and data. To make this comparison I fit the mass plots to a double Gaussian signal[†] , plus a linear background. Listed in Table 4.4 are the individual widths of the Gaussians, their integrated content, and the efficiency associated with each when the *standard* mass cut (0.480 to 0.514 GeV) is employed. The Gaussian with the largest content is listed in the first column set. The *standard* mass cut gives an efficiency of (99.6 ± 0.2)% for the data and (99.3 ± 0.3)% for the MC. The Gaussian with the smaller content has a much larger width. The efficiency of the mass cut on this part of the signal is (95.7 ± 0.5)% for the data and (89.9 ± 0.7)% for the MC. Summing over all K^0_S energies and over both Gaussians leads to an efficiency for the mass cut of (97.3 ± 0.5)% for the data and (94.0 ± 0.8)% for the MC. This shows that the MC ε_{Ks} is (3.3 ± 0.9)% lower than the data. This effect is momentum dependent and small compared to other errors in a typical branching ratio analysis. We will therefore include it in the overall error on the correction factor for ε_{Ks}.

[†] Two Gaussians were used because they a good fit to the extra-long tails of the K^0_S reconstructed mass distributions.

Energy	Width 1 (content)	Efficiency	Width 2 (content)	Efficiency
4.5	5.70 ± .16 (4860±244)	99.7 ± .1	2.16 ± .21 (1525±224)	100.0 ± .0
	7.10 ± .53 (1972 ± 349)	98.3 ± .9	3.46 ± .32 (1775 ± 360)	100.0 ± .0
8.0	5.95 ± .05 (54031± 1233)	99.6 ± .0	2.76 ± .09 (20348 ± 1222)	100.0 ± .0
	3.91 ± .05 (26339 ± 937)	100.0 ± 0.	8.25 ± .27 (12620 ± 892)	96.1 ± .7
12.5	3.54 ± .04 (55869 ± 1352)	100.0 ± .0	7.26 ± .13 (32126 ± 1210)	98.1 ± .2
	3.76 ± .04 (30399 ± 590)	100.0 ± .0	9.04 ± .22 (12385 ± 546)	94.0 ± .7
17.4	3.76 ± .04 (47878 ± 849)	100.0 ± .0	8.83 ± .24 (16756 ± 786)	94.5 ± .6
	3.86 ± .04 (22260 ± 362)	100.0 ± .0	10.05 ± .26 (8692 ± 323)	90.0 ± .8
22.4	3.80 ± .05 (30739 ± 673)	100.0 ± .0	9.07 ± .28 (12176 ± 623)	93.8 ± .7
	3.81 ± .05 (14009 ± 267)	100.0 ± .0	11.03 ± .30 (6361 ± 237)	87.6 ± 1.0
27.4	4.07 ± .05 (20432 ± 403)	100.0 ± .0	11.16 ± .42 (7533 ± 357)	87.1 ± 1.3
	4.14 ± .07 (9081 ± 187)	100.0 ± .0	13.39 ± .48 (4038 ± 161)	79.6 ± 1.5
32.3	4.35 ± .07 (13857 ± 307)	100.0 ± .0	12.50 ± .66 (4484 ± 265)	82.6 ± 2.3
	4.16 ± .10 (5171 ± 178)	100.0 ± .0	13.41 ± .57 (2988 ± 140)	79.6 ± 1.8
37.4	4.25 ± .11 (7853 ± 347)	100.0 ± .0	10.69 ± .51 (4442 ± 319)	88.8 ± 1.7
	4.70 ± .13 (3941 ± 133)	100.0 ± .0	14.79 ± 1.01 (1719 ± 114)	75.0 ± 3.0
42.3	4.59 ± .13 (5470 ± 229)	100.0 ± .0	12.59 ± .77 (2787 ± 206)	82.3 ± 2.7
	4.38 ± .22 (1767 ± 112)	100.0 ± .0	13.23 ± .85 (1485 ± 111)	79.9 ± 2.5
47.4	4.67 ± .19 (3502 ± 220)	100.0 ± .0	12.39 ± .86 (2218 ± 199)	82.9 ± 3.0
	4.69 ± .25 (1263 ± 81)	100.0 ± .1	16.74 ± 1.50 (1025 ± 79)	69.2 ± 4.4
52.3	5.30 ± .18 (2829 ± 129)	99.9 ± .0	18.56 ± 2.70 (1384 ± 161)	64.2 ± 6.6
	5.22 ± .49 (850 ± 105)	99.9 ± .2	14.74 ± 2.05 (598 ± 91)	75.0 ± 6.2
57.2	9.14 ± .50 (1884 ± 164)	93.7 ± 1.5	3.59 ± .46 (749 ± 168)	100.0 ± .0
	7.64 ± .35 (747 ± 38)	97.4 ± .7	1.13 ± .35 (72 ± 25)	100.0 ± .0

Table 4.4 K°_{S} Gaussian widths for data (first row) and MC (second row)

To determine why the MC does not adequately describe the DCA parameter for real $K^{\circ}_{S_{ESTR}}$'s and does not model the ε_{pp}'s in D1 better, I varied two sets of parameters in the MC digitization process. First, I varied the resolution used to *smear* hit locations in D1. Table 4.5 displays the relative efficiency (with the *standard* DCA cut) as a

function of D1 resolution. ε_{Ks} is not sensitive to reasonable changes in this digitization parameter. Next I varied the D1 hit probability in the digitization routines. The MC D1 ε_{pp}'s are lower than the data's. Unfortunately I was not able to increase the D1 hit probability parameter significantly because it was already set to nearly 1.0. I did lower them and the resultant measured ε_{pp}'s and tracking efficiencies are listed in Table 4.6. The tracking efficiency was only slightly sensitive to reasonable changes of these parameters.

D1 Resolution (cm)	Relative Efficiency
.0075	75.1 ± 2.2
.0150	73.9 ± 2.0
.0300	74.4 ± 1.4
.0600	72.0 ± 2.7
.3000	63.5 ± 4.0

Table 4.5 Relative ε_{Ks} vs D1 resolution in MC

D1 Efficiency	D1 Efficiency (Measured)	2 K°_{S}- Tracks
97.0	88.7 ± .3	71.7 ± 3.3
98.0	89.6 ± .3	67.2 ± 3.5
99.0	90.1 ± .3	70.6 ± 3.4
100.0	90.8 ± .3	75.1 ± 3.2

Table 4.6 D1 average per-plane efficiency vs Efficiency parameter in MC digitization

From the full K°_{S} study, I have found that the MC determined ε_{Ks} underestimates the real ε_{Ks} by 17±10%. A correction factor given by $C(K^{\circ}_{S}) = \varepsilon_{Ks}(data)/\varepsilon_{Ks}(MC) = 1.17 \pm 0.10$ can be used to correct MC determined reconstruction efficiencies. The error on the correction

factor is from the statistical errors on the DCA, CPROB, and mass cut factors, and uncertainties in the tracking efficiency. To correct a MC determined efficiency, one should multiply the efficiency by $(1.17\pm0.10)^n$, where n is the number of K^0_S's in the final state.

4.3 π° Selection

We reconstructed π°'s by identifying the decay $\pi^\circ \rightarrow \gamma\gamma$. To select *good* π°'s, we made cuts on the π° quality factor IQUAL, which was computed from several photon reconstruction parameters. First, for each event we compiled a list of photon candidates from SLIC showers which were consistent with expected photon shower shapes. For each candidate a probability, TESTB, was assigned which reflected how well the candidate's shower fit the expected shower shape. We assigned another parameter to each candidate, TESTC, which is a measure of the probability that the candidate is not associated with any π°. We determined TESTC partially from how well the candidate, when paired with any other candidate, gave a π° invariant mass. We then paired together the photon candidates to form π° candidates. To improve the π° momentum ($\mathbf{P}_{\pi^\circ}$) resolution, we adjusted each component of $\mathbf{P}_{\pi^\circ}$ by an amount proportional to $\Delta M^2_{\pi^\circ}$ and $\sigma_{E\gamma}$. $\sigma_{E\gamma}$ is the error in the measurement of each photon's energy, E_γ, and $\Delta M^2_{\pi^\circ}$ is given by:

$$\Delta M^2_{\pi^\circ} = M^2_{\gamma\gamma} - M^2_{\pi^\circ}. \qquad (4.1)$$

We also required that each photon in a candidate π° satisfy the following criteria: have E_γ above 2.0 GeV, have transverse

momentum above 40 MeV, and must be at least 6 cm (vertically) from the center of the SLIC (to avoid the congested pair-plane region). We set the first 2 bits of IQUAL if both π° photons satisfied these criteria. We set the third bit if the product of the photons' TESTB's were above 0.2 and the fourth bit if the TESTC product was below 0.5. Only π°'s with IQUAL=15 were used in my analyses. Figure 4.4 displays a mass spectrum of IQUAL = 15 π°'s.

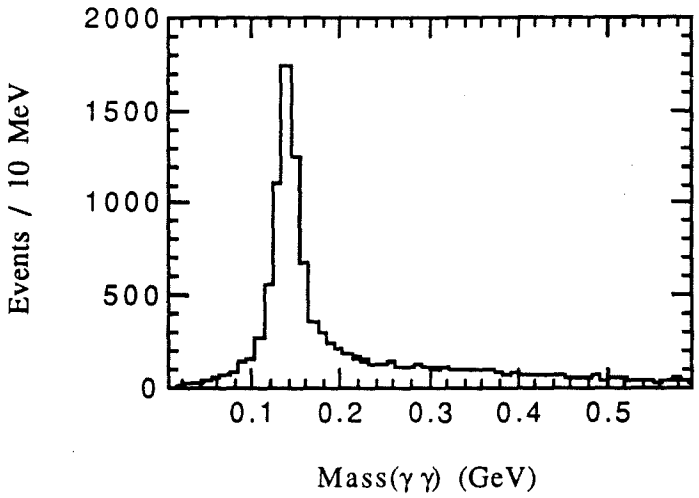

Figure 4.4 A typical π° signal after applying π° cuts

4.4 π° Reconstruction Efficiency

I have completed a π° reconstruction efficiency ($\varepsilon(\pi^\circ)$) study which yields a more accurate result for the MC efficiency overestimate than the $D^\circ \rightarrow K^-\pi^+\pi^\circ$ study [Br88], gives the momentum dependence of the efficiency, and provides a possible explanation for the overestimate. This improved understanding of the MC determined

$\varepsilon(\pi^\circ)$ was possible by using the four Kπ decay modes of K*'s which had about ten times more events than the $D^\circ \to K^-\pi^+\pi^\circ$ study.

My study's main goal was to determine if the MC correctly reproduces the momentum dependence and overall scale of $\varepsilon(\pi^\circ)_{data}$. This was accomplished by relating $\varepsilon(\pi^\circ)$ to $\varepsilon(\pi^+)$ which is well understood. Specifically, I computed

$$R_{data} = \frac{\varepsilon(\pi^\circ)_{data}}{\varepsilon(\pi^+)_{data}}, \quad R_{MC} = \frac{\varepsilon(\pi^\circ)_{MC}}{\varepsilon(\pi^+)_{MC}}, \qquad C(\pi^\circ) = \frac{R_{data}}{R_{MC}} = \frac{\varepsilon(\pi^\circ)_{data}}{\varepsilon(\pi^\circ)_{MC}}, \tag{4.2}$$

each as a function of P_{π°. If $\varepsilon(\pi^\circ)_{MC}$ is correct, $C(\pi^\circ)$ should be 1.0. If not, $C(\pi^\circ)$ can be used to correct any reconstruction efficiency involving π°'s.

To compute R_{data} and R_{MC}, I used a relation involving all four Kπ decay modes of charged and neutral K*'s. From isospin symmetry, one can obtain the relation [Su84]

$$\frac{N(K^{*\circ}\to K^\circ_S\pi^\circ)}{N(K^{*\circ}\to K^+\pi^-)}\,\frac{N(K^{*+}\to K^+\pi^\circ)}{N(K^{*+}\to K^\circ_S\pi^+)} = \frac{1}{\sqrt{2}}. \tag{4.3}$$

Rearrangement of this relation leads to

$$R=\frac{\varepsilon(\pi^\circ)}{\varepsilon(\pi^+)}=2*\left[\frac{N(K^{*\circ}\to K^\circ_S\pi^\circ)}{N(K^{*\circ}\to K^+\pi^-)}\,\frac{N(K^{*+}\to K^+\pi^\circ)}{N(K^{*+}\to K^\circ_S\pi^+)}\right]^{\frac{1}{2}}. \tag{4.4}$$

In this expression the K^0_S and K^+ efficiencies cancel as do the K* production factors. The efficiency of the DCA (distance of closest approach of the two SESTR tracks) cut used in the reconstruction of $K^{*\circ} \rightarrow K^+\pi^-$ does not cancel in R. However, when I compare R_{data} to R_{MC} , the DCA efficiency will cancel assuming that the MC models this efficiency correctly.

The first step toward calculating R_{data} and R_{MC} was to generate $K\pi$ invariant mass histograms for each of the four K* decay channels. This was done for the five P_π regions: $P_\pi < 10$, $10 < P_\pi < 20$, $20 < P_\pi < 30$, $30 < P_\pi < 40$, $P_\pi > 40$ GeV, and also integrated over all P_π. I used MC data with appropriate K* decays (coming from charm decays) and unstripped data DST's (about 20% of the complete data sample).

The background shapes under the K* signals in the $K\pi$ histograms I obtained were difficult to estimate. In several of the histograms, the K* signal peaked at the peak of the background. So I generated $K\pi$ pseudo-backgrounds to determine the background shapes under the K* signals. These pseudo-backgrounds were generated by computing the invariant mass of $K\pi$ combinations taken from independent events. For each $K\pi$ pair, their parent events were required to have equal photon multiplicities and equal charged track multiplicities. Their total energies (observed in the calorimeters) were required to be within 20% of one another. The pseudo-backgrounds reproduced the complete shapes of the real backgrounds but without the K* peaks. They were fit to the function

$$g(m) = A(m - B)^C e^{-E(m - D)} \qquad (4.5)$$

and their shapes were then scaled to the background levels observed in the real data. The fits to most of the pseudo-backgrounds had acceptable χ^2 per degree of freedom of 1.0-1.5 over the entire $K\pi$ mass region. For those fits which were not acceptable over the entire region, I limited the fitted region to insure a good fit in the K* signal region.

Once the background shapes were determined and scaled, I used two methods to estimate the K* signal in each histogram: "signal fit" and "background subtraction". In the signal fit method, I fit the signal with a student t-distribution whose shape parameters were fixed by the MC. Using a simple Monte Carlo, I found that this distribution gave a good fit to a convolution of a Breit-Wigner and a Gaussian. In the background subtraction method I did a bin-by-bin background subtraction, then summed up events in the signal region. Figure 4.5 shows the typical quality of the fits obtained. Results from both fit methods are given in Table 4.7.

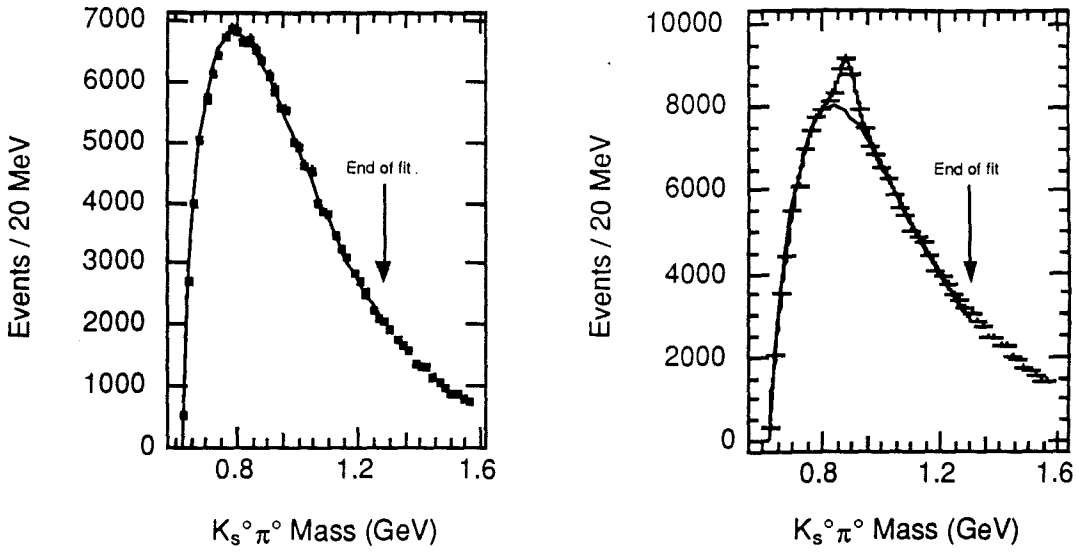

Figure 4.5 Typical quality of K* fits. (a) Fit to pseudo-background, (b) Fit to "background" plus signal

I used the numbers of K*'s from each sample, listed in Table 4.7, to compute R_{data} and R_{MC}. R_{MC} was scaled for each P_π region to account for the actual number of K*'s generated, using

$$R_{MC} = \frac{R_{raw}^{MC}}{R_G}, \quad R_G = 2^* \left[\frac{N(K^{*\circ} \to K^0_S \pi^\circ)}{N(K^{*\circ} \to K^+ \pi^-)} \frac{N(K^{*+} \to K^+ \pi^\circ)}{N(K^{*+} \to K^0_S \pi^+)} \right]^{\frac{1}{2}}. \qquad (4.6)$$

where N( ) refers to the number of K*'s generated. R_{data} and R_{MC} are plotted in Figure 4.6.

The correction factor $C(\pi^\circ)$, computed using equation (4.2), is plotted in Figure 4.7. $C(\pi^\circ)$ is equivalent to the correction factor obtained from the $D^\circ \to K^-\pi^+\pi^\circ$ study [Br88]. $C(\pi^\circ) > 1.0$ means the MC underestimates the π° reconstruction efficiency (lowering branching

ratios) while $C(\pi^\circ) < 1.0$ means the MC overestimates the efficiency (raising branching ratios). To use this factor one should use the formula

$$\varepsilon_{true} = C(\pi^\circ) * \varepsilon_{MC}. \qquad (4.7)$$

$C(\pi^\circ)$ is consistent with being constant over the entire P_{π° region considered, as can be seen in Figure 4.7 and Table 4.8. $C(\pi^\circ)$'s value when integrated over all momenta is 0.62 ± 0.07 which is consistent with the $D^\circ \rightarrow K^-\pi^+\pi^\circ$ study's result of $0.69 \pm .14$.

$P\pi$ region (GeV)	$K^{*\circ}\to K^{\circ}_{S}\pi^{\circ}$	$K^{*\circ}\to K^{+}\pi^{-}$	$K^{*+}\to K^{+}\pi^{\circ}$	$K^{*+}\to K^{\circ}_{S}\pi^{+}$
		(Data, signal fit)		
All P_π	5110±230	352050±5330	24180±720	115430±4100
P_π < 10 GeV	1280±140	156450±10100	4020±830	55310±1170
10 < P_π < 20 GeV	2370±180	127880±7080	17910±1300	34730±1130
20 < P_π < 30 GeV	680±80	30300±4030	4520±363	11512±230
30 < P_π < 40 GeV	160±40	9747±260	910±100	3690±120
P_π > 40 GeV	100±30	5840±220	563±70	2280±560
		(Data background subtracted)		
All P_π	4380±230	308730±5370	20420±730	109930±4110
P_π < 10 GeV	1170±150	139800±10120	4220±850	53900±1230
10 < P_π < 20 GeV	2050±180	107020±7080	15730±1290	31120±1140
20 < P_π < 30 GeV	620±80	24800±4030	4280±370	10410±230
30 < P_π < 40 GeV	190±40	7980±290	860±100	3470±130
P_π > 40 GeV	80±30	4720±220	510±70	2350±560
		(Monte Carlo, signal fit)		
All P_π	1100±70	15990±260	3330±130	5910±200
P_π < 10 GeV	180±70	7420±202	510±60	3150±200
10 < P_π < 20 GeV	520±40	5450±140	1720±90	1870±100
20 < P_π < 30 GeV	228±23	1710±70	610±50	580±50
30 < P_π < 40 GeV	80±14	740±37	250±20	230±20
P_π > 40 GeV	37±15	650±30	133±20	80±10
		(Monte Carlo background subtracted)		
All P_π	920±40	13360±190	2920±90	5640±160
P_π < 10 GeV	160±30	5750±150	500±50	3090±140
10 < P_π < 20 GeV	440±30	4680±100	1460±60	1700±70
20 < P_π < 30 GeV	210±20	1600±50	590±30	550±34
30 < P_π < 40 GeV	80±10	730±30	240±20	220±20
P_π > 40 GeV	30±10	620±30	115±10	80±10

Table 4.7 Results of $K\pi$ histogram fits (Monte Carlo results are uncorrected for actual number generated)

Momentum Region (GeV)	Mean Momentum (GeV)	C_{BG}	C_F
All P_{π°	14.6	0.62 ± 0.07	0.63 ± 0.07
$P_{\pi^\circ} < 10$	7.1	0.88 ± 0.32	0.91 ± 0.60
$10 < P_{\pi^\circ} < 20$	14.2	0.72 ± 0.10	0.69 ± 0.12
$20 < P_{\pi^\circ} < 30$	24.0	0.56 ± 0.15	0.53 ± 0.14
$30 < P_{\pi^\circ} < 40$	34.0	0.49 ± 0.15	0.39 ± 0.14
$P_{\pi^\circ} > 40$	45.4	0.82 ± 0.39	0.74 ± 0.51

Table 4.8 Correction factors showing that the Monte Carlo overestimates the π° reconstruction efficiency. C_{BG} is from background subtracted signals, C_F is from fitted signals

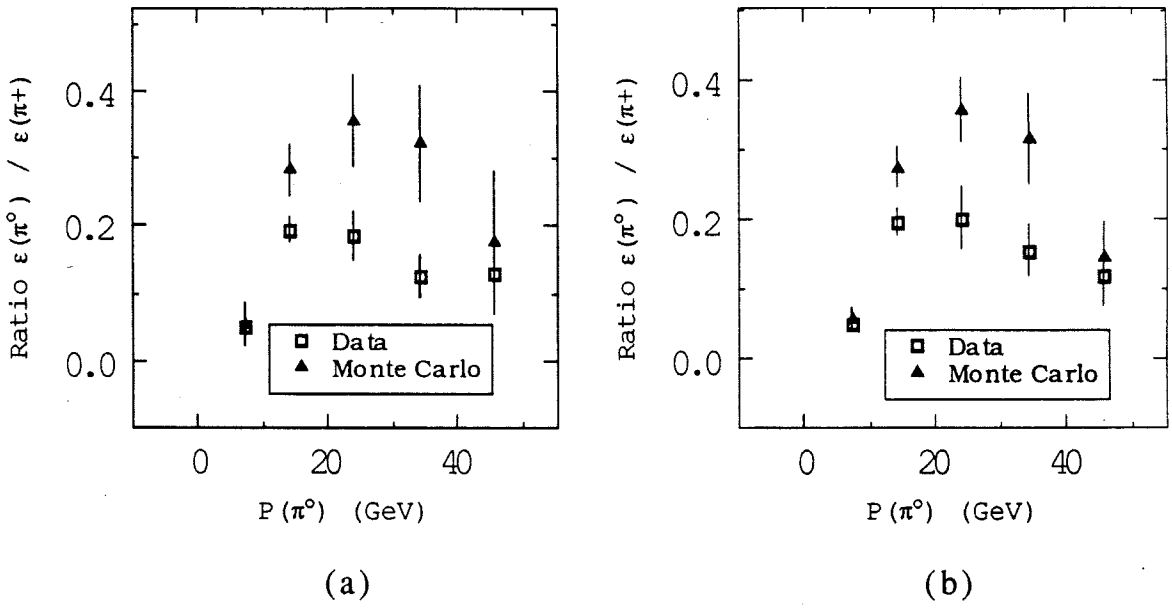

Figure 4.6 (a) Ratio using signal fitted results, (b) Ratio using background subtracted results

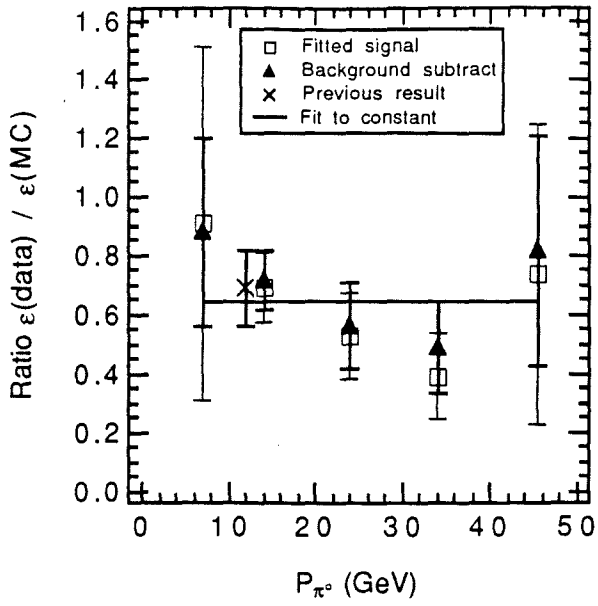

Figure 4.7 Correction factor showing that the Monte Carlo overestimates the π° reconstruction efficiency. (Solid line is a fit of the background subtracted data to a constant giving a $\chi^2/\nu = 0.86$)

To determine where the MC was overestimating $\varepsilon(\pi^\circ)$, I looked at $\varepsilon(\pi^\circ)$ as a function of the six cuts which are used to isolate a π° sample. For each cut parameter, I generated $\gamma\gamma$ invariant mass histograms, each with a different cut value from "no cut" to some maximal cut. All the other cuts were held at their nominal values. There were a total of six sets of histograms, one for each cut parameter; each set contained ten histograms. For each histogram set, I tabulated the number of π°'s in each histogram, then normalized these numbers to the number of π°'s in the histogram with "no cut". The result is of this process is the value of $\varepsilon(\pi^\circ)$ for each cut value

relative to $\varepsilon(\pi^0)$ with no cut, for each cut parameter. These values are plotted in Figure 4.8. I did this using unstripped data DST and using MC data.

To compare the MC and data relative $\varepsilon(\pi^0)$'s, I plotted the ratio $\varepsilon(\pi^0)_{data}$ / $\varepsilon(\pi^0)_{mc}$ as a function of each cut in Figure 4.9. The MC correctly reproduces the cut dependences ±5% for all but one of the cut parameters at the nominal cut values. The largest difference between the MC and data is in the TESTB parameter. TESTB is a measure of the probability that a given SLIC shower was produced by a photon. This information is useful but of limited value since recombining the dependencies into one result is not straightforward due to their strong correlations.

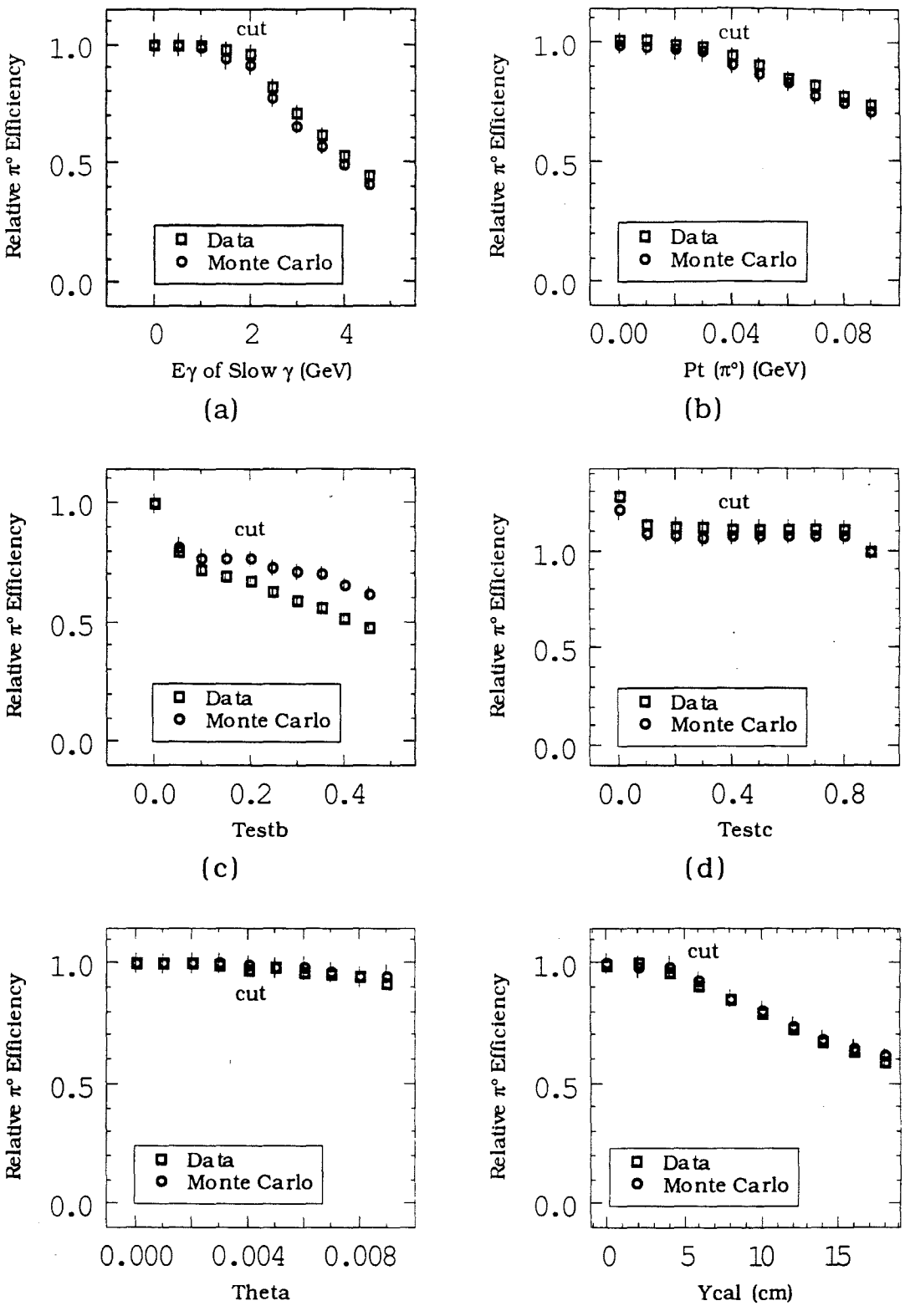

Figure 4.8 Relative π° Efficiency for Data and Monte Carlo

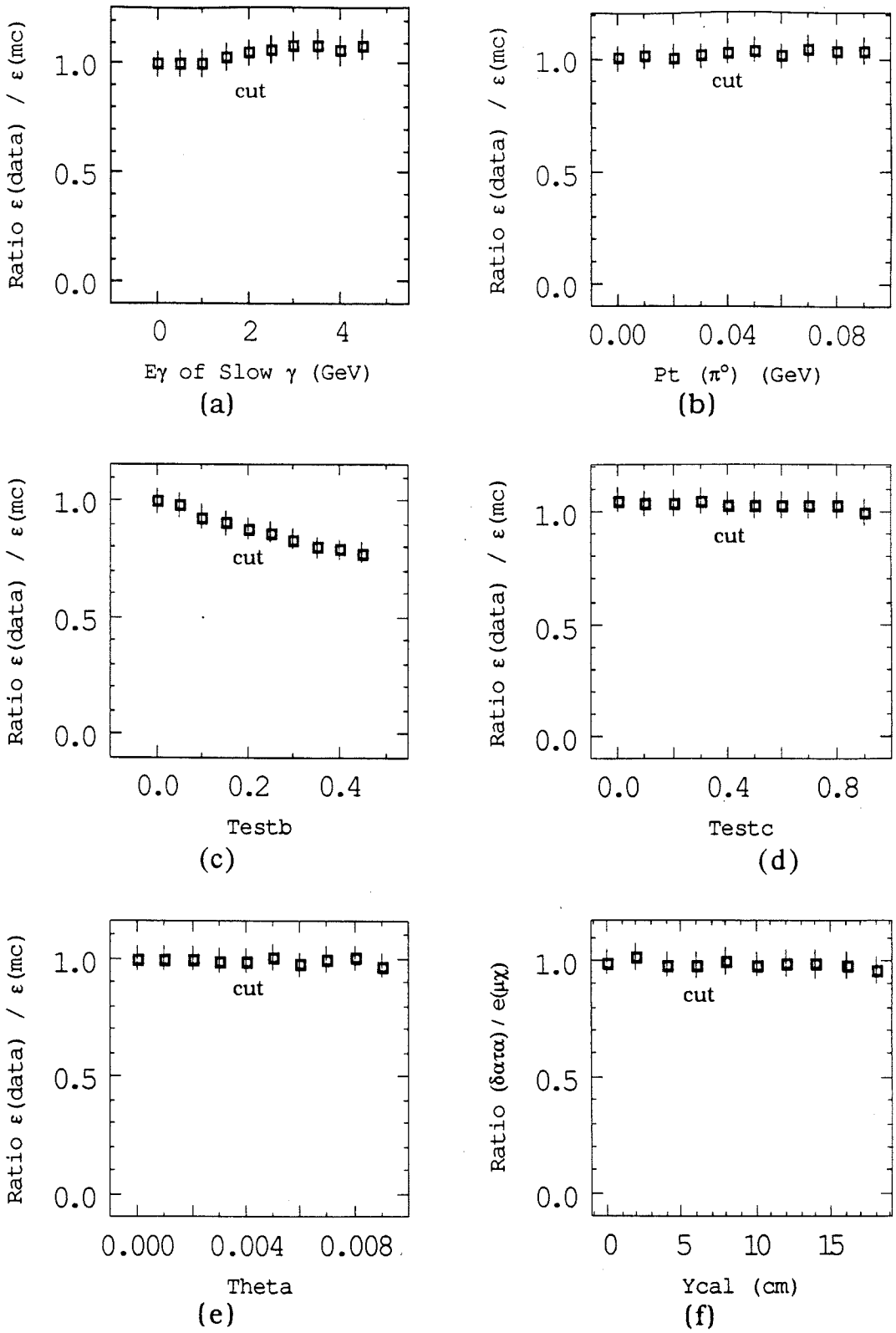

Figure 4.9 Ratio of ε(data)/ε(MC) for π°'s vs cuts

5 Analysis of Decay Modes

In this chapter, I will describe the methods and results of the decay analyses: $D^\circ \to \overline{K}^\circ \pi^\circ$, $D^\circ \to \overline{K}^\circ K^\circ$, $D^\circ \to \overline{K}^\circ \overline{K}^\circ K^\circ$, $D^+ \to \overline{K}^\circ \pi^+$, $D^+ \to \overline{K}^\circ K^{*+}$, $D_s^+ \to \overline{K}^\circ K^{*+}$. Some analysis techniques are common to several of these decay modes and are described first.

5.1 Analysis Methods

Three major analysis techniques were used in the analysis for this thesis: D* hypothesis, multiple charged track vertexing, single charged track vertexing (single prong analysis). These three techniques will be discussed in this section and refered to in other sections in this chapter.

5.1.1 D* hypothesis

The D* hypothesis technique was used in all D° analyses as the main method of background reduction, especially those with fully neutral final states. Its premise is to look for D°'s from the decay chain $D^{*+} \to D^\circ \pi^+$, $D^\circ \to$anything. All SESTR π^+ (bachelor π^+) tracks in an event were combined with the D° decay products to form the invariant masses, M_{D^*}. The mass differences $\Delta M = M_{D^*} - M_{D^\circ}$ were required to lie between 0.144 and 0.147 GeV. This tight mass difference cut (relative to the separate M_{D^*} and M_{D° resolutions) is possible because the mass resolution from the D° decay products cancels in ΔM. This ΔM requirement reduced combinatorial backgrounds by a factor of 50

while losing only 25% of the D*'s. However, 80% of the D°'s were not picked up because they did not come from D* decays.

5.1.2 Vertex separation technique

To reduce combinatorial backgrounds for final states with at least two charged tracks, we also used a vertex separation technique whose feasibility is based on D meson lifetimes and the resolution of our SMD's. A D° meson with 60 GeV momentum will typically travel 0.4 cm before it decays. The main idea of the technique is to reconstruct the decay vertex position of the D and the production (or primary) vertex position as illustrated in Fig. 5.1. It requires at least two SESTR tracks from the D decay products. ESTR tracks cannot be used as their position resolution is about 20 times larger. The resolution in longitudinal vertex separation distance between production and decay vertices was typically 300 mm for a D with 60 GeV/c momentum.

We required that the tracks from these decay products gave an acceptable fit to a common vertex with a good χ^2 (χ_d^2) per degree of freedom. All other reconstructed vertices in the event were considered as production vertex candidates. For each candidate we removed any decay product tracks from the vertex and required the fit to the remaining tracks have a good χ^2 (χ_p^2) per degree of freedom. The D meson momentum vector (P_D) was computed and projected back into the x-y plane containing the primary vertex candidate. The transverse miss distance, called DIP, (see Fig. 5.1) was computed and the primary vertex with the smallest DIP was selected. We also calculated the longitudinal vertex separation between the production

and decay vertices, Δz, and its error σ_z. Since Δz is approximately proportional to the D meson's boost factor (γ_D) and σ_z is proportional to $1/\gamma_D$, we formed the ratio SDZ = $\Delta z/\sigma_z$ which is roughly independent of P_D. We used SDZ as a cut parameter instead of Δz. We also required that no extraneous tracks pass within a small distance (typically 80 μm) of the decay vertex (called the isolation cut, see Fig. 5.2) and that all decay product tracks pass closer to the decay vertex than to the production vertex (called the RAT cut).

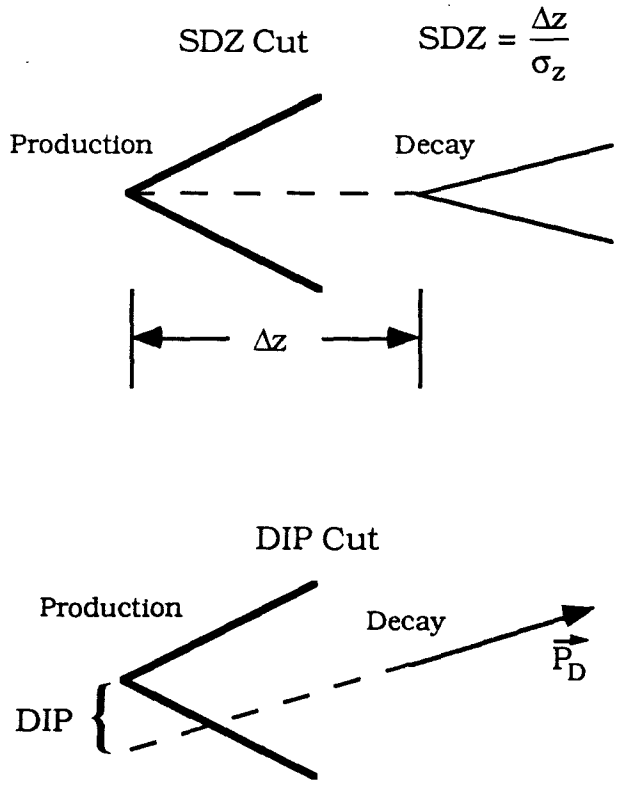

Figure 5.1 The SDZ and DIP Cuts

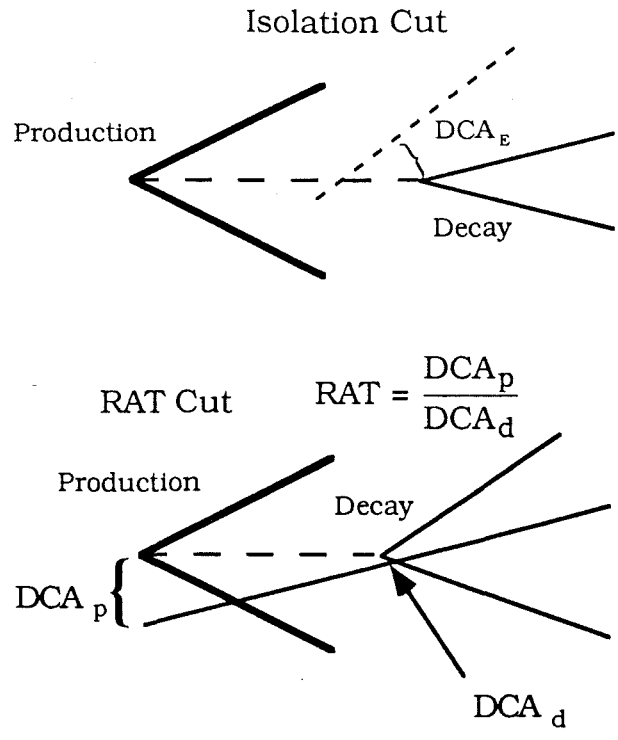

Figure 5.2 The isolation and RAT cuts

5.1.3 Single prong technique

We have adapted our vertex separation technique, as just described, for decays with only one track traversing the SMD's, as in $D^+ \rightarrow \overline{K}^\circ \pi^+$. With only one SMD track we cannot fully reconstruction the decay vertex. We can, however, compute an estimate of the decay position using the good position resolution of the SMD track and the direction of the D^+. After selecting the best production vertex and estimating the decay vertex (both described below), we can compute vertexing parameters similar to the multiple charged track method. Making cuts on these parameters, we can enhance our sensitivity to modes with single charged tracks.

In the multiple charged track method, we projected $\mathbf{P_D}$ back to each production vertex candidate and selected the the candidate

which minimized DIP. With a single SMD track our resolution on DIP was too poor to select effectively a production vertex. Instead we computed the decay plane of the D using the position information of the SMD track and the direction of the D (from $\mathbf{P_D}$). The decay plane contains the production vertex. We used the distance the candidate production vertex was from the decay plane (D_{miss}) to select the best one. Specifically, we decomposed D_{miss} into components in the decay plane (ITP) and perpendicular to the decay plane (OTP), as illustrated in Fig. 5.3. This figure is drawn with $\mathbf{P_D}$ coming out of the page. OTP corresponds to DIP and should be small (MC average was 40 μm) and ITP corresponds to Δz and should be large. ITP is dependent on $\mathbf{P_D}$ and decreases as the SMD track becomes collinear with $\mathbf{P_D}$. To decrease this effect we used ITP' as defined in Fig. 5.4 instead of ITP (its MC average was 300 μm). The production vertex candidate which minimized OTP while still giving a reasonable value of ITP' was selected as the best one.

Once we chose a production vertex candidate, we *pinned* $\mathbf{P_D}$ to this vertex position and calculated the distance of closest approach (DCA') of this vector and the SMD track. We then used the midpoint of DCA' as the estimated decay vertex position. Using this vertex position, we were able to calculate a Δz and SDZ as defined above. We also computed the distance of closest approach (DCAISO) of the SMD track to any other reconstructed vertex (excluding the production vertex). Making a cut on this parameter allowed us to reduce backgrounds from multiple charged track charm decays.

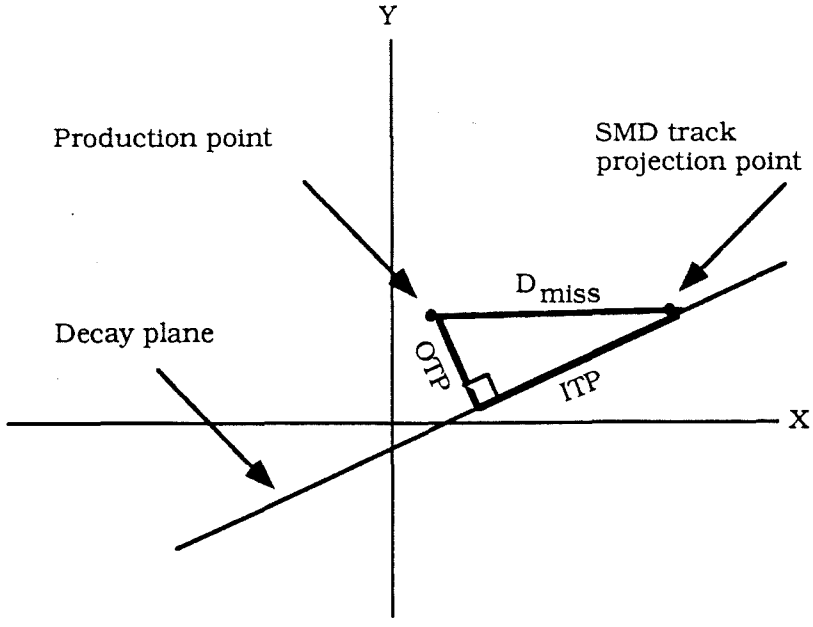

Figure 5.3 Definition of OTP an ITP single prong parameters (note: $\mathbf{P_D}$ is directed out of the page)

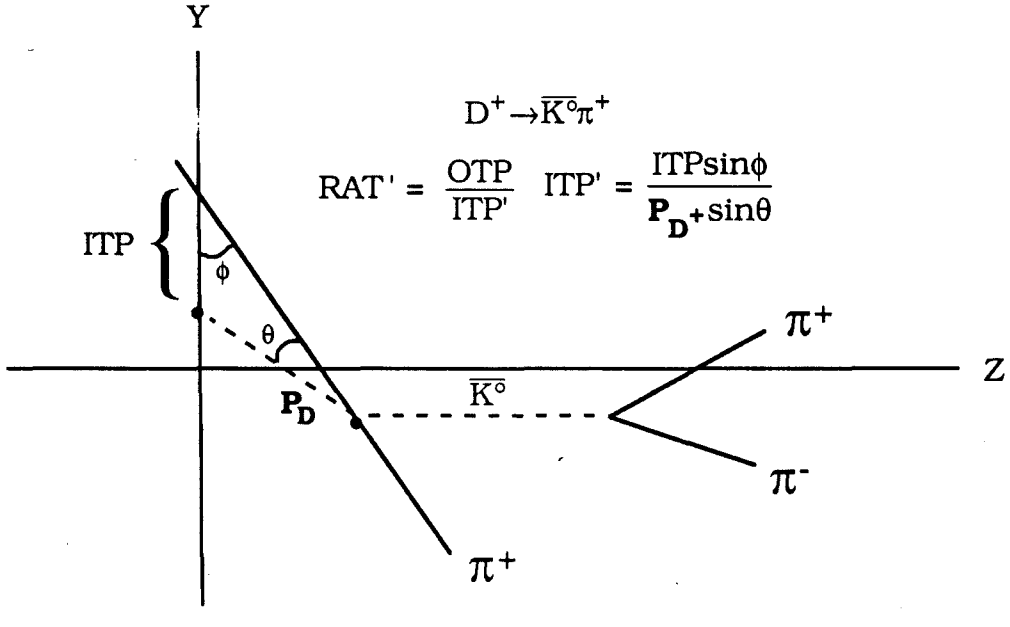

Figure 5.4 Definition of ITP' and RAT' single prong parameters

5.1.4 Invariant mass fitting technique

I fit all the invariant mass histograms obtained in the analyses that follow using a Gaussian function for the signal and either a polynomial or exponential function for the background. The fits were performed by the CERN HBOOK3 routine HFIT. I first fit a invariant mass histogram using the square root of each bin content as an estimate of that bin content's error. As a better estimate of each bin content's error I used the square root of the bin integral of the fitting function. The goodness of a fit was determined by eye and by the χ^2 per degree of freedom of the fit.

In each fit, the Gaussian width was fixed to that calculated from our MC and the central value fixed at the D meson mass (1.865 GeV for D° and 1.869 GeV for D^+). In some analyses two different background functions were tried separately to determine systematic errors due to our fitting procedure.

5.1.5 Optimizing cuts

I determined the best cut values for each parameter in each analysis by maximizing our sensitivity, S, given by

$$S = \frac{S_{mc}}{\sqrt{S_{mc}+B_{data}}}, \qquad (5.1)$$

where S_{mc} is the number of Monte Carlo events (scaled to expected levels) and B_{data} is the number of data events in the signal region. If

no cut value for a parameter increased S, that parameter was not used in the analysis.

5.2 D° Decay Modes

5.2.1 $D^\circ \to \overline{K}^\circ \pi^\circ$

The $D^\circ \to \overline{K}^\circ \pi^\circ$ sample was obtained from the decay chain: $D^{*+} \to D^\circ \pi^+$, $D^\circ \to \overline{K}^\circ \pi^\circ$, $\overline{K}^\circ \to K^\circ_S \to \pi^+\pi^-$, $\pi^\circ \to \gamma\gamma$ (charge conjugate states are implicitly included). I combined each K°_S in each event in the K°_S event set (described in section 4.1) with each reconstructed π° (discussed in section 4.3). The $K^\circ_S \pi^\circ$ invariant mass was computed. To reduce this mode's combinatorial background, I used the D* hypothesis technique (see section 5.1.1) if the $K^\circ_S \pi^\circ$ invariant mass was between 1.55 and 2.3 GeV. A typical D° momentum was about 60/c GeV and a typical K°_S and π° from background events had momenta about 15 GeV/c. An additional requirement of $|\cos(\theta_{cm})| < 0.7$ was imposed where θ_{cm} is the angle of the π° momentum relative to the D° direction in the D° rest frame. The signal should be flat in $\cos(\theta_{cm})$ since the $\overline{K}^\circ$ and π° are in a relative s-wave and the background tends to peak at $\cos(\theta_{cm}) = +1$[†].

The $K^\circ_S \pi^\circ$ invariant mass histogram, displayed in Figure 5.5 was fit using the technique of section 5.1.4. I find 119±15 events of $D^\circ \to K^\circ_S \pi^\circ$. To compute the ratio of $D^\circ \to \overline{K}^\circ \pi^\circ$ to $D^\circ \to K^-\pi^+$ I corrected the signal for the $\overline{K}^\circ \to K^\circ_S$, $K^\circ_S \to \pi^+\pi^-$ branching ratios and for our

[†] We had no acceptance near -1.

reconstruction efficiency of 1.9 ± 0.3% as computed by our MC (after correcting for the $\varepsilon(K^0_S)$ and $\varepsilon(\pi^0)$). I then divided by our $D^{*+}\to D^0\pi^+$, $D^0\to K^-\pi^+$ signal of 13100±580 [So89], giving

$$\frac{BR(D^0\to\overline{K^0}\pi^0)}{BR(D^0\to K^-\pi^+)} = 1.36 \pm 0.23 \pm 0.22 \qquad (5.2)$$

(± statistical ± systematic). Using the Particle Data Group's value of (3.71 ± 0.25)% [Be90] for $BR(D^0\to K^-\pi^+)$, we obtained

$$BR(D^0\to\overline{K^0}\pi^0) = (5.0 \pm 0.8 \pm 0.9)\%. \qquad (5.3)$$

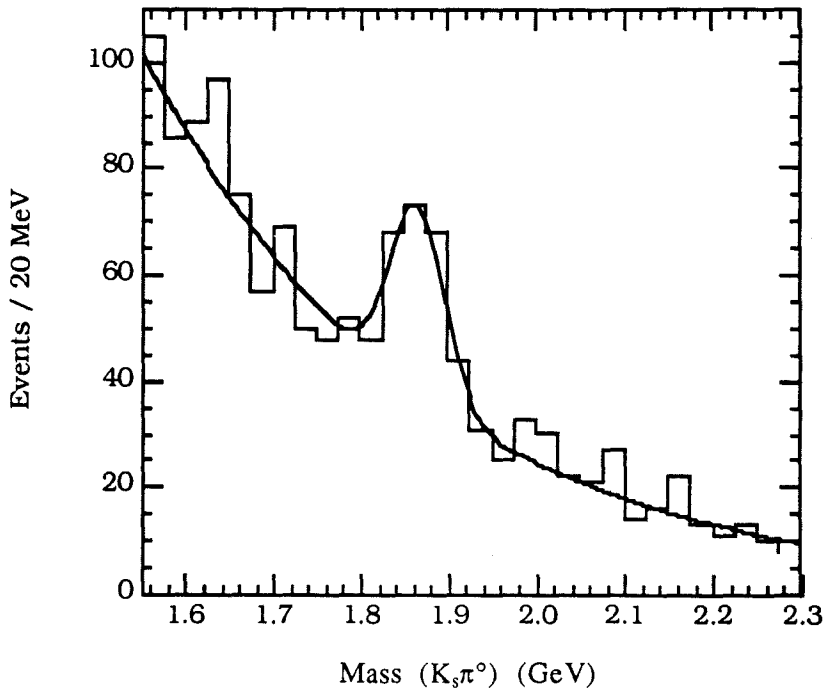

Figure 5.5 $K^0_S\pi^0$ invariant mass histogram from final cuts

5.2.2 $D^\circ \to \overline{K}^\circ K^\circ$

I analyzed the decay mode $D^\circ \to \overline{K}^\circ K^\circ$ by identifying the decay chain: $D^{*+} \to D^\circ \pi^+$, $D^\circ \to \overline{K}^\circ K^\circ$, $\overline{K}^\circ K^\circ \to K^\circ_S K^\circ_S$, $K^\circ_S \to \pi^+\pi^-$. The analysis method was similar to the $D^\circ \to \overline{K}^\circ \pi^\circ$ method. Both K°_S candidates were required to be *good* K°_S's as defined in section 4.1. The resultant $K^\circ_S K^\circ_S$ invariant mass histogram, shown in Figure 5.6, was fit using the technique of section 4.5.4. I used a linear function for the background shape. There is no evidence of a signal in the histogram at the D° mass. I find 0.0 ± 4.5 events of $D^\circ \to K^\circ_S K^\circ_S$. I corrected this result for the $\overline{K}^\circ K^\circ \to K^\circ_S K^\circ_S$ (= 2, see Appendix B), and $K^\circ_S \to \pi^+\pi^-$ branching ratios and for the MC calculated reconstruction efficiency of $6.3 \pm 0.8\%$ (after correcting for the MC K°_S inefficiency). Normalizing to our $D^{*+} \to D^\circ \pi^+$, $D^\circ \to K^-\pi^+$ signal of 13100±580 [So89], I obtained the 90% CL upper limit

$$\frac{BR(D^\circ \to \overline{K}^\circ K^\circ)}{BR(D^\circ \to K^-\pi^+)} < 0.032. \qquad (5.4)$$

Using the Particle Data Group's value of $(3.71 \pm 0.25)\%$ [Be90] for the $D^\circ \to K^-\pi^+$ branching ratio, I obtained the 90% CL upper limit

$$BR(D^\circ \to \overline{K}^\circ K^\circ) < 0.12\%. \qquad (5.5)$$

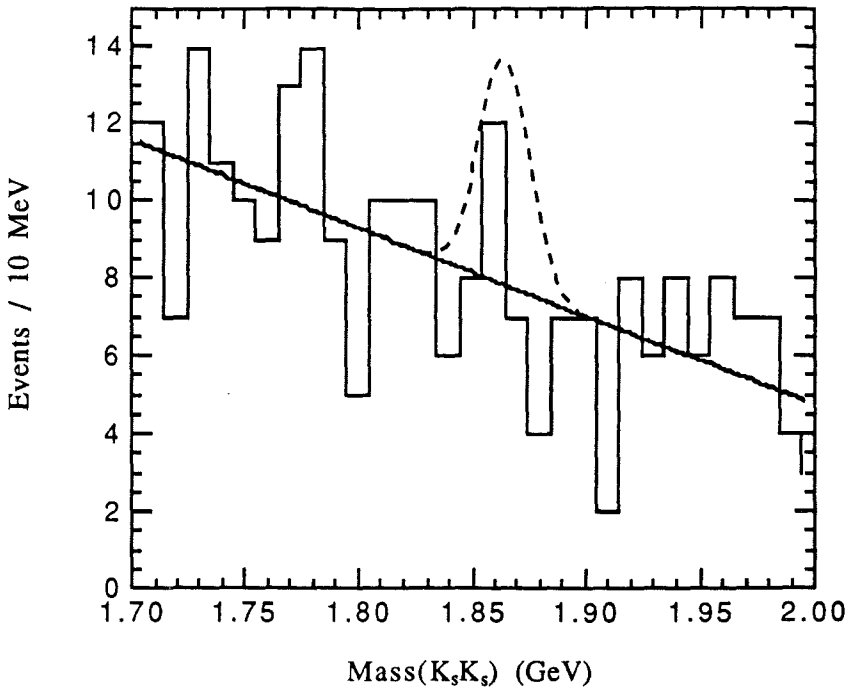

Figure 5.6 $K_S^0K_S^0$ invariant mass histogram from final cuts. Dashed line is 90% CL upper limit

5.2.3 $D^\circ \to \overline{K}^\circ \overline{K}^\circ K^\circ$

The final D° decay mode presented in this thesis is $D^\circ \to \overline{K}^\circ \overline{K}^\circ K^\circ$. It was studied through the decay chain: $D^{*+} \to D^\circ \pi^+$, $D^\circ \to \overline{K}^\circ \overline{K}^\circ K^\circ$, $\overline{K}^\circ \overline{K}^\circ K^\circ \to K_S^0 K_S^0 K_S^0$, $K_S^0 \to \pi^+\pi^-$. I required each D° candidate to be formed from 3 *good* K_S^0's. I obtained the 3 K_S^0 invariant mass histogram of Figure 5.7. I fit this histogram using the fitting technique of section 5.1.4 and obtained the result 6 ± 4 events for a statistical significance of about 1.5σ. Correcting for the $\overline{K}^\circ \overline{K}^\circ K^\circ \to K_S^0 K_S^0 K_S^0$ (see Appendix B) and $K_S^0 \to \pi^+\pi^-$ branching ratios, our reconstruction efficiency of (1.1 ± .2)% (corrected for the MC K_S^0

inefficiency), and normalizing to our $D^{*+}\rightarrow D^{\circ}\pi^{+}$, $D^{\circ}\rightarrow K^{-}\pi^{+}$ signal, I obtained the 90% CL upper limit

$$\frac{BR(D^{\circ}\rightarrow\overline{K^{\circ}}\overline{K^{\circ}}K^{\circ})}{BR(D^{\circ}\rightarrow K^{-}\pi^{+})} < 1.92. \qquad (5.6)$$

Using the Particle Data Group's value of (3.71 ± .25)% for $BR(D^{\circ}\rightarrow K^{-}\pi^{+})$ we get

$$BR(D^{\circ}\rightarrow \overline{K^{\circ}}\overline{K^{\circ}}K^{\circ}) < 7.1\%. \qquad (5.7)$$

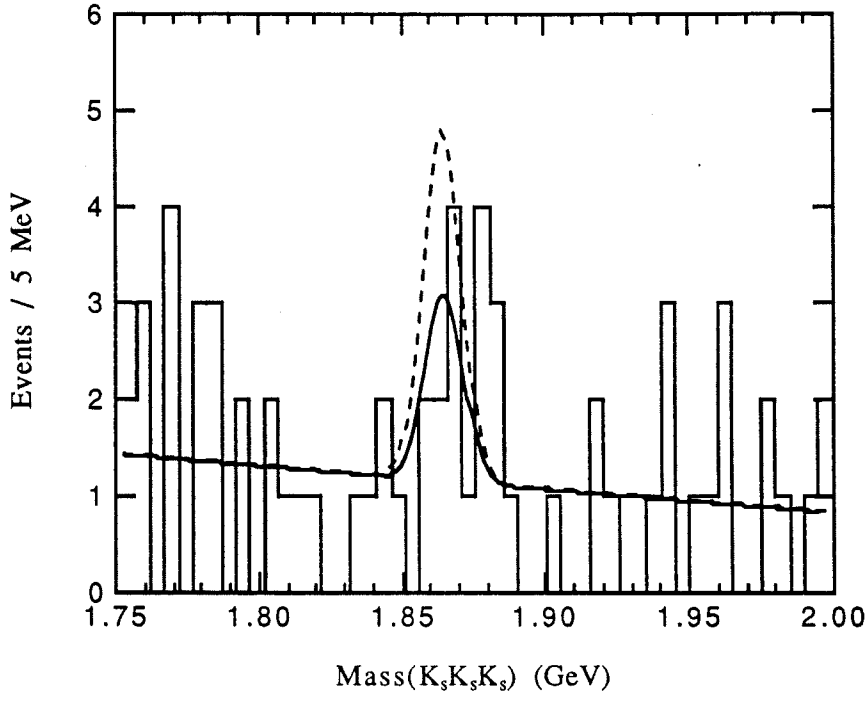

Figure 5.7 $K^{\circ}_{S}K^{\circ}_{S}K^{\circ}_{S}$ invariant mass histogram from final cuts Dashed line is 90% CL upper limit

5.3 D^{+} and Ds^{+} Decay Modes

5.3.1 $D^+ \to \overline{K}^\circ \pi^+$

The decay $D^+ \to \overline{K}^\circ \pi^+$ was identified by the decay chain: $D^+ \to \overline{K}^\circ \pi^+$, $\overline{K}^\circ \to K^\circ_S \to \pi^+\pi^-$. I started with the K°_S event set of section 4.1. To each K°_S I paired each SESTR track π^+ in the same event and computed their invariant masses. For D^+ candidates with mass between 1.7 and 2.1 GeV, I computed their single prong parameters (see sections 5.1.3 and Table 5.1). Next I adjust each parameter's cut value to maximize our sensitivity as described in section 5.1.4. I also required $\cos(\theta_{cm}) < 0.6$ where is the angle of the π^+ with respect to the D^+ momentum in the D^+ rest frame. A fit to the resultant $K^\circ_S \pi^+$ invariant mass histogram, shown in Figure 5.8, yielded 314 ± 29 signal events. This mode's corrected reconstruction efficiency was 6.0 ± .6%. After making adjustments for the $\overline{K}^\circ \to K^\circ_S \to \pi^+\pi^-$ branching ratio and normalizing to our signal for $D^+ \to K^-\pi^+\pi^+$ of 53300 ± 3500 [Be89], I obtained

$$\frac{BR(D^+ \to \overline{K}^\circ \pi^+)}{BR(D^+ \to K^-\pi^+\pi^+)} = 0.29 \pm 0.031 \pm 0.029. \qquad (5.8)$$

I computed the absolute branching ratio using the Particle Data Group's value of (7.1 ± 1.0)% for $BR(D^+ \to K^-\pi^+\pi^+)$ [Be90] and obtained

$$BR(D^\circ \to \overline{K}^\circ \pi^+) = (2.6 \pm 0.3 \pm 0.3)\%. \qquad (5.9)$$

An earlier result from E691 [An90] obtained BR($D^+ \to \overline{K^\circ}\pi^+$) = (2.5 ± .4 ± .3)% which is consistent with my result and has a slightly larger statistical error. My lower error is because I developed a better set of variables to separate signal from background.

Cut Parameter	$D^+ \to \overline{K^\circ}\pi^+$	$D^+ \to \overline{K^\circ}K^{*+}$	$D_S^+ \to \overline{K^\circ}K^{*+}$
OTP (μm)	≤ 80	≤ 80	≤ 80
ITP' (μm)	≥ 120**	≥ 160	≥ 90
SDZ	≥ 7	≥ 7	≥ 5
DCA (μm)	*	≤ 80	≤ 80
RAT' = OTP/ITP	≤ 0.25	*	*
DCAISO (μm)	*	120	*

Table 5.1 Single prong parameter cuts (* cut not used; ** ITP used, not ITP')

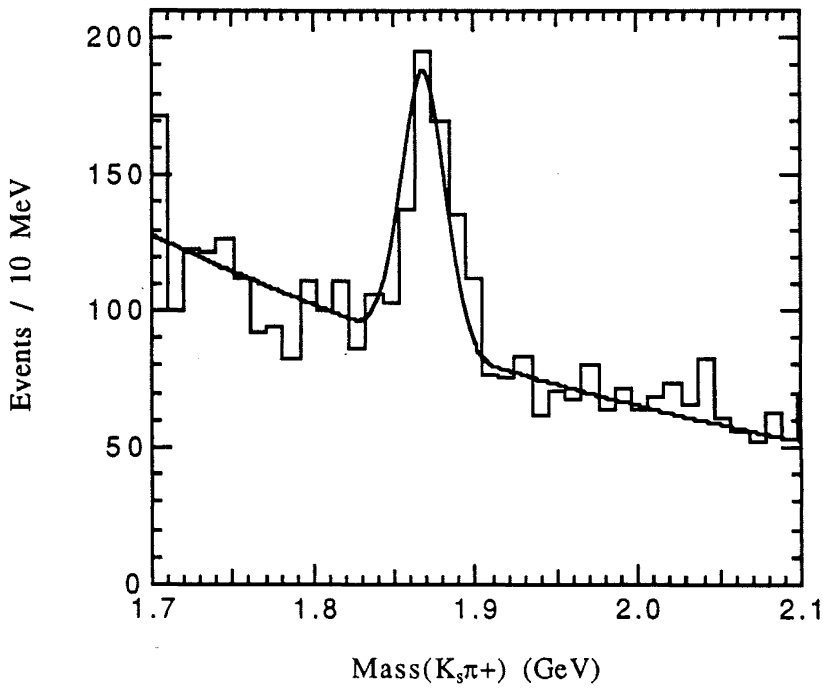

Figure 5.8 $K_S^\circ\pi^+$ invariant mass histogram from D^+ final cuts

5.3.2 $D^+ \to \overline{K}^0 K^{*+}$

I analyzed the decay mode $D^+ \to \overline{K}^0 K^{*+}$, using the decay chain: $D^+ \to \overline{K}^0 K^{*+}$, $K^{*+} \to \overline{K}^0 \pi^+$, $\overline{K}^0 \to K^0_S \to \pi^+\pi^-$. I combined each pair of *good* K^0_S's with each SESTR track π^+. If the $K^0_S K^0_S \pi^+$ invariant mass of a D^+ candidate was between 1.7 and 2.1 GeV, I applied our single prong analysis technique (see section 5.1.3). Next I computed the two possible $K^0_S \pi^+$ invariant mass combinations. I divided our sample into two types of candidates: those with at least one $K^0_S \pi^+$ invariant mass consistent with $M_{K^{*+}}$ ($0.852 < M_{K\pi} < 0.932$ GeV, K* sample) and those with both $K^0_S \pi^+$ invariant masses not consistent with $M_{K^{*+}}$ ($M_{K\pi} <$ 0.852 or $M_{K\pi} > 0.932$ GeV, non-K* sample). The single prong parameter cuts were adjusted to maximize the sensitivity for the K* sample (see Table 5.1). Histograms from both samples (Figures 5.9 and 5.10) were fit separately using the method of section 5.1.4. I found 30 ± 11 events in the K* sample, and 8 ± 15 events in the non-K* sample. The corrected reconstruction efficiencies were both (1.9 ± 0.3)%. The probability of non-K* to K* feedthrough was (0.38 ± 0.08)%, resulting in a possible 2 ± 4 events feedthrough. Using this feedthrough information, the branching ratio for $\overline{K}^0 \to K^0_S \to \pi^+\pi^-$, and normalizing to the mode $D^+ \to K^-\pi^+\pi^+$, I obtained

$$\frac{BR(D^+ \to \overline{K}^0 K^{*+})}{BR(D^+ \to K^-\pi^+\pi^+)} = 0.41 \pm 0.16 \pm 0.09. \qquad (5.10)$$

I computed the absolute branching ratio for this mode, using the Particle Data Group's value for $BR(D^+ \to K^-\pi^+\pi^+)$ of (7.7 ± 1.0)% [Be90] and obtained

$$BR(D^\circ \to \overline{K^\circ} K^{*+}) = (3.2 \pm 1.2 \pm 0.8)\%. \qquad (5.11)$$

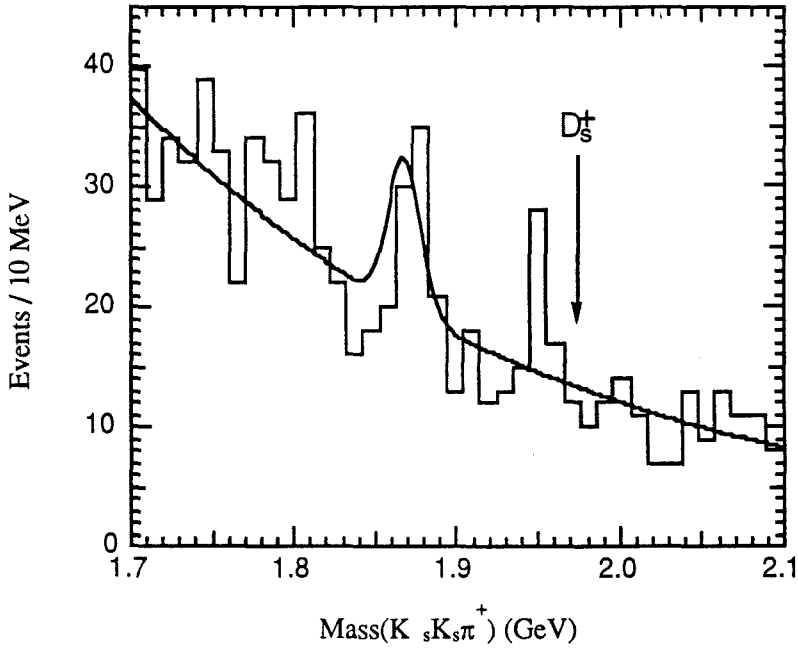

Figure 5.9 $K^\circ_S K^\circ_S \pi^+$ invariant mass histogram from D^+ final cuts on K* sample

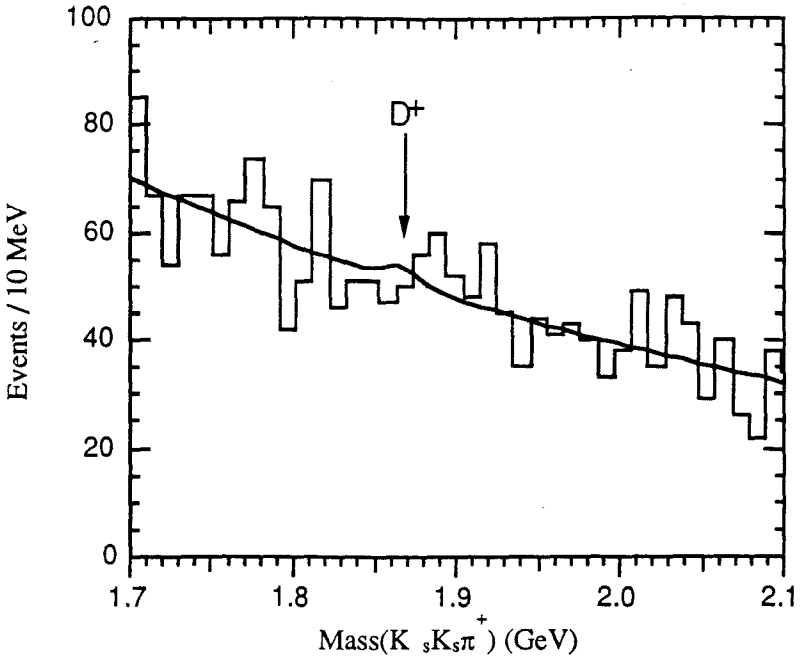

Figure 5.10 $K^0_S K^0_S \pi^+$ invariant mass histogram from D^+ final cuts on non-K* sample

5.3.3 $D_S^+ \to \overline{K^0} K^{*+}$

The final analysis presented in this thesis is of the decay $D_S^+ \to \overline{K^0} K^{*+}$. I used the decay chain: $D_S^+ \to \overline{K^0} K^{*+}$, $K^{*+} \to \overline{K^0} \pi^+$, $\overline{K^0} \to K^0_S \to \pi^+ \pi^-$. The analysis method is identical to the $D^+ \to \overline{K^0} K^{*+}$ analysis just discussed except that the single prong parameter cuts were adjusted to maximize the sensitivity for a D_S^+ decay into this final state (see Table 5.1). The main difference in the cut values is due to the shorter lifetime of the D_S^+ relative to the D^+, as reflected in the ITP' and SDZ cuts. The $K^0_S K^0_S \pi^+$ invariant mass histogram, shown in Figure 5.11, was fit using the method of section 5.1.4. There is no evidence of a signal in the histogram. From my fit I obtained 6 ± 18 events of $D_S^+ \to K^0_S K^0_S \pi^+$. I adjusted for our corrected reconstruction

efficiency (1.5±.2% for $D_S^+ \to K_S^0 K_S^0 \pi^+$) and for the branching ratios $K^{*+} \to \overline{K^0}\pi^+$, $\overline{K^0} \to K_S^0 \to \pi^+\pi^-$. Normalizing to the mode $D^+ \to K^-\pi^+\pi^+$, I obtained the 90% CL upper

$$\frac{BR(D_S^+ \to \overline{K^0}K^{*+})}{BR(D_S^+ \to \phi\pi^+)} < 2.9. \qquad (5.12)$$

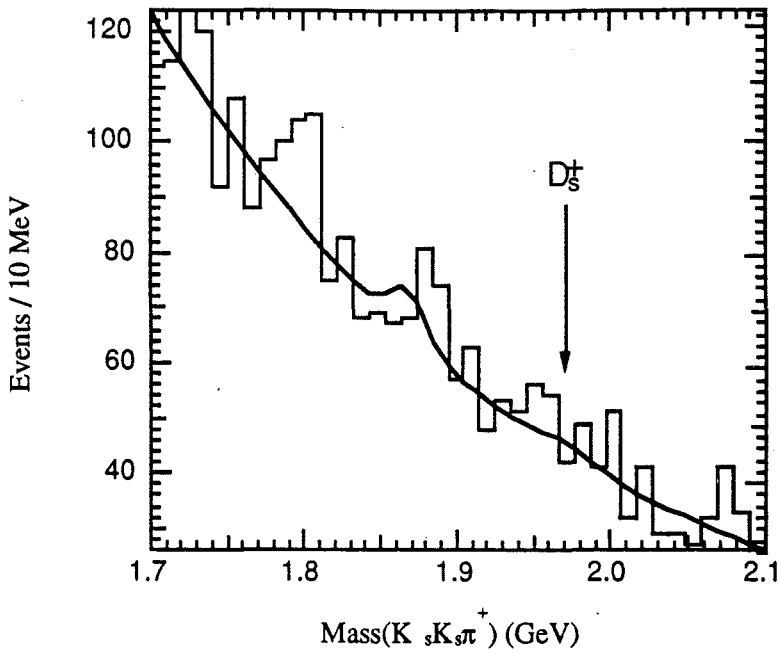

Figure 5.11 $K_S^0 K_S^0 \pi^+$ invariant mass histogram from D_S^+ final cuts

6 Summary

The results presented in Chapter 5 provide some insight into the physical processes involved in the decays of charmed mesons. In this chapter, I summarize these results. I also compare these results with similar experimental measurements and theoretical predictions where possible.

Elastic final state interactions significantly alter the naively computed relative decay rates of $D^\circ \to \overline{K}^\circ \pi^\circ$ and $D^\circ \to K^- \pi^+$. Since the weak components and available phase space of the two decays are the same, any difference in the two branching ratios must lie in the quark recombination process. Two possible explanations are that any color suppression is reduced by elastic final state interactions or that color suppression is non-existent due to bleaching. All the measurements of $BR(D^\circ \to \overline{K}^\circ \pi^\circ)$, listed in Table 6.1, are much higher than the predictions from a simple color suppression model, although they do allow some color suppression and are consistent with the predictions made by Donoghue [Do86] and Bauer *et.al.* [Ba87] when elastic final state interactions are included. Similar results for other D decays (summarized in Table 6.2) indicate either color suppression is almost completely reduced by final state interactions or bleaching, or that there is no suppression at all.

Mode	CLEO [Al90]	Mark III [Hi87]	E691	Theory [Ba87]
BR($D^\circ \to \overline{K}^\circ \pi^\circ$)	2.3±0.4±0.5	1.9±0.4±0.4	5.0±0.8±0.9	2.4
BR($D^\circ \to \overline{K}^\circ \pi^+$)	-	3.2±0.5±0.2	2.6±0.3±0.3	3.6
BR($D^\circ \to K^- \pi^+$)	-	4.2±0.4±0.4	-	5.8

Table 6.1 $D \to K\pi$ decay modes used to explore elastic final state interactions

Mode	BR(Inner-W)	BR(Outer-W)	$\frac{\text{BR(Inner-W)}}{\text{BR(Outer-W)}}$
$D^\circ \to K\pi$	$BR(D^\circ \to \overline{K}^\circ \pi^\circ) =$ $5.0\pm0.8\pm0.9$	$BR(D^\circ \to K^- \pi^+) =$ 3.71 ± 0.25^a	$1.36\pm0.23\pm0.22$
$D^\circ \to KK\ (\phi\pi)$	$BR(D^\circ \to K^+K^-) =$ 0.45 ± 0.07^a	$BR(D^\circ \to \phi\pi^\circ) =$ -	-
$D^+ \to KK\ (\phi\pi)$	$BR(D^+ \to \overline{K}^\circ K^+) =$ $0.68\pm0.2\pm0.1^b$	$BR(D^+ \to \phi\pi^+) =$ 0.57 ± 0.11^a	0.83 ± 0.31
$D_s^+ \to \phi\pi\ (KK)$	$BR(D_s^+ \to \phi\pi^+) =$ 2.6 ± 0.8^a	$BR(D_s^+ \to \overline{K}^\circ K^+) =$ 2.7 ± 0.7^a	0.96 ± 0.39

Table 6.2 Summary of BR(Inner-W) to BR(Outer-W) ratios for various D decays. BR's are in percent. ([a] are from [Be90], [b] is from [An90])

The evidence for the existence and level significance of inelastic final state interactions is not conclusive, as seen in Table 6.3. This table lists the decay modes which are sensitive to final state interactions as discussed in section 1.4.2. The results of CLEO [Al89]

and E400 [Cu88] for $D^\circ \to \overline{K}^\circ K^\circ$ are statistically significant. The upper limits of E691 and ARGUS [Al89a] favor the lower part of CLEO's and E400's error bars when considering the decay rate. All the results for this mode are about 2 to 3 times smaller than the prediction of Pham [Ph87]. The E691 upper limits for $BR(D^\circ \to \overline{K^*}^\circ K^\circ)$ and $BR(D^\circ \to \overline{K}^\circ K^{*\circ})$ are consistent with the $BR(D^\circ \to \overline{K}^\circ K^\circ)$ results. A point of departure is the mode $D^\circ \to \overline{K^*}^\circ K^{*\circ}$ with a branching ratio about 2.5 times larger than my upper limit for $D^\circ \to \overline{K}^\circ K^\circ$. While its available phase space is half that of $D^\circ \to \overline{K}^\circ K^\circ$, its number of helicity states is larger.

Result	ARGUS [Al89a]	CLEO [Al89]	MARK III [Ad88]	E400 [Cu88]	E691	Theory [Ph87]
$BR(D^\circ \to \overline{K}^\circ K^\circ)$	< 0.11	$0.13^{+0.07+0.02}_{-0.05-0.02}$	<0.46	0.10±0.08*	<0.12	0.3
$BR(D^\circ \to \overline{K}^\circ K^{*\circ})$	-	-	-	-	<0.22†	-
$BR(D^\circ \to \overline{K^*}^\circ K^\circ)$	-	-	-	-	<0.13†	-
$BR(D^\circ \to \overline{K^*}^\circ K^{*\circ})$	-	-	-	-	$0.33^{+0.18}_{-0.15}\pm0.07$†	-

Table 6.3 Results for the decay $D^\circ \to \overline{K}^\circ K^\circ$ and similar, in percent. All upper limits are 90% CL. (* value was derived from reported measurement using $BR(D^\circ \to K^+K^-) = 0.45\pm0.07\%$ [Be90], † are from [An91])

Outer-W spectator D decays with a vector meson formed directly from the W boson are consistently favored over other corresponding decays. Table 6.4 displays the ratios of branching ratios for several sets of D→PP, D→PV, D→VP and D→VV decays. Figure 6.1 illustrates the spectator decays for these forms. All the ratios are consistent with the D→PV being favored by a factor of two over D→PP and D→VP.

There are no measurements yet on decays of the form D→VV for these general decay modes.

General Decay	$\frac{BR(D\to PV)}{BR(D\to PP)}$	$\frac{BR(D\to PV)}{BR(D\to VP)}$	$\frac{BR(D\to PV)}{BR(D\to VV)}$
$D^\circ\to K^-\pi^+$	$\frac{BR(D^\circ\to K^-\rho^+)}{BR(D^\circ\to K^-\pi^+)} =$ 2.1 ± 0.3	$\frac{BR(D^\circ\to K^-\rho^+)}{BR(D^\circ\to K^{*-}\pi^+)} =$ 1.7 ± 0.33	$\frac{BR(D^\circ\to K^-\rho^+)}{BR(D^\circ\to K^{*-}\rho^+)} =$ -
$D^\circ\to K^-K^+$	$\frac{BR(D^\circ\to K^-K^{*+})}{BR(D^\circ\to K^-K^+)} =$ 1.5 ± 0.8	$\frac{BR(D^\circ\to K^-K^{*+})}{BR(D^\circ\to K^{*-}K^+)} =$ > 4.1	$\frac{BR(D^\circ\to K^-K^{*+})}{BR(D^\circ\to K^{*-}K^{*+})} =$ -
$D^+\to K^\circ\pi^+$	$\frac{BR(D^+\to \overline{K^\circ}\rho^+)}{BR(D^\circ\to \overline{K^\circ}\pi^+)} =$ 2.5 ± 0.6	$\frac{BR(D^+\to \overline{K^\circ}\rho^+)}{BR(D^\circ\to \overline{K^{*\circ}}\pi^+)} =$ 3.9 ± 2.1	$\frac{BR(D^+\to \overline{K^\circ}\rho^+)}{BR(D^\circ\to \overline{K^{*\circ}}\rho^+)} =$ -
$D^+\to K^\circ K^+$	$\frac{BR(D^+\to \overline{K^\circ}K^{*+})}{BR(D^\circ\to \overline{K^\circ}K^+)} =$ 3.8 ± 2.1	$\frac{BR(D^+\to \overline{K^\circ}K^{*+})}{BR(D^\circ\to \overline{K^{*\circ}}K^+)} =$ 7.4 ± 3.7	$\frac{BR(D^+\to \overline{K^\circ}K^{*+})}{BR(D^\circ\to \overline{K^{*\circ}}K^{*+})} =$ -

Table 6.4 Ratio of branching ratios for D→PP, D→PV, and D→VP and D→VV decays. ($D^\circ\to K^-\pi^+$, $D^\circ\to K^-\rho^+$, $D^\circ\to K^{*-}\pi^+$, $D^\circ\to K^-K^+$, $D^+\to \overline{K^\circ}K^+$, $D^+\to \overline{K^{*\circ}}\pi^+$, $D^+\to \overline{K^\circ}\rho^+$ from [Be89], $D^\circ\to K^-K^{*+}$, $D^\circ\to K^{*-}K^+$ from [An91]).

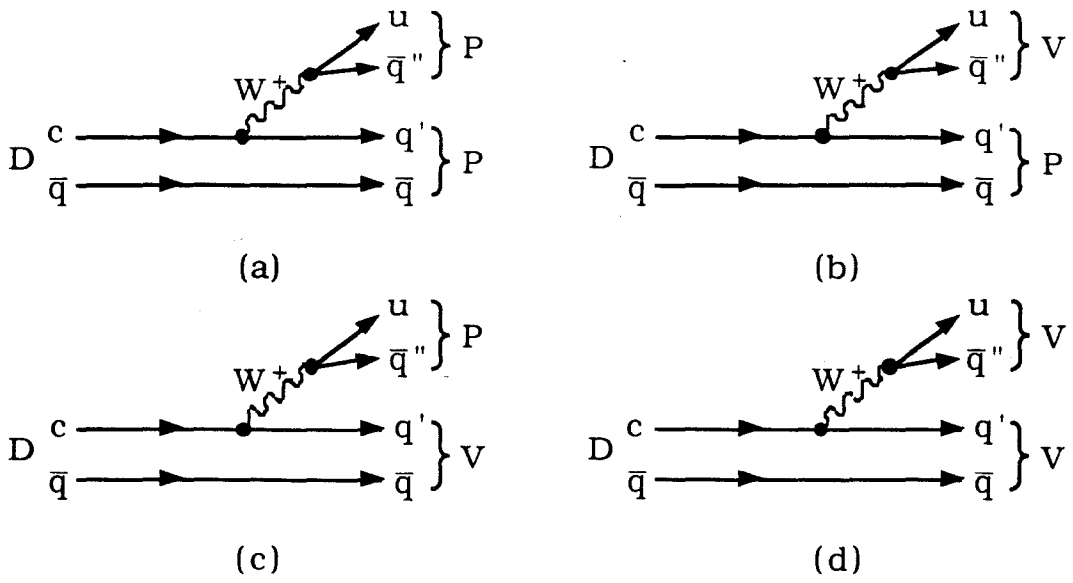

Figure 6.1 Outer-W spectator decays of the form: (a) D→PP, (b) D→PV, (c) D→VP and (d) D→VV

I have presented several measurements of D meson branching ratios which aid in the understanding of quark recombination affects in weak charm decays. I have compared these measurements with similar results and with theoretical predicts. The full utility of these measurements will be reached when additional decay rates, sensitive to quark recombination processes, are made and incorporated into a complete theorectical frame-work. Hopefully this frame-work will clearify how quark recombination processes effect bottom (and perhaps top?) weak decay.

References

An83 B. Anderson, G. Gustafson, C Ingelman, T. Sjöstrand, Phys. Rep. **97**, 31 (1983).

An87 J. Anjos *et al.*, PRL **58** 311 (1987).

An90 J. Anjos *et al.*, Phys. Rev. D41 2705 (1990).

An91 J. Anjos *et al.*, Phys. Rev. D43 R635 (1991).

Au74 J.J. Augert *et al.*, Phys. Rev. Lett. **33**, 1404 (1974).

Au74a J.E. Augustin *et al.*, Phys. Rev. Lett. **33**, 1406 (1974).

Be89 A. Bean, *An Update of Charmed Meson Branching Ratios Measured by E691*, an E691 internal memo (1989).

Bi80 I.I.Y. Bigi and M. Fukugita, Phys. Lett. **91B**, 121 (1980).

Bi88 I.I. Bigi, On Charm Decays - Present Status and Future Goals, in Charm Physics, eds. Ming-han Ye and Tao Huang, (Gordon and Breach, New York, 1988), p. 339.

Bj64 J.D.Bjorken and S.L. Glashow, Phys. Lett. **11**, 255-257 (1964).

Br88 T. Browder, *A study of D^0-$\overline{D^0}$ Mixing*, Ph.D. thesis, University of California Santa Barbara, UCSB-HEP-88-4 (1988).

Br88a T. Browder, *A Test of the Monte Carlo π^0 Simulation*, internal E691 memo, (1988).

Ca78 N. Cabibbo and L. Maiani, Phys. Lett. **73B**, 418 (1978).

De90 D.F. DeJongh, *Resonant Substructure in Anti-K PI PI PI Decays of D Mesons*, Ph.D. thesis, California Institute of Technology.

Do86 J.F. Donoghue, Phys. Lett. **193B**, 331 (1986).

Fa78 D. Fakirov and B. Stech, Nucl. Phys. **B133**, 315 (1978).

Fo81 M. Fontannaz, B. Pire, and D. Schiff, Z. Phys. **C11**, 201 (1981).

Gl70 S.L. Glashow, J. Iliopoulos, and L. Maiani, Phys. Rev. **D2**, 1285 (1970).

Go76 G. Goldhaber *et al.*, Phys. Rev. Lett. **37**, 255 (1976).
I. Peruzzi *et al.*, Phys. Rev. Lett. **37**, 569 (1976).

Go84 T. Gottschalk, *Hadronization and Fragmentation*, Th 3810-CERN, (1984).

Ha86 G. Hartner, *S1234*, an E691 internal memo (1986).

He90 J.J. Hernandez *et al.* (Particle Data Group), Phys. Lett. **B239**, VII.117 (1990).

Jo78 L. Jones and H. Wyld, Phys. Rev. **D17**, 612 (1978).

Ka85 P. Karchin, *et al.*, IEEE NS-32, 612 (1985).

Na86 T. Nash *et al.*, Proceedings of the XXIII Int'l Conference on High Energy Physics, Berkeley CA, (1986).

Ph87 X.Y. Pham, Phys. Lett. **B193**, 331 (1987).

Pu85 M. Purohit, E-691 Internal Memo on the E_T trigger (1985).

Pu89 G. Punkar, *Meassurements of Ds Decays and Cabibbo-Suppressed D^+ Decays*, Ph.D. thesis, University of California Santa Barbara, UCSB-HEP-89-03 (1989).

Ra87 J. Raab, *Lifetime Measurements of the Three Charmed Pseudoscalar D-Mesons*, Ph.D. thesis, University of California Santa Barbara, UCSB-HEP-87-8 (1987).

Re90 P. Renton, Electroweak Interactions, Chambridge University Press, pp. 413-418 (1990).

Su84 D. Summers, *A study of the Decay* $D^{\circ} \rightarrow K^{-}\pi^{+}\pi^{\circ}$ *in High Energy Photoproduction*, Ph.D. thesis, University of California Santa Barbara (1984).

So89 M. Sokoloff, private communication (1989).

So91 M. Sokoloff, private communication (1991).

Appendix A

Table A.1 Per-Plane Efficiencies vs. Track Momentum

Category-15 SESTR — SMD PER PLANE EFFICIENCIES — MC: DST8385

P AVG.	PLANE-1	PLANE-2	PLANE-3	PLANE-4	PLANE-5	PLANE-6	PLANE-7	PLANE-8	PLANE-9	AVERAGE	
				(NOTE: FIRST 2 LINES FROM CAT-3)							
2.7	84.5 ± .5	92.3 ±. .4	88.8 . ± 4	81.7 . ± 5	89.4 ± .4	78.6 . ± 5	91.4 . ± 4	94.4 . ± 3	88.8 . ± 5	87.5 ± 2	
6.7	93.9 ± .7	95.6 ± .6	90.2 ± .8	92.8 ± .7	93.0 ± .7	82.9 ± 1.0	92.4 ± .7	94.0 ± .7	87.2 ± .9	91.2 ± .3	
4.1	82.2 ± .6	93.6 ± .1	87.9 ± .4	79.6 ± .7	91.2 ± .3	86.2 ± 5	92.8 ± 1.1	95.7 ± 9	89.1 ± 1.4	88.4 ± .5	
75	90.9 ± .6	95.2 ± .4	93.4 ± 5	89.6 ± 6	91.1 ± 6	91.2 ± 6	92.5 ± .5	95.7 ± 4	92.3 ± .5	92.4 ± .5	
12.2	94.1 ± .6	95.0 ± .5	95.1 ± .5	94.3 ± .5	92.6 ± .6	94.7 ± .5	94.4 ± .5	96.4 ± .4	93.6 ± .6	94.5 ± .2	
17.2	95.2 ± .7	95.5 ± .7	94.7 ± .7	94.3 ± .8	91.3 ± .9	95.1 ± .7	96.0 ± .6	94.4 ± 8	93.8 ± 8	94.5 ± 3	
22.2	93.5 ± 1.2	95.3 ± 1.0	93.7 ± 1.1	94.3 ± 1.1	91.3 ± 1.3	92.5 ± 1.2	93.9 ± 1.1	95.8 ± 1.0	90.7 ± 1.3	93.4 ± .4	
27.4	94.4 ± 1.3	95.6 ± 1.2	96.3 ± 1.1	95.0 ± 1.3	92.8 ± 1.5	95.9 ± 1.1	92.8 ± 1.5	95.0 ± 1.3	95.9 ± 1.1	94.8 ± .4	
32.2	96.5 ± 1.4	98.2 ± 1.0	92.7 ± 2.0	95.9 ± 1.5	91.1 ± 2.1	97.6 ± 1.2	95.3 ± 1.6	93.7 ± 1.8	94.8 ± 1.7	95.0 ± .6	
37.2	96.1 ± 1.7	93.9 ± 2.1	97.6 ± 1.3	96.9 ± 1.5	92.5 ± 2.3	97.6 ± 1.3	95.4 ± 1.8	97.6 ± 1.3	93.9 ± 2.1	95.7 ± .6	
42.5	94.9 ± 2.5	97.4 ± 1.8	94.9 ± 2.5	94.9 ± 2.5	92.6 ± 2.9	92.6 ± 2.9	92.6 ± 2.9	93.8 ± 2.7	92.6 ± 2.9	94.0 ± 9	
60.1	94.2 ± 1.8	93.6 ± 1.9	95.9 ± 1.5	95.3 ± 1.6	94.7 ± 1.7	95.3 ± .6	95.9 ± 1.5	94.2 ± 1.8	91.5 ± 2.1	94.5 .6	Plane Averages

Category-15 SESTR — D1 PER PLANE EFFICIENCIES — MC: DST8385

P AVG	PLANE-1	PLANE-2	PLANE-3	PLANE-4	PLANE-5	PLANE-6	PLANE-7	PLANE-8	AVERAGE	
				(NOTE: FIRST 2 LINES FROM CAT-3)						
2.6	94.2 ± .3	95.0 . ± 3	93.9 ± .3	93.7 ± .3	95.6 ± .2	94.9 ± .3	91.9 ± 3	93.4 ± .3	94.0 ± .1	
6.7	91.7 ± .7	94.6 ± .6	92.7 ± .7	92.4 ± .7	94.9 ± .6	94.3 ± .6	91.0 ± .7	91.1 ± .7	92.8 ± .2	
4.0	93.5 ± 1.0	91.8 ± 1.1	91.1 ± 1.1	90.7 ± 1.1	91.7, ± 1.1	92.7 ± 1.0	89.6 ± 1.2	91.3 ± 1.1	91.5 ± .4	
7.5	91.1 ± .6	92.6 ± .5	89.1 ± .6	90.2 ± .6	92.5 ± .5	92.5 ± .5	87.8 ≠ .6	91.0 ± 6	90.8 ± .2	
12.2	91.7 ± .7	90.6 ± .7	89.9 ± .8	89.0 ± .8	92.7 ± .7	92.9 ± .7	86.7 ± .8	90.1 ± 8	90.4 ± 3	
17.1	90.4 ± 1.0	91.5 ± 1.0	89.5 ± 1.1	90.9 ± 1.0	91.2 ± 1.0	93.2 ± .9	85.1 = 1.2	91.2 ± 1.0	90.3 ± .4	
22.3	92.4 ± 1.3	92.4 ± 1.3	89.2 ± 1.5	89.6 ± 1.5	90.4 ± 1.4	91.1 ± 1.4	90.9 ± 1.4	90.4 ± 1.4	90.8 ± .5	
27.3	89.8 ± 2.0	85.7 ± 2.3	87.9 ± 2.1	91.9 ± 1.8	91.9 ± 1.8	92.3 ± 1.8	78.7 ± 2.5	88.3 ± 2.1	88.1 ± .6	
32.2	92.0 ± 2.3	91.4 ± 2.4	90.7 ± 2.5	90.1 ± 2.5	93.4 ± 2.1	92.7 ± 2.2	84.7 ± 2.9	85.2± 2.9	89.9 ± .9	
37.1	83.7 ± 3.7	93.2 ± 2.7	88.2 ± 3.3	93.2 ± 2.7	91.1 ± 3.0	90.1 ± 3.1	82.8 ± 3.8	81.2 ± 3.9	87.7 ± 2	
42.4	85.1 ± 4.4	90.5 ± 3.7	90.5 ± 3.7	95.0 ± 2.8	82.6 ± 4.6	96.6 ± 2.4	82.6 ± 4.6	85.1 ± ¢.4	88.2 ± 4	
61.0	86.5 ± 2.9	91.7 ± 2.4	91.0 ± 2.5	89.7 ± 2.6	87.8 ± 2.8	87.1 ± 2.8	85.3 ± 3.0	90.4 ± 2.5	88.6 ± 1.0	
13.4	91.2 ± .3	91.6 ± .3	89.6 ± .4	90.1 ± .4	91.9 ± .3	92.5 ± .3	87.0 ± .4	90.4 ± 4	90.5 ± .1	Plane Averages

Table A.1 Per-Plane Efficiencies vs. Track Momentum

Category-15 SESTR — D2 PER PLANE EFFICIENCIES — MC: DST8385

P AVG	PLANE-1	PLANE-2	PLANE-3	PLANE-4	PLANE-5	PLANE-6	PLANE-7	PLANE-8	PLANE-9	PLANE-10	PLANE-11	PLANE-12	AVERAGE	
						(NOTE: FIRST 2 LINES FROM CAT-3)								
2.6	89.3 ± .4	90.6 ± .3	85.3 ± .4	88.2 ± .4	87.8 ± .4	86.3 ± .4	90.7 ± .3	92.1 ± .3	88.1 ± .4	89.4 ± .4	90.4 ± .3	88.5 ± .4	88.9 ± .1	
6.7	89.7 ± .8	89.4 ± .8	85.9 ± .9	87.3 ± .8	86.4 ± .8	87.4 ± .8	89.6 ± .8	91.1 ± .7	85.9 ± .9	89.6 ± .8	87.8 ± .8	89.9 ± .8	88.3 ± .2	
4.1	84.1 ± 1.4	85.3 ± 1.4	80.1 ± 1.5	84.1 ± 1.4	85.3 ± 1.4	83.2 ± 1.4	87.5 ± 1.3	86.8 ± 1.3	80.1 ± 1.5	87.4 ± 1.3	83.9 ± 1.4	87.1 ± 1.3	84.5 ± .4	
7.5	86.4 ± .6	85.7 ± .7	82.3 ± .7	85.8 ± .7	85.6 ± .7	82.9 ± .7	88.1 ± .6	87.4 ± .6	84.6 + .7	88.7 ± .6	85.0 ± .7	87.1 ± .6	85.8 + .2	
12.2	86.7 ± .8	85.9 ± .8	79.6 ± .9	85.4 ± .8	86.± 1 .8	85.3 ± .8	88.9 ± .8	88.8 ± .8	84.7 ± .9	89.1 ± .8	83.8 ± .9	87.9 ± .8	86.0 ± .2	
17.2	85.6 ± 1.2	84.0 ± 1.2	81.3 ± 1.3	85.9 ± 1.2	86.6 ± 1.1	84.0 ± 1.2	89.8 ± 1.0	89.6 ± 1.0	84.9 ± 1.2	88.1 ± 1.1	85.2 ± 1.2	87.7 ± 1.1	86.0 ± .3	
22.2	86.2 ± 1.6	85.9 ± 1.6	82.8 ± 1.7	86.6 ± 1.6	83.1 ± 1.7	84.7 ± 1.6	88.7 ± 1.5	89.5 ± 1.4	85.2 ± 1.6	90.6 ± 1.4	81.9 ± 1.7	85.8 ± 1.6	85.9 ± .5	
27.4	87.7 ± 2.0	85.5 ± 2.1	80.1 ± 2.3	81.9 ± 2.2	88.6 ± 1.9	84.4 ± 2.2	87.5 ± 2.0	88.7 ± 1.9	87.5 ± 2.0	85.0 ± 2.2	84.0 ± 2.2	83.6 ± 2.2	85.3 ± .6	
32.2	80.7 ± 3.1	81.0 ± 3.1	79.5 ± 3.2	83.9 ± 3.0	85.4 ± 2.8	88.7 ± 2.6	87.7 ± 2.7	91.3 ± 2.3	79.3 ± 3.2	88.8 ± 2.6	82.0 ± 3.0	88.9 ±2.5	84.6 ± .8	
37.2	85.7 ± 3.1	86.1 ± 3.1	82.8 ± 3.4	83.3 ± 3.3	90.6 ± 2.7	81.6 ± 3.5	91.5 ± 2.6	87.5 ± 3.0	85.5 ± 3.3	90.8 ± 2.6	85.1 ± 3.2	86.4 ± 3.1	86.4 ± 2.9	
42.4	85.5 ± 4.0	79.7 ± 4.5	75.3 ± 4.9	84.4 ± 4.1	82.7 ± 4.4	83.1 ± 4.4	82.7 ± 4.4	92.9 ± 3.1	84.0 ± 4.2	90.1 ± 3.5	90.3 ± 3.5	84.6 ± 4.1	84.5 ± 1.2	
60.2	88.9 ± 2.5	82.4 ± 2.9	81.0 ± 3.0	85.5 ± 2.7	84.2 ± 2.8	87.1 ± 2.6	86.5 ± 2.6	90.9 ± 2.2	81.6 ± 2.9	88.4 ± 2.5	88.3 ± 2.5	87.3 ± 2.6	85.9 ± 8	
13.7	86.1 ± .4	85.3 ± .4	81.1 ± .4	85.3 ± .4	85.8 ± .4	84.0 ± .4	88.4 ± .4	88.3 ± .4	84.2 ± .4	88.6 ± .4	84.5 ± .4	87.1 ± .4	85.7± .1	Plane Averages

Category-15 SESTR — D3 PER PLANE EFFICIENCIES — MC: DST8385

P AVG	PLANE-1	PLANE-2	PLANE-3	PLANE-4	PLANE-5	PLANE-6	PLANE-7	PLANE-8	PLANE-9	PLANE-10	PLANE-11	PLANE-12	AVERAGE	
4.1	85.6 ± 1.4	861 ± 1.4	85.1 ± 1.4	75.8 ± 1.6	84.3 ± 1.4	66.4 ± 1.7	85.3 ± 1.4	91.7 ± 1.1	87.9 ± 1.3	93.2 ± 1.0	79.6 ± 1.5	90.6 ± 1.2	84.0 .4	
7.4	86.2 ± .6	90.0 ± .6	88.0 ± .6	79.5 ± .7	85.5 ± .7	68.4 ± .8	86.5 ± .6	90.8 ± .5	90.5 ± .6	93.5 ± .5	80.2 ± .7	91.5 ± .5	85.5 ± .2	
12.2	86.1 ± .8	90.3 ± .7	86.0 ± .8	79.1 ± 1.0	84.3 ± .9	69.5 ± 1.0	86.1 ± .8	90.5 ± .7	89.3 ± .7	92.4 ± .6	84.8 ± .9	92.3 ± .6	85.6 ± .2	
17.1	86.3 ± 1.1	90.5 ± 1.0	86.0 ± 1.1	78.6 ± 1.3	84.5 ± 1.2	69.5 ± 1.4	88.4 ± 1.1	90.0 ± 1.0	90.0 ± 1.0	93.3 ± .8	88.0 ± 1.1	91.8 ± .9	86± 1 .3	
22.2	87.2 ± 1.5	89.7 ± 1.4	85.2 ± 1.6	81.2 ± 1.8	84.5 ± 1.6	64.8 ± 2.1	84.3 ± 1.7	87.9 ± 1.5	90.1 ± 1.4	92.9 ± 1.2	90.2 ± 1.4	89.5 ± 1.4	85.3 ± .5	
27.4	82.8 ± 2.2	89.1 ± 1.8	89.1 ± 1.8	79.9 ± 2.3	87.0 ± 1.9	70.4 ± 2.5	87.0 ± 1.9	89.0 ± 1.8	88.8 ± 1.9	92.3 ± 1.6	92.7 ± 1.5	90.8 ± 1.7	86.3 ± .6	
32.2	87.7 ± 2.6	90.2± 3	88.7 ± 2.4	78.2 ± 3.1	87.3 ± 2.6	68.2 ± 3.3	89.6 ± 2.4	90.3 ± 2.3	89.6 ± 2.4	92.4 ± 2.1	87.8 ± 2.6	90.8 ± 2.3	86.4 ± .8	
37.1	84.0 ± 3.3	89.8 ± 2.8	88.6 ± 2.9	80.0 ± 3.7	86.3 ± 3.1	67.9 ± 3.9	81.3 ± 3.5	92.4 ± 2.4	86.0 ± 3.2	93.1 ± 2.4	93.9 ± 2.2	92.2 ± 2.5	85.9 ± .9	
42.3	73.0 ± 4.9	90.0 ± 3.4	93.3 ± 2.9	72.1 ± 4.8	96.0 ± 2.3	65.2 ± 5.0	81.5 ± 4.3	92.2 ± 3.1	86.3 ± 3.9	88.3 ± 3.7	92.2 ± 3.1	95.9 ± 2.3	84.9 ± 1.2	
60.3	85.0 ± 2.7	91.1 ± 2.2	88.6 ± 2.5	79.8 ± 3.0	88.8 ± 2.4	70.7 ± 3.3	88.7 ± 2.4	89.7 ± 2.3	91.0 ± 2.2	92.2 ± 2.1	90.6 ± 2.2	90.7 ± 2.2	87.0 ± .7	
13.8	85.9 ± .4	89.8 ± .4	87.0 ± .4	79.0 ± .5	85.2 ± .4	68.5 ± .5	86.4 ± .4	90.4 ± .3	89.7 ± .4	93.0 ± .3	83.9 ± .4	91.5 ± .3	85.6 ± .1	Plane Averages

Table A.1 Per-Plane Efficiencies vs. Track Momentum

Category-15 SESTR MC: DST8385

D4 PER PLANE EFFICIENCIES

P AVG	PLANE-1	PLANE-2	PLANE-3	AVERAGE	
4.1	60.8 ± 2.0	73.5 ± 2.0	57.0 ± 1.9	63.0 ± 1.2	
7.5	74.6 ± .9	76.6 ± .8	64.2 ± .9	71.4 ± .5	
12.2	80.4 ± 1.0	77.3 ± 1.0	67.2 ± 1.1	74.5 ± .6	
17.1	79.9 ± .4	76.3 ± 1.5	67.9 ± 1.5	74.3 ± .8	
22.2	77.9 ± 2.0	74.0 ± 2.1	66.1 ± 2.1	72.3 ± 1.2	
27.4	82.0 ± 2.6	73.1 ± 2.8	57.6 ± 2.8	69.4 ± 1.6	
32.2	83.3 ± 3.1	79.5 ± 3.3	64.5 ± 3.5	74.8 ± 2.0	
37.2	77.1 ± 4.3	66.7 ± 4.5	64.3 ± 4.5	68.9 ± 2.6	
42.4	81.2 ± 4.7	80.0 ± 4.8	61.5 ± 5.1	73.0 ± 2.9	
60.6	86.2 ± 2.8	77.5 ± 3.2	69.7 ± 3.4	77.2 ± 1.9	
13.9	76.4 ± .5	76.2 ± .5	64.7 ± .5	72.0 ± .3	Plane averages

Table A.1 Per-Plane Efficiencies vs. Track Momentum

Category-15 ESTR — D1 PER PLANE EFFICIENCIES — MC: DST8385

P AVG	PLANE-1	PLANE-2	PLANE-3	PLANE-4	PLANE-5	PLANE-6	PLANE-7	PLANE-8	AVERAGE	
				(NOTE: FIRST 2 LINES FROM CAT-3)						
2.2	96.0 ± 2	96.5 ± .2	94.7 ± .2	94.3 ± .2	94.7 ± .2	84.2 ± .3	91.5 ± .3	92.0 ± .3	92.8 ± .1	
6.6	93.3 ± .7	94.6 ± .6	94.0 ± .7	92.9 ± .7	92.9 ± .7	83.3 ± 1.0	91.9 ± .8	91.4 ± .8	91.7 ± .3	
3.8	91.7 ± .9	92.6 ± .9	92.9 ± .9	90.3 ± 1.0	93.8 ± .8	85.6 ± 1.1	90.4 ± 1.0	90.9 ± 1.0	91.0 ± .3	
7.2	91.1 ± .6	90.9 ± .7	90.8± .7	90.4 ± .7	92.8 ± .6	91.1 ± .6	86.6 ± .8	90.4 ± .7	90.5 ± .2	
12.1	90.4 ± 1.0	89.8 ± 1.1	90.2 ± 1.1	91.2 ± 1.0	90.4 ± 1.0	91.1 ± 1.0	86.0 ± 1.2	90.4± 1.0	89.9 ± .4	
17.2	88.3 ± 1.8	85.0 ± 2.0	90.7 ± 1.7	90.7 ± 1.7	90.1 ± 1.7	87.8 ± 1.9	86.4 ± 1.9	89.5 ± 1.8	88.5 ± .6	
22.1	87.6 ± 3.1	85.3 ± 3.3	87.6 ± 3.1	85.3 ± 3.3	83.2 ± 3.4	81.8 ± 3.5	81.8 ±3.5	83.9 ± 3.4	84.5 ± 1.2	
27.4	89.5 ± 4.1	82.3 ± 4.9	82.3 ± 4.9	87.9 ± 4.3	87.9 ± 4.3	79.7 ± 5.0	86.4 ± 4.5	96.2 ± 2.6	86.3 1.6	
32.5	78.8 ± 7.1	89.7 ± 5.7	86.7 ± 6.2	92.9 ± 4.9	100.0 ± .0	83.9 ± 6.6	76.5 ± 7.3	89.7 ± 5.7	86.7 ± 2.2	
37.9	77.8 ± 9.8	77.8 ± 9.8	87.5 ± 8.3	87.5 ± 8.3	77.8 ± 9.8	93.3 ± 6.4	87.5 ± 8.3	93.3 ± 6.4	84.8 ± 3.1	
42.1	.0 ± .0	91.7 ± 8.0	.0 ± .0	100.0 ± .0	91.7 ± 8.0	91.7 ± 8.0	.0 ± .0	91.7 ± 8.0	88.0 ± 3.2	
55.2	85.7 ± 7.6	81.8 ± 8.2	90.0 ± 6.7	94.7 ± 5.1	94.7 ± 5.1	94.7 ± 5.1	100.0 ± .0	94.7 ± 5.1	91.7 ± 2.2	
9.5	90.5 ± .5	90.2± .5	90.8 ± .4	90.4 ± .5	92.0 ± .4	89.2 ± .5	87.1 ± .5	90.4± .5	90.1± .2	Plane Averages

Category-15 ESTR — D2 PER PLANE EFFICIENCIES — MC: DST8385

P AVG	PLANE-1	PLANE-2	PLANE-3	PLANE-4	PLANE-5	PLANE-6	PLANE-7	PLANE-8	PLANE-9	PLANE-10	PLANE-11	PLANE-12	AVERAGE	
						(NOTE: FIRST 2 LINES FROM CAT-3)								
2.2	93.2 ± .2	93.4 ± .2	90.2 ± .3	89.9 ± .3	89.2 ± .3	87.8 ± .3	91.4 ± .2	92.4 ± .2	89.3 ± .3	91.5 ± .2	90.1 ± .3	89.1 ± .3	90.6 ± .1	
6.6	93.1 ± .6	92.0 ± .7	90.0 ± .8	89.9 ± .8	87.8 ± .8	87.3 ± .8	92.3 ± .7	91.4 ± .7	88.3 ± .8	91.7 ± .7	87.9 ± .8	93.0 ± .6	90.4 ± .2	
3.8	89.4 ± 1.0	89.8 ± .9	85.5 ± 1.1	87.9 ± 1.0	86.9 ± 1.0	85.2 ± 1.1	88.7 ± 1.0	89.4 ± .9	87.0 ± 1.0	88.3 ± 1.0	84.6 ± 1.1	88.4 ± 1.0	87.6 ± .3	
7.2	87.3 ± .7	87.0 ± .7	83.6 ± .8	85.7 ± .7	86.8 ± .7	85.4 ± .7	88.9 ± .7	89.4 ± .6	84.8 ± .7	88.7 ± .7	85.5 ± .7	89.0 ± .7	86.8 ± .2	
12.1	87.5 ± 1.1	85.8 ± 1.1	81.7 ± 1.3	84.0 ± 1.2	83.7 ± 1.2	86.1 ± 1.1	89.3 ± 1.0	87.4 ± 1.1	83.9 ± 1.2	87.0 ± 1.1	84.0 ± 1.2	86.6 ± 1.1	85.5 ± .3	
17.1	84.9 ± 1.9	82.1 ± 2.0	81.8 ± 2.0	85.6 ± 1.9	85.0 ± 1.9	83.7 ± 2.0	88.4 ± 1.7	84.9 ± 1.9	83.1 ± 2.0	86.0 ± 1.8	78.2 ± 2.1	88.0 ± 1.7	84.3 ± .6	
22.1	79.9 ± 3.2	82.1 ± 3.1	81.8 ± 3.1	84.9 ± 2.8	81.5 ± 3.1	79.2 ± 3.2	89.2 ± 2.6	88.1 ± 2.6	82.7 ± 3.0	86.1 ± 2.8	81.5 ± 3.1	85.4 ± 2.9	83.5 ± .9	
27.5	83.1 ± 4.4	87.0 ± 4.1	80.3 ± 4.6	80.5 ± 4.5	81.1 ± 4.6	78.7 ± 4.7	85.1 ± 4.1	84.5 4.3	83.8 ± 4.3	87.8 ± 3.8	86.7 ± 3.9	84.7 ± 4.2	83.6 ± 1.2	
32.4	71.9 ± 7.9	66.7± 8.2	74.2 ± 7.9	71.4 ± 7.6	73.3 ± 8.1	85.7 ± 6.6	71.9 ± 7.9	92.3 ± 5.2	73.3 ± 8.1	86.2 ± 6.4	80.6 ± 7.1	82.8 ± 7.0	77.0 ± 2.2	
36.8	86.4 ± 7.3	72.7 ± 9.5	90.5 ± 6.4	81.0 ± 8.6	85.7 ± 7.6	81.0 ± 8.6	90.5 ± 6.4	81.8 ± 8.2	86.4 ± 7.3	80.0 ± 8.9	90.5 ± 6.4	75.0 ± 8.8	83.3 ± 2.3	
42.1	.0 ± .0	.0 ± .0	.0 ± .0	.0 ± .0	100.0 ± .0	85.7 ± 9.4	.0 ± .0	100.0 ± .0	.0 ± .0	92.3 ± 7.4	.0 ± .0	100.0 — .0	81.9 ± 3.0	
54.1	83.3 ± 8.8	78.9 ± 9.4	68.2 ± 9.9	85.0 ± 8.0	80.0 ± 8.9	77.3 ± 8.9	100.0 ± .0	88.9 ± 7.4	.0 ± .0	83.3 ± 8.8	80.0 ± 8.9	88.9 ± 7.4	81.5 ± 2.6	
9.5	87.1 ± .5	86.6 ± .5	83.3 ± .5	85.6 ± .5	85.8 ± .5	85.0 ± .5	88.7 ± .5	88.6 ± .5	84.7 ± .5	88.0 ± .5	84.3 ± .5	88.1 ± .5	86.3 .1 ± .2	Plane Averages

Table A.1 Per-Plane Efficiencies vs. Track Momentum

Category-15 ESTR — D3 PER PLANE EFFICIENCIES — MC: DST8385

P AVG	PLANE-1	PLANE-2	PLANE-3	PLANE-4	PLANE-5	PLANE-6	PLANE-7	PLANE-8	PLANE-9	PLANE-10	PLANE-11	PLANE-12	AVERAGE	
3.8	87.1 ± 1.1	87.3 ± 1.1	88.7 ± 1.0	79.4 ± 1.3	86.2 ± 1.1	67.4 ± 1.4	86.7 ± 1.1	89.9 ± 1.0	89.8 ± 1.0	93.5 ± .8	81.5 ± 1.2	93.0 ± .8	85.6 ± .3	
7.2	87.3 ± .7	90.4 ± .6	87.2 ± .7	78.7 ± .8	85.6 ± .7	69.5 ± .9	87.7 ± .7	90.9 ± .6	89.7 ± .7	92.7 ± .6	79.9 ± .8	90.8 ± .6	85.6 ± .2	
12.1	88.5 ± 1.0	88.1 ± 1.1	89.7 ± 1.0	80.0 ± 1.3	85.6 ± 1.1	67.2 ± 1.4	87.5 ± 1.1	89.5 ± 1.0	88.4 ± 1.1	93.5 ± .8	85.9 ± 1.1	90.6 ± 1.0	85.9 ± .3	
17.2	86.2 ± 1.7	92.1 ± 1.4	87.5 ± 1.7	76.5 ± 2.1	85.8 ± 1.8	72.2 ± 2.1	86.2 ± 1.7	90.9 ± 1.5	86.4 ± 1.7	91.8 ± 1.4	92.0 ± 1.4	92.0 ± 1.4	86.4 ± .5	
22.2	81.5± 2.9	94.5 ± 1.8	90.0 ± 2.3	81.0 ± 2.9	88.2 ± 2.5	70.6 ± 3.3	86.9 ± 2.6	91.3 ± 2.2	89.5 ± 2.3	89.3 ± 2.4	92.3 ± 2.1	88.8 ± 2.4	86.7 ± .7	
27.4	78.2 ± 4.7	91.5 ± 3.3	80.8 ± 4.5	84.0 ± 4.2	84.4 ± 4.1	60.4 ± 5.1	89.3 + 3.6	89.2 ± 3.6	80.8 ± 4.5	97.1 ± 2.0	90.3 ± 3.5	89.0 ± 3.7	84.0 ± 1.2	
32.0	84.1 ± 5.5	90.5 ± 4.5	81.4 ± 5.9	81.8 ± 5.8	78.6 ± 6.3	72.3 ± 6.5	90.0 ± 4.7	95.1 ± 3.4	90.5 ± 4.5	83.7 ± 5.6	100.0 ± .0	92.3 ± 4.3	86.4 ± 1.5	
37.3	78.3 ± 8.6	85.7 ± 7.6	86.4 ± 7.3	72.0 ± 9.0	77.3 ± 8.9	81.8 ± 8.2	100.0 ± .0	77.3 ± 8.9	82.6 ± 7.9	94.7 ± 5.1	90.5 ± 6.4	94.7 ± 5.1	84.5 ± 2.3	
42.2	100.0 ± .0	87.5 ± 8.3	94.1 ± 5.7	88.2 ± 7.8	88.2 ± 7.8	.0 ± .0	83.3 ± 8.8	88.2 ± 7.8	94.1 ± 5.7	88.2 ± 7.8	88.2 ± 7.8	94.1 ± 5.7	88.3 ± 2.2	
54.7	84.6 ± 7.1	90.9 ± 6.1	87.5 ± 6.8	84.0 ± 7.3	95.7 ± 4.3	64.3 ± 9.1	95.5 ± 4.4	91.3 ± 5.9	91.3 ± 5.9	95.5 ± 4.4	100.0 ± .0	90.9 ± 6.1	88.7 ± 1.9	
9.8	87.0 ± .5	89.6 ± .4	88.0 ± .5	79.1 ± .6	85.8 ± .5	68.8 ± .6	87.4 ± .5	90.4 ± .4	89.0 ± .5	92.8 ± .4	83.2 ± .5	91.2 ± .4	85.7 ± .1	Plane Averages

Category-15 ESTR — MC: DST8385

D4 PER PLANE EFFICIENCIES

P AVG	PLANE-1	PLANE-2	PLANE-3	AVERAGE	
3.9	64.4 ± .7	71.4 ± .7	54.0 ± .6	62.4 ± 1.0	
7.3	75.4 ± .0	75.5 ± .0	62.7 ± .0	70.7 ± .6	
12.0	78.9 ± .4	77.4 ± .4	67.1 ± .5	74.1 ± .8	
17.2	76.9 ± .4	71.9 ± .5	61.5 ± .5	69.5 ± 1.4	
22.1	85.5 ± .9	83.9 ± .0	66.0 ± .4	77.4 ± 1.9	
27.4	79.7 ± .8	76.4 ± .0	64.7 ± .2	73.0 ± 3.0	
32.3	85.7 ± .9	81.1 ± .4	65.2 ± .0	76.3 ± 3.9	
37.0	73.9 ± .2	77.3 ± .9	73.9 ± .2	75.0 ± 5.3	
42.2	.0 ± .0	.0 ± .0	.0 ± .0	69.8 ± 7.0	
53.9	.0 ± .0	91.7± 8.0	.0 ± .0	62.3 ± 6.7	
9.9	74.5 ± .7	75.3 ± .7	62.0 ± .7	70.1 ± .4	Plane Averages

Table A.1 Per-Plane Efficiencies vs. Track Momentum

Category-15 SESTR — SMD PER PLANE EFFICIENCIES — Data: DST9010

P AVG.	PLANE-1	PLANE-2	PLANE-3	PLANE-4	PLANE-5	PLANE-6	PLANE-7	PLANE-8	PLANE-9	AVERAGE	
				(NOTE: FIRST 2 LINES FROM CAT-3)							
2.7	86.4 ± .4	93.6 ± .3	96.4 ± .2	85.8 ± .4	94.7 ± .3	87.7 ± .4	92.0 ± .3	96.7 ± .2	82.4 ± .5	90.4 ± .1	
4.2	83.2 ± 1.3	94.5 ± .8	96.0 ± .7	83.4 ± 1.3	96.2 ± .7	84.5 ± 1.2	93.2 ± .9	96.5 ± .7	87.5 ± 1.1	90.2 ± .3	
6.9	93.0 ± .6	94.6 ± .5	97.1 ± .4	91.3 ± .6	95.9 ± .5	93.5 ± .6	93.3 ± .6	96.0 ± .5	83.0 ± .8	92.9 ± .2	
7.6	91.0 ± .4	95.2 ± .3	97.7 ± .2	92.2 ± .4	96.4 ± .3	92.3 ± .4	94.8 ± .3	96.8 ± .3	90.4 ± .4	94.0 ± .1	
12.3	93.7 ± .4	95.8 ± .3	97.7 ± .2	93.8 ± .4	96.3 ± .3	93.9 ± .4	94.8 ± .3	97.4 ± .2	92.4 ± .4	95.1 ± .1	
17.3	94.8 ± .4	96.0 ± .4	98.0 ± .3	94.0 ± .4	96.5 ± .3	94.3 ± .4	95.8 ± .4	98.2 ± .3	92.6 ± .5	95.5 ± .1	
22.4	94.7 ± .5	96.1 ± .4	97.9 ± .3	94.0 ± .5	96.5 ± .4	94.8 ± .5	95.4 ± .5	97.7 ± .3	93.4 ± .6	95.6 ± .2	
27.3	93.6 ± .7	95.6 ± .6	97.8 ± .4	93.9 ± .7	96.0 ± .6	94.2 ± .7	96.1 ± .6	97.5 ± .4	92.7 ± .7	95.2 ± .2	
32.3	95.2 ± .7	96.0 ± .6	98.8 ± .4	94.0 ± .8	96.3 ± .6	93.4 ± .8	97.0 ± .6	98.0 ± .5	92.7 ± .8	95.7 ± .2	
37.4	93.1 ± 1.0	96.3 ± .7	96.9 ± .7	93.7 ± .9	96.9 ± .7	96.1 ± .8	95.4 ± .8	97.3 ± .6	91.1 ± 1.1	95.1 ± .3	
42.3	94.2 ± 1.0	95.7 ± .9	97.7 ± .7	95.1 ± 1.0	95.1 ± 1.0	92.5 ± 1.2	96.1 ± .9	98.1 ± .6	92.5 ± 1.2	95.2 ± .3	
66.7	95.7 ± .5	95.6 ± .5	97.5 ± .4	93.8 .6	96.1 ± .5	93.7 ± .6	96.8 ± .4	98.1 ± .3	91.7 ± .6	95.4 ± .2	
20.7	93.0 ± .2	95.7 ± .1	97.7 ± .1	93.0 .2	96.3 ± .1	93.2 ± .2	95.4 ± .1	97.5 ± .1	91.7 ± .2	94.8 ± .1	Plane Averages

Category-15 SESTR — DC1 PER PLANE EFFICIENCIES — Data: DST9010

P AVG.	PLANE-1	PLANE-2	PLANE-3	PLANE-4	PLANE-5	PLANE-6	PLANE-7	PLANE-8	AVERAGE	
				(NOTE: FIRST 2 LINES FROM CAT-3)						
2.6	97.3 ± .2	97.8 ± .2	96.0 ± .2	95.1 ± .2	93.5 ± .3	97.1 ± .2	94.0 ± .3	93.5 ± .3	95.5 ± .1	
6.8	97.3 ± .3	97.5 ± .3	96.0 ± .4	95.2 ± .4	95.5 ± .4	97.6 ± .3	94.5 ± .5	96.0 ± .4	96.2 ± .1	
4.2	97.0 ± .5	97.5 ± .5	96.2 ± .6	94.6 ± .7	93.4 ± .8	95.7 ± .6	93.3 ± .8	93.1 ± .8	95.1 ± .2	
7.6	97.3 ± .2	97.5 ± .2	95.5 ± .3	94.7 ± .3	94.1 ± .3	97.2 ± .2	92.5 ± .3	94.6 ± .3	95.4 ± .1	
12.3	97.5 ± .2	97.6 ± .2	95.7 ± .3	95.6 ± .3	94.3 ± .3	97.0 ± .3	92.7 ± .4	94.2 ± .3	95.5 ± .1	
17.3	97.5 ± .3	97.6 ± .3	96.5 ± .3	95.7 ± .4	93.9 ± .4	97.6 ± .3	91.5 ± .5	94.6 ± .4	95.6 ± .1	
22.4	97.5 ± .4	98.0 ± .3	96.2 ± .4	96.4 ± .4	92.9 ± .6	96.7 ± .4	91.6 ± .6	94.0 ± .5	95.4 ± .2	
27.3	98.0 ± .4	96.6 ± .5	96.8 ± .5	96.4 ± .5	91.7 ± .8	97.0 ± .5	89.6 ± .8	92.6 ± .7	94.8 ± .2	
32.3	97.1 ± .6	96.1 ± .7	96.8 ± .6	96.0 ± .7	91.3 ± .9	95.8 ± .7	89.8 ± 1.0	90.1 ± 1.0	94.0 ± .3	
37.4	98.3 ± .5	98.3 ± .5	96.6 ± .7	96.2 ± .7	89.7 ± 1.1	97.1 ± .7	91.4 ± 1.1	91.6 ± 1.1	94.8 ± .3	
42.3	97.3 ± .8	96.1 ± .9	96.9 ± .8	97.6 ± .7	87.3 ± 1.5	95.6 ± 1.0	87.3 ± 1.5	91.4 ± 1.3	93.5 ± .4	
65.4	95.7 ± .5	96.3 ± .5	96.0 ± .5	95.3 ± .5	83.8 ± .9	96.2 ± .5	88.7 ± .8	85.7 ± .9	92.0 ± .2	
19.4	97.3 ± .1	97.4 ± .1	96.0 ± .1	95.5 ± .1	92.6 ± .2	96.9 ± .1	91.6 ± .2	93.2 ± .2	95.0 ± .1	Plane Averages

Table A.1 Per-Plane Efficiencies vs. Track Momentum

Category-15 SESTR — D2 PER PLANE EFFICIENCIES — Data: DST9010

P AVG	PLANE-1	PLANE-2	PLANE-3	PLANE-4	PLANE-5	PLANE-6	PLANE-7	PLANE-8	PLANE-9	PLANE-10	PLANE-11	PLANE-12	AVERAGE	
					(NOTE: FIRST 2 LINES FROM CAT-3)									
2.6	90.2 ± .3	92.7 ± .3	84.6 ± .4	79.2 ± .4	87.8 ± .4	76.4 ± .5	88.7 ± .4	92.9 ± .3	87.0 ± .4	86.6 ± .4	91.3 ± .3	90.6 ± .3	87.2 ± .1	
6.9	91.8 ± 6	92.0 ± .6	86.2 ± .8	77.7 ± .9	85.5 ± .8	76.6 ± .9	89.1 ± .7	91.3 ± .6	86.5 ± .7	88.4 ± .7	89.7 ± .7	92.3 ± .6	87.1 ± .2	
4.2	90.6 ± .9	90.5 ± .9	87.7 ± 1.0	81.3 ± 1.2	86.4 ± 1.1	81.0 ± 1.2	90.5 ± .9	89.9 ± 1.0	81.0 ± 1.2	88.0 ± 1.0	87.0 ± 1.1	91.9 ± .9	87.1 ± .3	
7.6	92.5 ± .4	90.1 ± .4	87.6 ± .4	83.1 ± .5	88.5 ± .4	81.5 ± .5	90.2 ± .4	90.3 ± .4	84.3 ± .5	88.2 ± .4	87.7 ± .4	93.6 ± .3	88.1 ± .1	
12.3	92.1 ± .4	90.4 ± .4	87.5 ± .5	84.3 ± .5	88.6 ± .5	83.5 ± .5	91.2 ± .4	90.8 ± .4	83.1 ± .5	89.9 ± .5	87.5 ± .5	93.7 ± .4	88.5 ± .1	
17.3	91.3 ± .5	90.4 ± .6	87.2 ± .6	82.3 ± .7	88.8 ± .6	83.2 ± .7	90.1 ± .6	90.7 ± .6	82.5 ± .7	89.8 ± .6	88.7 ± .6	94.2 ± .4	88.2 ± .2	
22.4	92.8 ± .6	89.0 ± .7	88.1 ± .7	85.6 ± .8	89.5 ± .7	85.0 ± .8	91.6 ± .6	90.7 ± .7	82.2 ± .9	92.4 ± .6	90.7 ± .7	94.3 ± .5	89.2 ± .2	
27.3	91.4 ± .8	89.0 ± .9	85.6 ± 1.0	85.8 ± 1.0	89.3 ± .9	84.0 ± 1.0	91.4 ± .8	90.6 ± .8	81.9 ± 1.1	90.3 ± .8	90.0 ± .8	92.8 ± .7	88.4 ± .3	
32.3	92.8 ± .8	89.8 ± 1.0	84.7 ± 1.1	85.0 ± 1.1	87.1 ± 1.1	84.3 ± 1.2	93.1 ± .8	90.8 ± .9	81.3 ± 1.2	93.8 ± .8	91.8 ± .9	94.4 ± .8	89.0 ± .3	
37.4	90.1 ± 1.2	87.2 ± 1.3	85.4 ± 1.4	84.2 ± 1.4	89.3 ± 1.2	84.8 ± 1.4	92.7 ± 1.0	91.1 ± 1.1	82.8 ± 1.4	92.3 ± 1.0	90.7 ± 1.1	92.8 ± 1.0	88.6 ± .4	
42.3	92.4 ± 1.2	90.9 ± 1.3	86.9 ± 1.5	87.7 ± 1.4	89.1 ± 1.4	85.2 ± 1.5	91.2 ± 1.3	90.0 ± 1.3	80.7 ± 1.7	94.4 ± 1.0	90.2 ± 1.3	93.3 ± 1.1	89.3 ± .4	
67.0	90.8 ± .7	90.0 ± .7	87.3 ± .8	87.9 ± .7	88.3 ± .7	85.6 ± .8	91.8 ± .6	89.2 ± .7	84.4 ± .8	93.2 ± .6	92.5 ± .6	93.2 ± .6	89.5 ± .2	
20.5	91.9 ± .2	89.9 ± .2	87.2 ± .2	84.2 ± .2	88.6 ± .2	83.3 ± .3	91.0 ± .2	90.4 ± .2	83.1 ± .3	90.3 ± .2	88.9 ± .2	93.6 ± .2	88.5 ± .1	Plane Averages

Category-15 SESTR — D3 PER PLANE EFFICIENCIES — Data: DST9010

P AVG	PLANE-1	PLANE-2	PLANE-3	PLANE-4	PLANE-5	PLANE-6	PLANE-7	PLANE-8	PLANE-9	PLANE-10	PLANE-11	PLANE-12	AVERAGE	
4.2	86.9 ± 1.1	92.0 ± .9	85.4 ± 1.1	66.1 ± 1.4	87.0 ± 1.1	64.2 ± 1.4	87.0 ± 1.1	92.7 ± .9	88.4 ± 1.0	94.9 ± .7	91.1 ± .9	90.5 ± 1.0	84.8 ± .3	
7.6	86.8 ± .5	92.3 ± .4	85.0 ± .5	70.7 ± .6	86.4 ± .5	63.5 ± .6	87.5 ± .5	92.1 ± .4	90.8 ± .4	94.3 ± .3	92.3 ± .4	92.3 ± .4	85.6 ± .1	
12.3	86.8 ± .5	93.2 ± .4	85.1 ± .6	71.5 ± .7	85.4 ± .5	64.9 ± .7	87.7 ± .5	91.9 ± .4	90.0 ± .5	94.3 ± .4	93.8 ± .4	93.0 ± .4	85.9 ± .2	
17.4	87.8 ± .6	92.4 ± .5	85.5 ± .7	72.9 ± .8	86.4 ± .7	67.7 ± .8	89.6 ± .6	91.4 ± .5	91.6 ± .5	92.5 ± .5	94.4 ± .5	92.4 ± .5	86.6 ± .2	
22.3	86.6 ± .8	92.5 ± .6	84.9 ± .8	72.8 ± 1.0	87.3 ± .8	69.0 ± 1.0	89.3 ± .7	91.1 ± .7	91.1 ± .7	93.4 ± .6	94.0 ± .6	91.6 ± .7	86.5 ± .2	
27.3	86.1 ± 1.0	92.9 ± .7	87.2 ± .9	74.4 ± 1.2	88.1 ± .9	72.6 ± 1.2	90.5 ± .8	92.7 ± .7	92.5 ± .8	93.1 ± .7	94.7 ± .6	91.9 ± .8	87.7 .3	
32.2	87.4 ± 1.1	91.4 ± .9	88.2 ± 1.0	75.8 ± 1.3	88.1 ± 1.0	74.7 ± 1.4	90.5 ± 1.0	93.0 ± .8	92.3 ± 9	93.2 ± .8	94.1 ± .8	90.4 ± 1.0	88.0 ± .3	
37.4	84.9 ± 1.4	93.3 ± 1.0	87.6 ± 1.3	75.5 ± 1.6	87.4 ± 1.3	74.8 ± 1.6	89.5 ± 1.2	92.9 ± 1.0	94.3 ± .9	93.7 ± 1.0	94.3 ± .9	88.7 ± 1.2	87.8 ± .4	
42.3	89.1 ± 1.4	91.3 ± 1.3	85.1 ± 1.6	72.0 ± 1.9	88.3 ± 1.5	74.7 ± 1.9	86.8 ± 1.5	90.6 ± 1.3	91.9 ± 1.3	94.0 ± 1.1	94.8 ± 1.0	88.5 ± 1.5	86.9 ± .4	
67.1	84.3 ± .8	94.1 ± .6	89.0 ± .7	77.5 ± .9	88.5 ± .7	78.5 ± .9	90.7 ± .7	93.9 ± .6	92.5 ± .6	93.8 ± .6	94.7 ± .5	88.9 ± .7	88.7 ± .2	
20.8	86.6 ± .2	92.7 ± .2	85.9 ± .2	72.4 ± .3	86.8 ± .2	67.9 ± .3	88.6 ± .2	92.2 ± .2	91.1 ± .2	93.8 ± .2	93.6 ± .2	91.6 ± .2	86.5 ± .1	Plane Averages

Table A.1 Per-Plane Efficiencies vs. Track Momentum

Category-15 SESTR Data: DST9010

D4 PER PLANE EFFICIENCIES

P AVG	PLANE-1	PLANE-2	PLANE-3	AVERAGE	
4.2	62.3 ± 1.7	73.7 ± 1.6	58.3 ± 1.6	64.1 ± 1.0	
7.6	71.8 ± .6	76.1 ± .6	66.9 ± .7	71.4 ± .4	
12.3	79.0 ± .7	76.6 ± .7	70.2 ± .7	75.1 ± .4	
17.3	79.7 ± .8	74.3 ± .9	67.0 ± .9	73.3 ± .5	
22.3	79.8 ± 1.1	72.8 ± 1.1	62.2 ± 1.1	70.8 ± .7	
27.3	79.0 ± 1.3	73.1 ± 1.4	61.2 ± 1.4	70.3 ± .8	
32.3	80.6 ± 1.5	74.8 ± 1.6	59.1 ± 1.6	70.2 ± .9	
37.4	77.5 ± 2.0	69.3 ± 2.0	54.8 ± 2.0	65.8 ± 1.2	
42.3	79.3 ± 2.2	70.6 ± 2.3	54.6 ± 2.2	66.6 ± 1.3	
66.2	80.2 ± 1.2	71.5 ± 1.2	51.5 ± 1.2	65.4 ± .7	
19.8	76.4 ± .3	74.6 ± .3	64.0 ± .3	71.2 ± .2	Plane Averages

Table A.1 Per-Plane Efficiencies vs. Track Momentum

Category-15 ESTR — DC1 PER PLANE EFFICIENCIES — Data: DST9010

P AVG.	PLANE-1	PLANE-2	PLANE-3	PLANE-4	PLANE-5	PLANE-6	PLANE-7	PLANE-8	AVERAGE	
				(NOTE: FIRST 2 LINES FROM CAT-3)						
2.1	97.4 ± .2	98.0 ± .1	95.6 ± .2	93.7 ± .2	93.6 ± .3	84.3 ± .4	93.9 ± .2	92.9 ± .3	93.5 ± .1	
6.7	96.7 ± .5	98.0 ± .4	96.1 ± .6	93.9 ± .7	94.6 ± .7	83.4 ± 1.0	94.1 ± .7	94.2 ± .7	93.7 ± .2	
3.9	96.1 ± .8	97.9 ± .6	94.1 ± 1.0	92.1 ± 1.1	92.0 ± 1.1	86.5 ± 1.3	93.0 ± 1.0	90.8 ± 1.2	92.7 ± .4	
7.3	97.4 ± .4	97.5 ± .4	95.5 ± .5	94.4 ± .6	93.7 ± .6	95.1 ± .6	93.9 ± .6	94.4 ± .6	95.2 ± .2	
12.2	96.8 ± .6	98.7 ± .4	94.8 ± .8	95.9 ± .7	93.0 ± .9	97.4 ± .6	91.9 ± 1.0	94.6 ± .8	95.3 ± .3	
17.3	98.2 ± .7	97.9 ± .7	96.7 ± .9	96.9 ± .9	93.3 ± 1.2	96.9 ± .9	94.0 ± 1.2	91.7 ± 1.4	95.6 ± .4	
22.3	99.1 ± .6	98.7 ± .8	94.8 ± 1.4	96.9 ± 1.1	93.6 ± 1.6	96.5 ± 1.2	92.9 ± 1.7	91.7 ± 1.8	95.5 ± .5	
27.3	97.9 ± 1.2	97.2 ± 1.4	95.2 ± 1.8	96.5 ± 1.5	91.4 ± 2.3	97.2 ± 1.4	90.2 ± 2.4	93.2 ± 2.1	94.8 ± .7	
32.3	96.3 ± 2.1	98.7 ± 1.3	92.9 ± 2.8	95.1 ± 2.4	91.8 ± 3.0	97.5 ± 1.7	91.8 ± 3.0	92.9 ± 2.8	94.5 ± .9	
37.	100.0 ± .0	98.5 ± 1.5	98.5 ± 1.5	100.0 ± .0	89.0 ± 3.7	97.0 ± 2.1	100.0 ± .0	95.6 ± 2.5	97.2 ± .7	
42.3	93.8 ± 4.3	90.9 ± 5.0	90.9 ± 5.0	93.8 ± 4.3	90.9 ± 5.0	100.0 ± .0	93.8 ± 4.3	88.2 ± 5.5	92.7 ± 1.6	
63.1	96.7 ± 1.9	96.7 ± 1.9	97.8 ± 1.5	96.7 ± 1.9	78.1 ± 3.9	96.7 ± 1.9	89.9 ± 3.0	84.0 ± 3.6	91.5 ± 1.0	
13.1	97.3 ± .3	97.9 ± .2	95.2 ± .3	95.0 ± .3	92.6 ± .4	94.6 ± .4	93.1 ± .4	93.1 ± .4	94.8 ± .1	Plane Averages

Category-15 ESTR — D2 PER PLANE EFFICIENCIES — Data: DST9010

P AVG	PLANE-1	PLANE-2	PLANE-3	PLANE-4	PLANE-5	PLANE-6	PLANE-7	PLANE-8	PLANE-9	PLANE-10	PLANE-11	PLANE-12	AVERAGE	
						(NOTE: FIRST 2 LINES FROM CAT-3)								
2.1	90.5 ± .3	93.6 ± .3	88.1 ± .3	76.1 ± .4	85.4 ± .4	72.0 ± .4	85.3 ± .4	91.8 ± .3	86.5 ± .4	87.3 ± .3	91.2 ± .3	83.5 ± .4	85.7 ± .1	
6.7	92.4 ± .8	2.7 ± .8	88.3 ± .9	77.8 ± 1.2	83.3 ± 1.1	74.5 ± 1.2	86.7 ± 1.0	90.7 ± .9	85.1 ± 1.0	89.5 ± .9	89.2 ± .9	87.9 ± .9	86.3 ± .3	
3.8	90.7 ± 1.1	89.7 ± 1.2	88.7 ± 1.2	83.0 ± 1.4	85.4 ± 1.3	80.7 ± 1.5	90.1 ± 1.2	88.5 ± 1.2	85.1 ± 1.4	87.9 ± 1.3	89.4 ± 1.2	95.3 ± .8	87.8 ± .4	
7.3	90.5 ± .8	90.1 ± .8	84.5 ± .9	82.5 ± 1.0	85.7 ± .9	83.3 ± 1.0	88.8 ± .8	90.2 ± .8	83.5 ± 1.0	89.5 ± .8	88.4 ± .9	92.6 ± .7	87.4 ± .3	
12.2	90.2 ± 1.1	89.2 ± 1.2	85.1 ± 1.3	81.3 ± 1.4	86.4 ± 1.3	77.4 ± 1.5	91.7 ± 1.0	88.5 ± 1.2	82.7 ± 1.4	90.0 ± 1.1	88.9 ± 1.2	92.5 ± 1.0	86.8 ± .4	
17.2	87.7 ± 1.7	87.9 ± 1.7	83.8 ± 1.9	81.0 ± 2.0	86.2 ± 1.8	80.3 ± 2.0	91.9 ± 1.5	89.7 ± 1.6	78.5 ± 2.1	92.4 ± 1.4	87.1 ± 1.8	92.1 ± 1.5	86.4 ± .5	
22.3	89.6 ± 2.1	87.6 ± 2.2	86.1 ± 2.4	86.2 ± 2.3	85.8 ± 2.3	85.3 ± 2.4	92.6 ± 1.8	85.4 ± 2.3	86.7 ± 2.3	89.8 ± 2.1	90.8 ± 2.0	91.1 ± 1.9	88.0 ± .6	
27.3	88.5 ± 2.8	84.8 ± 3.1	77.6 ± 3.5	79.0 ± 3.5	85.1 ± 3.1	79.3 ± 3.4	84.7 ± 3.1	90.0 ± 2.6	84.7 ± 3.1	90.6 ± 2.6	85.7 ± 3.0	88.6 ± 2.8	84.8 ± .9	
32.4	86.3 ± 4.0	90.4 ± 3.4	85.3 ± 4.1	81.3 ± 4.5	83.1 ± 4.3	72.8 ± 4.9	86.7 ± 3.9	87.7 ± 3.8	77.1 ± 4.6	93.0 ± 3.0	92.9 ± 3.1	90.3 ± 3.5	85.3 ± 1.2	
37.5	87.7 ± 4.3	89.1 ± 4.2	84.2 ± 4.8	82.5 ± 5.0	89.3 ± 4.1	83.9 ± 4.9	92.7 ± 3.5	92.6 ± 3.6	76.3 ± 5.5	84.2 ± 4.8	91.1 ± 3.8	98.0 ± 1.9	87.5 ± 1.3	
42.1	97.1 ± 2.8	89.2 ± 5.1	91.9 ± 4.5	73.8 ± 6.8	81.6 ± 6.3	82.5 ± 6.0	89.2 ± 5.1	91.7 ± 4.6	84.6 ± 5.8	97.2 ± 2.7	83.3 ± 6.2	100.0 ± .0	88.2 ± 1.5	
66.9	92.7 ± 2.5	90.2 ± 2.8	87.0 ± 3.1	87.5 ± 3.1	86.7 ± 3.2	78.6 ± 3.7	89.5 ± 2.9	87.6 ± 3.1	80.3 ± 3.6	92.9 ± 2.4	95.5 ± 2.0	93.7 ± 2.3	88.3 ± .9	
13.1	90.1 ± .5	89.3 ± .5	85.3 ± .6	82.3 ± .6	85.8 ± .6	81.0 ± .6	90.0 ± .5	89.2 ± .5	83.0 ± .6	89.8 ± .5	88.9 ± .5	92.9 ± .4	87.2 ± .2	Plane Averages

Table A.1 Per-Plane Efficiencies vs. Track Momentum

Category-15 ESTR — D3 PER PLANE EFFICIENCIES — Data: DST9010

P AVG	PLANE-1	PLANE-2	PLANE-3	PLANE-4	PLANE-5	PLANE-6	PLANE-7	PLANE-8	PLANE-9	PLANE-10	PLANE-11	PLANE-12	AVERAGE	
3.8	87.9 ± 1.4	91.6 ± 1.2	85.4 ± 1.5	65.7 ± 1.8	85.2 ± 1.5	61.7 ± 1.8	84.2 ± 1.5	89.9 ± 1.3	86.0 ± 1.4	94.3 ± 1.0	88.4 ± 1.3	92.1 ± 1.1	83.6 ± .4	
7.3	86.4 ± 1.0	93.4 ± .7	84.0 ± 1.0	69.8 ± 1.2	85.8 ± 1.0	61.8 ± 1.2	87.8 ± .9	91.8 ± .8	87.3 ± .9	93.8 ± .7	90.8 ± .8	92.4 ± .8	84.7 ± .3	
12.2	87.8 ± 1.2	92.9 ± 1.0	86.4 ± 1.3	66.8 ± 1.7	84.6 ± 1.4	66.0 ± 1.7	87.2 ± 1.3	90.1 ± 1.1	88.2 ± 1.2	93.3 ± 1.0	95.4 ± .8	91.1 ± 1.1	85.2 ± .4	
17.2	85.7 ± 1.9	90.1 ± 1.6	86.6 ± 1.8	71.6 ± 2.3	83.2 ± 2.0	67.7 ± 2.4	87.5 ± 1.8	91.0 ±1.6	90.1 ± 1.6	92.0 ± 1.5	91.0 ± 1.6	91.8 ± 1.5	85.3 ± .6	
22.4	84.9 ± 2.5	88.2 ± 2.3	83.3 ± 2.6	69.7 ± 3.0	88.1 ± 2.3	70.5 ± 3.0	88.5 ± 2.3	89.5 ± 2.2	91.9 ± 1.9	92.0 ± 1.9	90.5 ± 2.1	94.7 ± 1.6	85.6 ± .7	
27.3	87.3 ± 2.9	91.9 ± 2.3	79.7 ± 3.4	72.7 ± 3.6	83.8 ± 3.1	69.9 ± 3.7	92.6 ± 2.3	94.7 ± 2.0	92.4 ± 2.3	91.2 ± 2.4	94.6 ± 2.0	91.2 ± 2.4	86.4 ± .8	
32.3	89.0 ± 3.5	89.9 ± 3.4	80.7 ± 4.2	73.6 ± 4.7	87.5 ± 3.7	73.9 ± 4.7	87.8 ± 3.6	92.3 ± 3.0	93.7 ± 2.7	96.1 ± 2.2	98.7 ± 1.3	88.1 ± 3.5	87.2 ± 1.1	
37.5	90.7 ± 3.9	88.5 ± 4.4	88.5 ± 4.4	71.4 ± 5.7	85.2 ± 4.8	70.5 ± 5.8	88.5 ± 4.4	94.1 ± 3.3	85.2 ± 4.8	90.2 ± 4.2	92.3 ± 3.7	85.2 ± 4.8	85.4 ± 1.4	
42.1	78.1 ± 7.3	96.6 ± 3.4	87.9 ± 5.7	74.3 ± 7.4	81.8 ± 6.7	75.7 ± 7.1	93.3 ± 4.6	90.3 ± 5.3	96.7 ± 3.3	75.7 ± 7.1	87.1 ± 6.0	90.0 ± 5.5	85.1 ± 1.8	
67.4	80.3 ± 3.7	93.6 ± 2.3	90.0 ± 2.9	74.8 ± 3.9	83.1 ± 3.5	74.8 ± 4.0	94.5 ± 2.2	89.4 ± 2.9	93.5 ± 2.4	93.4 ± 2.4	98.1 ± 1.3	89.6 ± 2.9	87.6 ± .9	
13.5	86.7 ± .6	92.2 ± .5	85.0 ± .6	69.1 ± .7	85.2 ± .6	64.8 ± .7	87.5 ± .6	91.0 ± .5	88.3 ± .5	93.2 ± .4	91.8 ± .5	91.8 ± .5	85.0 ± .2	Plane Averages

Category-15 ESTR — Data: DST9010

D4 PER PLANE EFFICIENCIES

P AVG	PLANE-1	PLANE-2	PLANE-3	AVERAGE	
3.9	63.3 ± .1	69.5 ± .1	56.7 ± .0	62.7 ± 1.2	
7.3	74.8 ± .2	75.2 ± .2	66.6 ± .3	72.0 ± .7	
12.2	77.2 ± .6	75.2 ± .7	70.4 ± .7	74.2 ± 1.0	
17.3	77.5 ± .5	73.4 ± .5	59.9 ± .6	69.4 ± 1.5	
22.4	88.2 ± .5	73.0 ± .1	64.8 ± .1	74.1 ± 1.8	
27.2	86.8 ± .5	60.8 ± .3	58.1 ± .2	66.4 ± 2.5	
32.5	84.4 ± .4	69.1 ± .2	42.2 ± .2	60.0 ± 3.6	
37.4	82.4 ± .5	65.1 ± .3	47.5 ± .5	61.8 ± 4.2	
42.3	80.8 ± .7	77.8 ± .0	55.3 ± .1	69.2 ± 4.8	
64.2	80.2 ± .4	73.0 ± .7	56.5 ± .6	68.4 ± 2.8	
13.1	75.1 ± .8	73.2 ± .8	63.4 ± .8	70.2 ± .5	Plane Averages

Table A.4 Percentages of Category 3-3, 15-15, and 3-15 K^0_S's

Category 3,7,15 Tracks — SMD PER PLANE EFFICIENCIES — Data: DST5705

ANGLE	PLANE-1	PLANE-5	PLANE-7	ANGLE	PLANE-2	PLANE-4	PLANE-8	ANGLE	PLANE-3	PLANE-6	PLANE-9	AVERAGE
.0049	96.1 ± .2	96.8 ± .2	97.2 ± .2	.0055	97.7 ± .2	95.3 ± .1	98.2 ± .2	.0048	98.5 ± .2	94.9 ± .1	95.3 ± .1	96.7 ± .1
.0147	94.4 ± .2	96.1 ± .2	97.0 ± .2	.0147	97.6 ± .2	94.7 ± .2	98.0 ± .2	.0148	98.6 ± .2	95.3 ± .2	94.4 ± .2	96.2 ± .1
.0247	94.5 ± .3	96.6 ± .3	96.1 ± .3	.0247	97.9 ± .3	94.6 ± .3	97.7 ± .3	.0248	98.4 ± .3	95.6 ± .3	94.1 ± .3	96.2 ± .1
.0347	93.9 ± .4	96.7 ± .4	95.6 ± .4	.0348	98.0 ± .4	93.2 ± .4	98.2 ± .4	.0347	98.4 ± .4	95.2 ± .4	94.4 ± .4	95.9 ± .1
.0448	92.9 ± .5	96.9 ± .5	95.8 ± .5	.0447	97.9 ± .6	93.2 ± .5	98.3 ± .6	.0447	98.4 ± .5	95.0 ± .5	92.8 ± .5	95.7 ± .2
.0548	93.0 ± .6	96.2 ± .6	95.4 ± .6	.0547	97.8 ± .7	92.3 ± .7	98.4 ± .7	.0547	97.8 ± .6	94.7 ± .6	91.7 ± .6	95.2 ± .2
.0648	94.8 ± .9	96.1 ± .9	93.5 ± .8	.0651	98.3 ± .8	93.7 ± .8	98.4 ± .8	.0648	98.6 ± .9	93.6 ± .9	91.3 ± .9	95.4 ± .2
.0747	92.6 ± 1.2	97.5 ± 1.2	94.0 ± 1.2	.0746	98.5 ± 1.1	92.6 ± 1.1	97.3 ± 1.1	.0749	98.1 ± 1.2	93.8 ± 1.1	92.7 ± 1.1	95.3 ± .3
.0849	93.0 ± 1.5	98.1 ± 1.5	95.2 ± 1.5	.0846	98.5 ± 1.6	93.2 ± 1.6	98.4 ± 1.6	.0847	97.7 ± 1.7	94.5 ± 1.7	87.1 ± 1.6	95.1 ± .3
.1021	91.4 ± 1.4	96.0 ± 1.4	96.5 ± 1.4	.1001	98.0 ± 1.4	94.7 ± 1.4	99.1 ± 1.4	.1009	98.7 ± 1.9	95.3 ± 1.9	63.6 ± 1.6	93.2 ± .3
.0288	94.4 ± .1	96.6 ± .1	96.2 ± .1	.0282	97.8 ± .1	94.3 ± .1	98.1 ± .1	.0279	98.4 ± .1	95.0 ± .1	93.4 ± .2	96.0 ± .0

Category 3,7,15 Tracks — SMD PER PLANE EFFICIENCIES — Monte Carlo: DST8379

.0050	95.3 ± .3	94.2 ± .3	95.7 ± .2.	0052	96.6 ± .2	94.6 ± .3	96.7 ± .2	.0049	96.7 ± .2	92.9 ± .3	96.2 ±.2	95.5 ± .1
.0150	94.9 ± .3	94.4 ± .3	96.2 ± .2	.0147	96.9 ± .2	94.6 ± .3	96.9 ± .2	.0149	96.6 ± .2	93.0 ± .3	95.9 ±.2	95.5 ± .1
.0248	94.5 ± .3	95.3 ± .3	95.3 ± .3	.0247	96.7 ± .2	93.1 ± .4	97.2 ± .2	.0248	97.3 ± .2	92.9 ± .3	95.5 ± .3	95.3 ± .1
.0348	94.4 ± .3	94.5 ± .3	95.2 ± .3	.0347	96.7 ± .3	93.0 ± .4	96.8 ± .3	.0348	96.9 ± .3	92.3 ± .4	95.1 ± .3	95.0 ±. 1
.0448	93.6 ± .4	94.7 ± .4	95.1 ± .4	.0448	96.8 ± .3	91.7 ± .5	96.4 ± .3	.0449	96.5 + .3	92.2 ± .5	94.8 ± .4	94.6 ± .1
.0548	93.4 ± .5	95.3 ± .4	95.3 ± .4	.0547	96.4 ± .4	91.7 ± .6	97.1 ± .4	.0548	94.6 ± .4	90.9 ± .6	95.3 ± .4	94.4 ± .2
.0647	93.9 ± .5	95.0 ± .5	94.8 ± .5	.0653	96.9 ± .4	92.2 ± .6	96.8 ± .4	.0647	92.8 ± .6	90.7 ± .7	94.8 ± .5	94.2 ± .2
.0747	93.8 ± .6	95.4 ± .5	95.0 ± .6	.0748	96.8 ± .4	93.6 ± .6	96.8 ± .4	.0746	90.5 ± .8	92.0 ± .8	94.8 ± .6	94.1 ± .2
.0845	94.4 ± .7	96.0 ± .6	96.0 ± .6	.0847	97.5 ± .4	92.8 ± .7	97.8 ± .4	.0845	89.1 ± 1.0	91.1 ± .9	89.7 ± 1.0	94.0 ± .2
.1029	94.2 ± .6	97.2 ± .4	96.7 ± .5	.1025	97.6 ± .3	94.6 ± .5	98.0 ± .3	.1004	90.6 ± 1.0	91.0 ± 1.0	66.9 ± 1.9	93.6 ± .2
.0342	94.5 ± .1	94.9 ± .1	95.5 ± .1	.0344	96.8 ± .1	93.6 ± .1	96.9 ± .1	.0324	95.8 ± .1	92.3 ± .1	94.6 ± .1	95.0 ± .0

Appendix B

B.1 The $\overline{K^\circ}K^\circ \rightarrow K^\circ_S K^\circ_S$ branching ratio

To determine the correct $\overline{K^\circ}K^\circ \rightarrow K^\circ_S K^\circ_S$ branching ratio to use for the decay $D^\circ \rightarrow \overline{K^\circ}K^\circ$, I used the conservation of angular momentum in weak decays. Since the D° is a pseudo-scalar ($J^P = 0^-$), the $\overline{K^\circ}K^\circ$ must have orbital angular momentum l=0. This s-state is even under spatial inversion, so the $\overline{K^\circ}K^\circ$ spatial wave function immediately following the D° decay must be:

$$|D^\circ\rangle \rightarrow |f\rangle = \frac{1}{\sqrt{2}}\left[\left|K^\circ(z);\overline{K^\circ}(-z)\right\rangle + \left|K^\circ(-z);\overline{K^\circ}(z)\right\rangle\right]. \qquad \text{(B.1)}$$

Using the weak eigenstate expansion for $\overline{K^\circ}$ and K°

$$|K^\circ\rangle = \frac{1}{\sqrt{2}}\frac{1}{p}\left[\left|K^\circ_S\right\rangle + \left|K^\circ_L\right\rangle\right]$$

$$|\overline{K^\circ}\rangle = \frac{1}{\sqrt{2}}\frac{1}{q}\left[\left|K^\circ_S\right\rangle - \left|K^\circ_L\right\rangle\right] \qquad \text{(B.2)}^\dagger$$

equation (B.1) can be rewritten as

$$|D^\circ\rangle \rightarrow |f\rangle = \frac{1}{\sqrt{2}}\frac{1}{pq}\left[\left|K^\circ_S(z);K^\circ_S(-z)\right\rangle - \left|K^\circ_L(-z);K^\circ_L(z)\right\rangle\right]. \qquad \text{(B.3)}$$

So the correct value is $BR(\overline{K^\circ}K^\circ \rightarrow K^\circ_S K^\circ_S) = 1/2$ for the decay $D^\circ \rightarrow \overline{K^\circ}K^\circ$.

---

† p=q=1 in the limit of CP conservation (ε=0)

B.2 The $\overline{K^\circ}\,\overline{K^\circ}K^\circ \rightarrow K_S^\circ\, K_S^\circ\, K_S^\circ$ branching ratio

A determination of the correct BR($\overline{K^\circ}\,\overline{K^\circ}K^\circ \rightarrow K_S^\circ\, K_S^\circ\, K_S^\circ$) for the decay $D^\circ \rightarrow \overline{K^\circ}\,\overline{K^\circ}K^\circ$ depends on the relative angular momenta of the K_S°'s. These need not be 0 since only the total angular momentum must be 0 (see argument in B.1). For simplicity†, I will calculate BR($\overline{K^\circ}\,\overline{K^\circ}K^\circ \rightarrow K_S^\circ\, K_S^\circ\, K_S^\circ$) for all K°'s and $\overline{K^\circ}$'s in an s-wave. As in B.1, the kaons must be in a state even under spacial inversion. This state must also be symmetric under interchange of the $\overline{K^\circ}$ bosons, giving

$$|D^\circ\rangle \rightarrow |f\rangle = \frac{1}{\sqrt{4}}\left[\begin{array}{l}|\overline{K^\circ}(1);\overline{K^\circ}(2);K^\circ(3)\rangle + |\overline{K^\circ}(2);\overline{K^\circ}(1);K^\circ(3)\rangle + \\ |\overline{K^\circ}(-1);\overline{K^\circ}(-2);K^\circ(-3)\rangle + |\overline{K^\circ}(-2);\overline{K^\circ}(-1);K^\circ(-3)\rangle\end{array}\right]. \quad \text{(B.4)}$$

where 1, 2, and 3 are the momenta for particles 1, 2, and 3. Substitution of (B.2) into (B.4) and collection of like terms yields

$$|D^\circ\rangle \rightarrow |f\rangle = \frac{1}{\sqrt{32}}\frac{1}{pq^2}\left[\begin{array}{l}4\left|K_S^\circ;K_S^\circ;K_S^\circ\right\rangle + 4\left|K_L^\circ;K_L^\circ;K_L^\circ\right\rangle + \\ 12\left|K_S^\circ;K_S^\circ;K_L^\circ\right\rangle + 12\left|K_L^\circ;K_L^\circ;K_S^\circ\right\rangle\end{array}\right]. \quad \text{(B.5)}$$

So BR($\overline{K^\circ}\,\overline{K^\circ}K^\circ \rightarrow K_S^\circ\, K_S^\circ\, K_S^\circ$) = 1/8 for the given assumptions.

† and since there is very little phase space left for angular momentum